Synthesis of oxide layer coated ZnO and TiO_2 nanoparticles and their application in dye sensitized solar cells

A THESIS

Submitted to the

FACULTY OF SCIENCE

THAPAR UNIVERSITY, PATIALA

for the degree of

Doctor of Philosophy

By

MANVEEN KAUR

Regn. No. 900912007

School of Physics & Materials Science

Thapar University

Patiala - 147 004

INDIA

October 2013

DECLARATION

It is certified that the thesis is entirely my own and that the ideas and references cited herein have been duly acknowledged.

(Manveen Kaur)

Attestation by supervisor

(Dr. N. K. Verma)

Senior Professor

School of Physics and Materials Science,

Thapar University,

Patiala – 147 004

INDIA

CERTIFICATE

This is to certify that the thesis entitled, "**Synthesis of oxide layer coated ZnO and TiO_2 nanoparticles and their application in dye sensitized solar cells**", submitted by **Ms. Manveen Kaur** in the fulfillment of the requirement for the award of the degree of Doctor of Philosophy in the School of Physics and Materials Science, Thapar University, Patiala, is a record of candidate's own work carried out by her under my supervision and guidance. The matter presented in this thesis has not been submitted in part or full for the award of any degree in any other University or Institute.

Attestation by supervisor

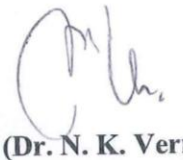

(Dr. N. K. Verma)

Senior Professor

School of Physics and Materials Science,

Thapar University,

Patiala – 147 004

INDIA

TO
MY BELOVED
PARENTS
AND
FRIENDS

ACKNOWLEDGEMENT

I humbly prostrate myself before the **Almighty** for HIS grace and abundant blessings which enabled me to complete my work successfully and to my full satisfaction.

I would like to express my sincere gratitude to my supervisor **Dr. N. K. Verma** for his continuous guidance and wholehearted support as well as for his patience, motivation, enthusiasm, and immense knowledge. A special word of thanks to **Mrs. (Dr.) Rama Verma** for her motherly affection and care.

I am profoundly obliged to **Dr. K. K. Raina**, Director, **Dr. Kulvir Singh**, Head, **Dr. O. P. Pandey**, Senior professor, School of Physics and Materials Science, for their full support and motivation. I am also thankful to the entire faculty of School of Physics and Materials for their support.

I would like to thank my Doctoral Committee: **Dr. B. N. Chudasama, Dr Bonamali Pal**, for their encouragement and constructive comments.

I acknowledge with thanks the support of the technical and secretarial staff of the Department.

I am grateful to Thapar University management for awarding me Teaching Associateship during my research work.

I am grateful to the **University Grants Commission (UGC)** for the funding vide sanction letter no. F.No. 39-533/2010 (SR) dated January 7, 2011.

I would like to express my gratitude to my seniors **Dr. Zinki Jindal, Dr. Sanjeev Kumar** and **Dr. Sunil Kumar** for their guidance, suggestions and inspiration.

I would like to thank **Dr. Poonam Sharma**, St. Francis Xavier University for constructive discussions and suggestions.

I would like to show my greatest appreciation to my co-researchers **Mr. Gurmeet Singh Lotey, Ms. Lavanya Khanna, Mr. Jaspal Singh, Ms. Gitanjali Dhir, Ms.**

Kamaldeep Kaur, Ms. Imanpreet Kaur and Mr. Sunil Kumar who have been a source of motivation, support and laughter throughout this journey.

I especially thank **Ms. Supreet** and **Ms. Gudveen Sawhney** for their co-operation and encouragement.

Special thanks goes to my friends, **Mr. Harshpreet Singh, Ms. Arvind Rishi Raj, Mrs. Kirandeep Kaur** and **Ms. Anuja Saxena**, for their unmatched support and motivation.

I am thankful to **Mr. Manpreet Singh Manna** (Associate Professor, SLIET, Longowal) for encouraging me to pursue research.

My mother **Mrs. Paramjit Kaur** and father **Mr. Surjit Singh Bedi** have supported and helped me along the course of this dissertation by giving encouragement and providing the moral and emotional support I needed to complete my thesis. Special thanks to my brother **Mr. Harshmeet Singh Bedi**, for always motivating me.

I would like to thank all my well-wishers, whose names may not be mentioned here but are deeply acknowledged.

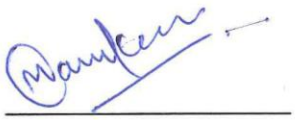

(Manveen Kaur)

CONTENTS

LIST OF FIGURES

LIST OF TABLES

LIST OF PUBLICATIONS

I. Papers in SCI/refereed journals

1. Manveen Kaur, N. K. Verma, 'Structural and optical properties of Eu_2O_3 coated TiO_2 nanoparticles and their application for dye sensitized solar cell', Journal of Materials Science: Materials in Electronics, (2013) 24:1121–1127
2. Manveen Kaur, N. K. Verma, 'Performance of Eu_2O_3 coated ZnO nanoparticles-based DSSC', Journal of Materials Science: Materials in Electronics, (2013) 24:3617–3623
3. Manveen Kaur, N. K. Verma, '$CaCO_3$/TiO_2 nanoparticles based dye sensitized solar cell', Journal of Materials Science and Technology, (2013) DOI - 10.1016/j.jmst.2013.10.016
4. Manveen Kaur, N. K. Verma, 'Study on $CaCO_3$-coated ZnO nanoparticles based dye sensitized solar cell', Journal of Materials Science: Materials in Electronics, DOI - 10.1007/s10854-013-1512-8
5. Manveen Kaur, N. K. Verma, 'Performance of dye-sensitized solar cell fabricated using titania nanoparticles calcined at different temperatures', Materials Science-Poland, (2013) 31(3): 378-385

II. Papers in non-SCI journals

1. Manveen Kaur, N. K. Verma, 'Application of Eu_2O_3/ZnO nanoparticles in dye sensitized solar cell', AIP Conference Proceeding, (2013) 1536: 69-70
2. Manveen Kaur, N. K. Verma, 'Eu_2O_3/ZnO nanocomposites for dye sensitized solar cell', Excel India Publishers, (2013) 2171-2176

III. Papers communicated

1. Manveen Kaur, N. K. Verma, 'Photocatalytic degradation of methyl orange by Eu_2O_3 coated TiO_2 nanoparticles', communicated to Materials Science-Poland (Springer) April, 2013
2. Manveen Kaur, Rajwant Singh, N. K. Verma, 'Tb_2O_3 coated TiO_2 nanoparticles based dye-sensitized solar cell', communicated to Journal of Materials Science & Technology (Elsevier) September, 2013

IV. Papers in conference proceedings

1. Manveen Kaur, N. K. Verma, 'Size and phase dependent performance of TiO_2 nanoparticles based dye sensitized solar cells', Emerging Trends in Physics for Environmental Monitoring & Management (ETPEMM-12), December 17-19, 2012, Punjabi University, Patiala, pp. 33 (Oral presentation)
2. Manveen Kaur, N. K. Verma, 'Synthesis and characterization of Eu_2O_3 coated ZnO nanoparticles', 23rd Annual General Meeting of Materials Research Society of India (MRSI), February 13-15, 2012, Thapar University, Patiala, pp. 88-89 (Poster presentation)
3. Manveen Kaur and N. K. Verma, 'Photocatalytic degradation of N719 dye by TiO_2 nanoparticles', 4^{th} Bangalore Nano Conference, December 8-9, 2011, pp. 107 (Poster presentation)
4. Manveen Kaur and N. K. Verma, 'Synthesis and characterization of Eu_2O_3 coated TiO_2 nanoparticles', The National Conference on Nanoscience Fundamentals & Applications, July 23-24, 2011, pp. 38 (Poster presentation)
5. Manveen Kaur and N. K. Verma, 'Synthesis and characterization of CdS nanoparticles', International conference on Advances in Materials &

Manufacturing Technology (AMMT-2011), July 20-21, 2011, pp. 194-195 (Oral presentation)

6. Manveen Kaur, N. K. Verma, 'Synthesis and characterization of $CaCO_3$ coated ZnO nanoparticles', National Seminar on Advanced Materials and Devices, July 3-4, 2011 (Poster Presentation)
7. Manveen Kaur, N. K. Verma, 'Synthesis of $CaCO_3$ coated ZnO nanoparticles and their application in dye sensitized solar cells', International Conference on Emerging Trends in Mechanical Engineering ICETME-2011, February 24-26, 2011, (Oral Presentation)
8. Manveen Kaur, N. K. Verma, '$CaCO_3$ coated ZnO nanostructures for dye sensitized solar cells', 14^{th} Punjab Science Congress, February 7-9, 2011, pp. 112 (Oral presentation)
9. Manveen Kaur, Zinki Jindal and N. K. Verma, 'Structural and optical studies of silver doped CdS nanoparticles', First National Conference on Recent Advances in Polymer Nanocomposites, January 14-15, 2011, (Oral Presentation)
10. Manveen Kaur, N. K. Verma, 'Synthesis and characterization of Cu/CdSe hetero nanostructures by electrochemical template synthesis', National Conference on Smart, Electronic & Engineering Materials SEEMs, March 5-6, 2010, pp-50 (Oral Presentation)

ABSTRACT

ZnO and TiO_2 nanoparticles are very promising materials for dye-sensitized solar cells (DSSCs) because of their unique properties such as bandgap, chemical stability, high electron mobility, nontoxicity. A DSSC comprises of a dye adsorbed semiconductor (TiO_2, ZnO) electrode, and a liquid electrolyte containing redox couple sandwiched between two transparent conductive oxide (TCO) glasses. However, the efficiency of DSSCs is limited due to the charge recombination of the semiconductor with the dye or the electrolyte used. The research work is, therefore, mainly aimed at, to reduce the charge recombination problem. The problem has been resolved using a synthesized oxide layer (Eu_2O_3, $CaCO_3$) coated semiconductor nanoparticles (ZnO, TiO_2) as photoelectrode. For the syntheses of ZnO and TiO_2 nanoparticles, respectively, the chemical precipitation and sol-gel techniques have been used whereas, for the oxide layer coating on the surface of nanoparticles (TiO_2 and ZnO), the hydrothermal method has been employed. Four different combinations (Eu_2O_3/ZnO, $CaCO_3$/ZnO, Eu_2O_3/TiO_2, and $CaCO_3$/TiO_2) have been taken. Their structural and compositional studies have been carried out using XRD and EDAX; morphological analysis using SEM/TEM; optical studies using FTIR and PL. To determine the amount of dye adsorbed on the fabricated electrodes, UV-visible analysis of the dye desorbed solution has been done. And the solar cell parameters such as short-circuit current density, open circuit voltage, fill factor, efficiency, have been calculated using the current density-voltage characteristics.

PREFACE

This thesis presents the synthesis of $CaCO_3$ and Eu_2O_3 coated ZnO and TiO_2 nanoparticles by chemical synthesis route as well as the investigations of structural, morphological and optical properties of the synthesized nanoparticles. These nanoparticles have been employed in DSSCs, and their photocurrent density-voltage (J-V) characteristics have been studied.

Chapter 1: Introduction

Highlights the importance and need of solar energy, and the different generations of solar cells. Working and mechanism of DSSCs have been discussed in this chapter. An interesting section of this chapter "recent advances in DSSCs" comprises the recombination problem in DSSCs and their various solutions by different research groups. Literature review of different coatings used by various researches is presented. Importance of coating of rare earth oxides and insulating oxides on the semiconductor (TiO_2, ZnO) nanoparticles is given. The objective of the present thesis is also discussed in brief.

Chapter 2: Materials and characterization

Provides information about the materials used (TiO_2, ZnO) in the present work. The experimental procedure for the synthesis of TiO_2 and ZnO nanoparticles has been described. The fabrication procedure for the DSSCs has been discussed in detail. The chapter also describes various characterization techniques used in the present study for the synthesized nanoparticles and the fabricated DSSCs. Introduction, principle, theory and instrumentation of characterization techniques have also been described.

Chapter 3: Oxide-layer coated ZnO nanoparticles and their application in dye sensitized solar cells

Comprises results and discussion for Eu_2O_3 and $CaCO_3$ coated ZnO nanoparticles. The synthesized nanoparticles have been characterized structurally through XRD, morphologically through SEM, TEM and compositionally through EDAX. The different bonds in the synthesized material have been studied through FTIR. Dye desorption studies are presented, which compare the dye adsorbed on the fabricated electrodes. The analyses of the obtained current density-voltage (J-V) characteristics of the fabricated DSSCs are also presented.

Chapter 4: Oxide-layer coated TiO_2 nanoparticles and their application in dye sensitized solar cells

Presents the results and discussion regarding Eu_2O_3 and $CaCO_3$ coated TiO_2 nanoparticles and the DSSCs made thereof. The synthesized nanoparticles have been characterized through XRD, TEM, EDAX, FTIR and PL spectroscopy. The dye desorbed studies are performed to compare the dye adsorbed on the fabricated electrodes. The J-V characteristics of the fabricated DSSCs and their analyses are presented.

Chapter 5: Conclusions and future scope

Concludes the research work done including the future scope of this work.

Chapter 1

Introduction

Chapter-1

Non-renewable reserves are dwindling because of high cost and environmentally damaging retrieval techniques. So, there is a significant need for cheap and sustainable resources. Renewable energy sources, specifically solar power, can be extremely practical as alternatives to damaging carbon-intensive fuels. The ability to design nanostructured semiconductors, organic-inorganic hybrid assemblies, and molecular assemblies opens up new ways to design third generation light energy conversion devices. Extensive research on dyes, semiconductor oxides, and redox electrolytes is being carried out for the development of more efficient dye sensitized solar cells.

1.1 Energy

Energy has been universally known as one of the most vital inputs for economic growth and human development. Energy is one of the major drivers of a growing economy like India and is an essential building block of economic development. In an effort to meet the demands of a developing nation, the Indian energy sector has witnessed a rapid growth [1]. In order to address the economic and environmental consequences of energy system, the availability and consumption of energy resources is considered. Problems arise from our dependence on combustible fuels, the environmental risks related with their extraction, and the environmental destruction caused by their emissions [2]. Yet no primary energy source, be it renewable or non-renewable, is free of environmental or economic limitations.

1.1.1 Non-renewable energy resources

The non-renewable energy resources can be defined as the energy resources that are not sustainable and depleting at a very fast rate with increasing consumption. Fossil fuel (such as oil, petroleum, natural gas and coal) and radioactive fuel (uranium) are the most common non-renewable energy sources. Non-renewable energy reserves have a very negative effect on the environment when mined, processed and consumed. The use of non-renewable energy resources leads to air, water and soil pollution, and produce greenhouse gases which result in climate crisis such as global warming and acid rain. Also the non-sustainable energy resources are limited, hence becoming more and more expensive with time.

1.1.2 Renewable energy resources

Renewable energy is generated from natural resources such as sunlight, wind, rain, tides and geothermal heat, which are naturally replenished. Figure 1.1 shows the various renewable and non-renewable sources of energy. Most of these renewable energy technologies have been around for years and there is an increase in their efficiency due to technological innovation.

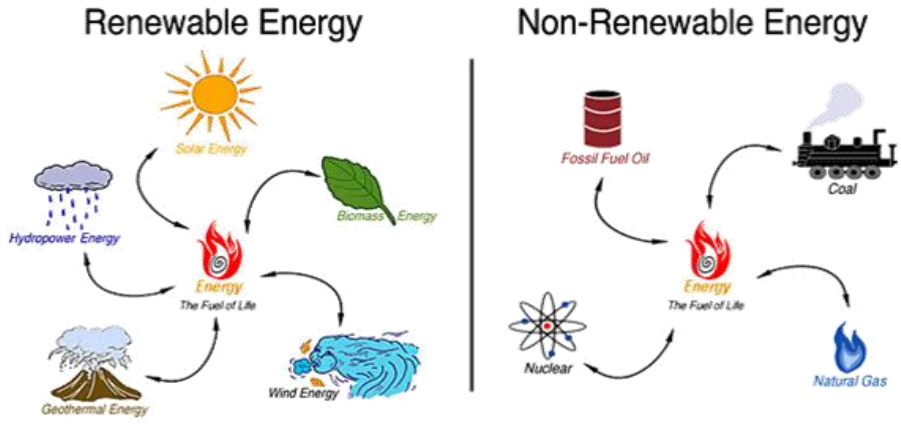

Figure 1.1 Renewable and non-renewable energy resources

Natural energy resources such as oil, coal and natural gas, required for all types of transportation, communication, industry, houses and many other human activities, are depleting at a very fast rate. The threat that the natural resources are being consumed at a very fast rate, is forcing us to identify new sources of energy that are environmentally friendly and able to replace current supplies. There is a current global need for clean and renewable energy sources. Polymer batteries, fuel cells, photovoltaic cells, wind power generators, and geothermal power generators are some possible alternatives. The need of the hour is to find safe, renewable sources of sustainable energy that do not pose any hazards in the long run. Efforts are also on to find effective means for creating green energy, meaning energy that is environmental friendly. Natural sources such as solar energy, wind energy, hydro energy can be tapped and channelled to generate power through solar cells, wind turbines, etc. for numerous applications. These energy sources are inexhaustible, unlike petroleum and its derived products, which are getting used up faster with each passing day. Renewable energy comes from a variety of sources. These include:

Wind power - Wind power harnesses the energy in the wind through wind turbines to make electrical power, windmills for mechanical power, and wind pumps for water pumping or drainage.

Hydroelectric energy - Hydroelectric energy refers to the power generated by the use of the gravitational force of falling or flowing water.

Ocean wave energy – Ocean wave energy harnesses the undulating action of waves to generate energy.

Biofuels - Biofuels include fuels derived from biomass, or biological materials.

Solar Power - Solar light energy can be directly converted into electricity by the photovoltaic effect using photovoltaic cells. Solar panels are dependent on sunlight,

however new technologies are being developed that increase the sensitivity of the panels so that they can generate energy even on cloudy days. In addition to solar panels, other ways of producing energy from sunlight such as solar shingles and solar roof tiles are becoming popular.

Renewable energy sources, specifically solar power, can be extremely practical as alternatives to damaging carbon-intensive fuels.

1.2 Sun as the ultimate source of energy

In order to meet the increasing energy demand, we are forced to seek environmentally clean alternate energy resources. Major options to tackle the 10 TW clean energy demand includes carbon neutral energy, nuclear power, and renewable energy. To produce such a huge amount of energy using fossil fuels without affecting the environment, secure storage for 25 billion metric tons of CO_2 produced annually is required. To generate 10 TW of energy using nuclear power, there is a need of constructing everyday one new GW electric nuclear fission plant for the next 50 years. Different types of renewable energy sources are expected to contribute future energy production, but each source can only extract a finite amount of power. Hydroelectric resources account for only 0.5 TW possible energy production, capturing energy from all tides and oceans 2 TW, implementing geothermal energy over all land area, 12 TW, all globally extractable wind power, 2-4 TW, and the solar energy striking the earth, 1,20,000 TW [3]. Among these options, solar energy stands out as the most viable choice to meet future energy demand. Solar panels can be used to provide electricity on a small scale to homes to supplement the electricity supply from the national grid or can be used to power whole towns. Despite this, the energy produced from solar energy remains less than 0.01% of the total energy demand [4]. Solar energy research symbolizes an innovative approach of addressing the challenges

associated with shifting global energy production away from fossil fuels to provide a secure, environmental friendly and virtually unlimited supply of energy for the future. Although solar radiation is ideal to meet the projected demand, it requires new initiatives to harvest incident photons with greater efficiency for example, by employing nanostructured semiconductors and molecular assemblies [3].

1.3 Photovoltaic cell

Photovoltaic cells convert light energy directly into electricity. They are often called solar cells because the source of light is usually the sun. A solar cell is a photonic device that converts light energy directly into electricity and function by the photovoltaic effect. Photo means light and voltaic means electrical current or electricity (light-electricity). Solar cells provide direct current (DC) electricity that can be used to power DC motors and light bulbs [5]. Solar cells can be used to charge rechargeable batteries so that electricity can be stored for later use when the sun is not available.

1.3.1 History of solar cells

Solar power technology is not a recent one; in fact, it dates back to the mid-century. Use of solar power cannot be credited to one inventor but to numerous great minds. In 1839, French physicist Alexandre Edmond Becquerel discovered the photovoltaic effect [6]. He claimed that "shining light on an electrode submerged in a conductive solution would create an electric current". In 1865 Auguste Mouchout was the first man to patent a design for an engine running on solar energy [7]. He designed a device, which could turn solar energy into mechanical steam power, and operate a steam engine. In 1883 Charles Fritz invented the first true photovoltaic cell [8]. The solar cell had a conversion rate of only 1-2% but represented the beginning of solar

technology. With Albert Einstein publishing a paper on photoelectric effect in 1905, a scientist named Robert Millikan in 1916 evidenced the photoelectric effect experimentally [9]. Over the following 65 years, many scientists tried to improve solar power technology and did so with great success. The first commercial solar panel went on the market in 1956. It was very expensive, costing around $300 per watt [10]. In 1970, there was a huge energy crisis, and people became aware that it was becoming more and more necessary to look for alternate energy sources. As solar panel technology improved, prices got down to $20 per watt. Research in this area continued to produce and develop many types and structures of the materials presently used in photovoltaic (PV) technology.

1.3.2 Generations of solar cells

Solar cells are usually divided into three main categories called generations:

1.3.2.1 First generation solar cells

The first generation photovoltaic cell consists of a large-area, single-crystal, single layer p-n junction diode, capable of generating electrical energy from light. These cells are typically made using diffusion process with silicon wafers. First-generation photovoltaic cells are the dominant technology in the commercial production of solar cells, accounting for more than 86% of the terrestrial solar cell market. The efficiency achieved by first generation solar cells is 24% [11]. However, the expensive material cost and the long energy payback time prevented their large spread. The single crystal silicon based photovoltaic devices that are commercially available deliver power with 15% efficiency. The first generation solar cells suffer from high cost of manufacturing and installation.

1.3.2.2 Second generation solar cells

The second generation, also called thin-film solar cells, have been under intense development for the 1990s, are low-cost, low-efficiency cells. They are significantly cheaper to produce than the first generation cells but have lower efficiency. The second generation of photovoltaic materials is based on the use of thin epitaxial deposits of semiconductors on lattice-matched wafers. The most popular materials used for the second generation solar cells are copper indium gallium diselenide (CIGS), cadmium telluride (CdTe), micromorphous silicon and amorphous silicon [12]. The second generation devices made up CIGS polycrystalline semiconductor thin films brought down the price significantly, but their efficiency needed to be enhanced in order to make them practically viable. There are two classes of epitaxial photovoltaics - space and terrestrial. Space cells typically have higher AM0 efficiencies (28-30%) in production, but have a higher cost per watt. The efficiency achieved by second generation solar cells is around 17%. Second generation solar cells comprise a small segment of the terrestrial photovoltaic market, and approximately 90% of the space market [13].

1.3.2.3 Third generation solar cells

Third generation solar cells are the leading edge of solar technology. Still in the research phase, third generation cells have moved well beyond silicon-based cells. Third-generation photovoltaics are proposed to be very different from the previous semiconductor devices as they do not rely on a traditional p-n junction to separate photo-generated charge carriers [14]. For space applications quantum well devices (quantum dots, quantum ropes, etc.) and devices incorporating carbon nanotubes are being studied - with a potential for up to 45% AM0 production efficiency. For

terrestrial applications, these new devices include photo-electrochemical cells, polymer solar cells, nanocrystal solar cells, dye-sensitized solar cells. Table 1.1 compares the efficiency of the three generations of the solar cells.

Table 1.1 Comparison of different generations of solar cell [15]

Classification	**J_{SC}(mA/cm^2)**	**V_{OC} (mV)**	**FF**	**η (%)**
First generation solar cells				
Si (crystalline)	42.2	706	0.83	24.7
Si (multicrystalline)	38.1	654	0.80	19.8
Si (thin-film transfer)	32.8	645	0.78	16.6
Second generation solar cells				
GaAs (crystalline)	28.2	1022	0.87	25.1
GaAs (thin film)	27.6	1011	0.84	23.3
InP (crystalline)	29.3	878	0.85	21.9
CIGS	35.7	669	0.77	18.4
CdTe	26.7	845	0.76	16.5
Si (nanocrystalline)	24.4	539	0.77	10.1
Third generation solar cells				
Dye sensitized solar cell	19.4	795	0.71	11.0
Dye sensitized solar cell (sub-module)	11.3	795	0.59	4.7

Michael Gratzel and co-workers at the Ecole Polytechnique Federale de Lausanne succeeded for the first time to produce what is known as “Gratzel Cell” or the dye sensitized solar cell (DSSC) by sensitizing a nanocrystalline TiO_2 film using novel Rubipyridl complex [16]. In dye sensitized solar cell, charge separation is

accomplished by kinetic competition like in photosynthesis leading to photovoltaic action. It has been shown that DSSCs are promising class of low cost and moderate efficiency solar cells, with simple manufacturing procedures based on organic materials [15].

1.3.3 Dye sensitized solar cells

Dye sensitized solar cell (DSSC) - a prominent member of the group of thin film photovoltaics, and as a new innovative technology - is developing very quickly and has been subject of increasing laboratory research since its discovery. Unlike the crystalline and thin film solar cells that have solid-state light absorbing layers, dye sensitized solar cells have their active component in the liquid phase. They use a dye sensitizer to absorb the light and create electron-hole pairs in the nanocrystalline semiconductor layer.

DSSC are a promising potential replacement for silicon-based solar cells. With advancements in nanostructured semiconductors, high-efficiency sensitizers and robust electrolytes, the performance of modern DSSCs is becoming more and more competitive. DSSCs do not require complex manufacturing processes and are mechanically robust, lightweight and semi-flexible, which make them suitable for low-density applications, such as rooftop collectors, where traditional silicon-based solar cells cannot be used. Simple processing, low-cost materials and a wide range of applications are all helping DSSCs to find a foothold in the marketplace [17].

A DSSC is composed of a dye adsorbed semiconductor (TiO_2, ZnO, SnO_2, etc.) electrode, a liquid electrolyte containing the redox couple I^-/I_3^- sandwiched between glasses having transparent conductive oxide (TCO) layer. The dye, on the electrode, absorbs light and injects electrons into the conduction band of the semiconductor. The

electron is then collected by a conducting glass and further supplied to load. The electrolyte reduces the oxidized dye, thus completing the redox cycle [16].

1.3.3.1 Composition of dye sensitized solar cells

The DSSC consists of the following components (as also shown in figure 1.2):

(1) Fluorine-doped SnO_2 (FTO) glass substrate

(2) Semiconductor film

(3) Sensitizer

(4) Electrolyte

(5) Counter electrode

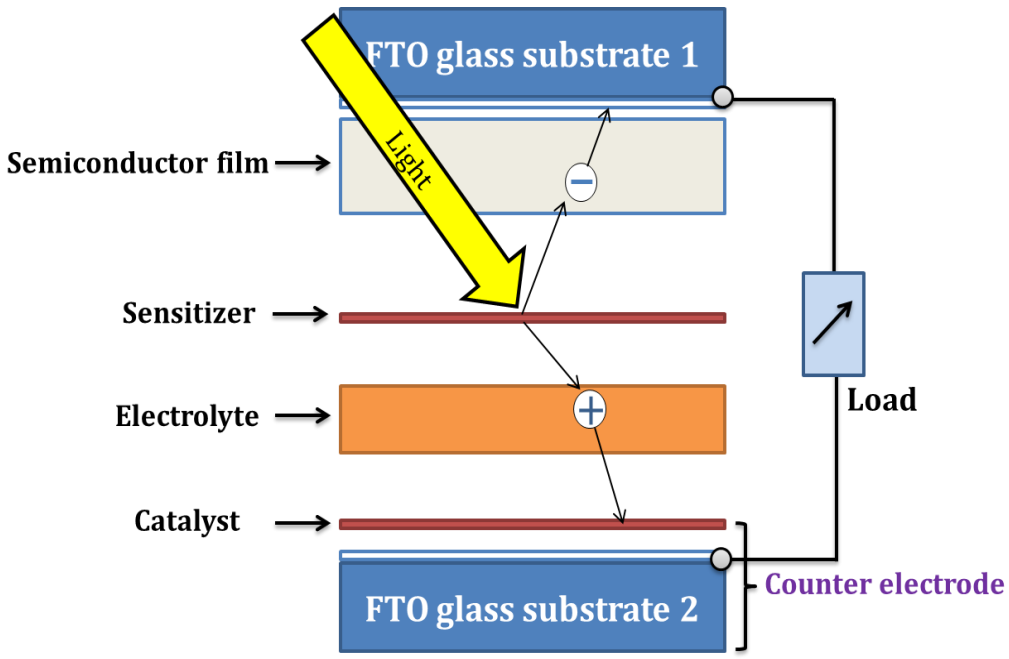

Figure 1.2 Composition of dye sensitized solar cell

1.3.3.2 FTO glass substrate

Glass substrates are commonly used as substrate because of their relatively low cost, availability and high optical transparency in the visible and near infrared regions. FTO

conductive film in the form of thin layer is deposited on one side of the substrate. The conductive film ensures low electric resistance per square. Typical value of such resistance is 10-20Ω/square at room temperature. The nanostructured semiconductor oxide (electron acceptor) is applied on the conductive side. Before assembling DSSC, the counter electrode (CE) is coated with a catalysing layer such as graphite, platinum to facilitate electron donation mechanism to the electrolyte, as will be discussed under section 1.3.3.7.

1.3.3.3 Semiconductor film

In DSSC, the semiconductor is used for charge transport, the photoelectrons are provided from a separate photosensitive dye [18]. Photoelectrodes made of materials such as Si, GaAs, InP, and CdS decompose under irradiation in solution owing to photo-corrosion [19]. In contrast, oxide semiconductor materials, such as TiO_2, ZnO and SnO_2 have good chemical stability under visible irradiation in solution; additionally, they are nontoxic and inexpensive. The TiO_2 thin-film photoelectrode is prepared by a very simple process. TiO_2 colloidal paste is coated on a TCO substrate and then sintered at 450 to 500° C, producing a TiO_2 film about 10 μm in thickness. This film is composed of TiO_2 nanoparticles (10–20 nm), giving it a nanoporous structure. The dye is adsorbed on the TiO_2 surface in a monolayer. The nanoporous TiO_2 film has a high roughness factor (>1000), the amount of dye adsorbed is drastically increased (on the order of 10^{-7} mol cm^{-2}), resulting in an increase of LHE, i.e., near 100% at the peak absorption wavelength of the dye. In comparison, the amount of adsorbed dyes on the surface of single-crystal and polycrystal materials is quite small, with only 1% LHE even at the peak wavelength [19].

1.3.3.4 Importance of the Nanostructure

During the last two decades nanomaterials have emerged as the new building blocks to construct light energy harvesting assemblies. Materials scientists have found that it is possible to design photovoltaic solar cells using nanotechnology-based semiconductor materials such as nanowires, nanocrystals, nanorods, nanodots. Use of the nanostructured material in solar cells reduces the cost and increases its conversion efficiency. New capabilities enabled by the unique performance enhancements of nanostructured materials promise to revolutionize the technology landscape. Nanostructured materials are those having atleast one dimension of 100 nm or less; they can be in the form of nanoparticles, nanorods, nanowires, thin films, and bulk materials made of such structures [20]. The properties such as optical, electronic, chemical, physical, electrical, magnetic of nanostructures are entirely different from those of their bulk counterparts with the same chemical composition [21]. This extraordinary aspect at nanoscale is related to their small size and large surface to volume ratio [22]. In nanocrystals, the electronic energy levels are not continuous as in the bulk but are discrete. This is because of quantum confinement - confinement of the electronic wave function to the physical dimensions of the particles. Suitable control of the properties and response of nanostructures can lead to new devices and technologies. The nanocrystalline morphology of the oxide semiconductor film is essential for the efficient operation of the DSSC. On a flat surface, a monolayer of dye can absorb hardly 1 % of the incident light [23]. Employing a nanoporous semiconductor oxide, with a roughness factor of approximately 10^3, dramatically increases the light harvesting efficiency enabling to overcome the notorious inefficiency problem. A whole range of nanostructures has been tested thus far, ranging from simple assemblies of nanoparticles to nanorods and nanotubes [24].

Third generation contains a wide range of potential solar innovations including polymer solar cells, nanocrystalline cells, and dye-sensitized solar cells.

1.3.3.5 Sensitizer

Charge separation occurs at the surfaces between the dye, semiconductor and electrolyte. As one of the crucial parts in DSSC, the photosensitizer should fulfil some essential characteristics. (1) the photosensitizer should have the absorption spectrum that lies in the visible to near-IR region (2) the photosensitizer should strongly bind to the semiconductor surface (3) for dye regeneration, the oxidized state level of the photosensitizer must be more positive than the redox potential of electrolyte (4) the photosensitizer should be photostable, as well as electrochemical and thermal stability are also required [25].

Among the metal complexes, ruthenium (Ru) complexes have shown the best photovoltaic properties: a broad absorption spectrum, suitable excited and ground state energy levels, relatively long excited-state lifetime, and good electrochemical stability.

1.3.3.6 Electrolyte

The electrolyte takes care of the charge transport between the two electrodes in DSSC. Basic electrolyte essentially consisted of an organic solvent and a dissolved redox couple; the iodide/triiodide system. This electrolyte has over the years been optimized by the inclusion of various additives, having an effect on both electrode surface electronics and structure, as well as on the electrolyte chemistry itself [26]. The redox electrolyte should be chemically stable with low viscosity in order to minimize transport problems, and be a good solvent for the redox couple components

and various additives. Also, it does not cause dissolution of the adsorbed dye or the semiconducting material of the electrodes. As many organometallic sensitizing dyes are sensitive toward hydrolysis, water and reactive protic solvents are normally not optimal choices [25].

1.3.3.7 Counter electrode

One of the most important components of DSSCs is the CE which collects electrons arriving from external circuit and catalyses reduction reaction of triiodide ion. Thus, the CE should possess high catalytic activity and high electrical conductivity for efficient charge transport [27]. The main requirements for the counter electrode materials used for the iodide/triiodide reduction are a low charge transfer resistance and good chemical and electrochemical stability of the platinum/electrolyte interface. In these terms platinum is an advantageous electrode material, because of its excellent electrochemical performance. Platinum (Pt) is a superior catalyst used as CEs in DSSCs. Several other materials, such as carbon materials, metal oxide, conductive polymers, transition metal carbides, and low cost quaternary chalcogenide materials have been used as catalyst material in DSSCs [27]. The role of Pt in the counter electrode of a DSSC is to catalyse the reduction of triiodide (I_3^-) ions that are produced by the oxidation of iodide (I^-) ions in the electrolyte by the oxidized dye. Platinized FTO glass has been the preferred combination for the counter electrode of a DSSC, due to the excellent catalytic activity of Pt for the reduction of I_3^- ions and due to its light reflecting nature. Pt can be deposited using a range of methods such as electro-deposition, spray pyrolysis, sputtering, and vapor deposition. Best performance and long-term stability has been achieved with nanoscale Pt clusters prepared by thermal decomposition of platinum chloride compounds [28]. Pt films

prepared by other methods such as electrodeposition and vapor-deposition on TCO substrates were found to dissolve in iodide/triiodide electrolytes and are therefore not suitable as counter electrodes in DSSCs.

1.3.3.8 Mechanism of DSSC

DSSC consists of a substrate of FTO conducting glass, a nanoporous semiconductor oxide film sensitized by a dye for absorbing visible light, a redox electrolyte for deoxidizing oxidized dye, and a platinized cathode to collect electrons and catalyse the redox couple regeneration reaction, as shown in figure 1.3. In DSSCs, the light-active component of the cell is a molecular dye which is anchored to the semiconductor surface. After being excited by a photon, the dye molecule injects the photoexcited electron to the conduction band of the semiconductor. The semiconductor then transfers the electron to FTO and it reaches the counter electrode after working on load. The oxidized dye is regenerated by reduction of I^- ions in the electrolyte. The I^- ion is restored by the reduction of I_3^- at the cathode. Thus the electric circuit is completed by diffusion of I^- and I_3^- from and to the counter electrode, respectively. Overall, DSSC produces electric power from light without suffering any permanent chemical transformation [23].

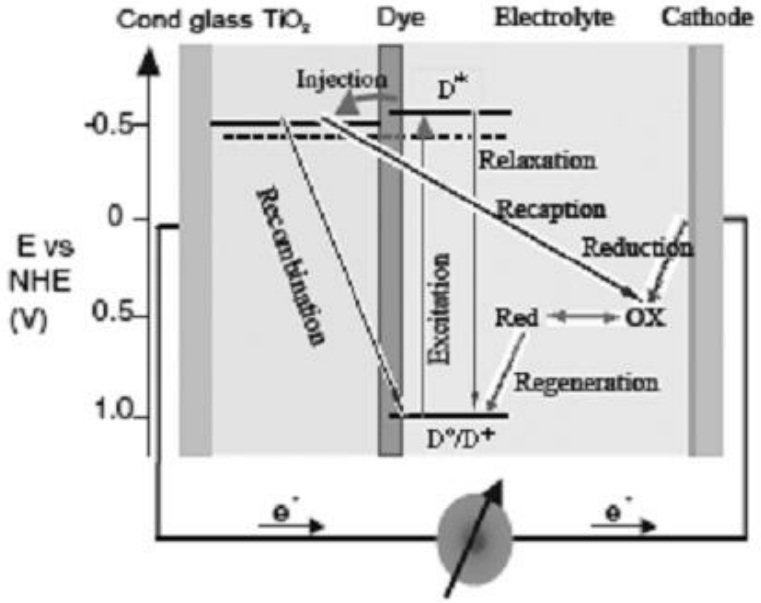

Figure 1.3 Principle operation of dye sensitized solar cell [23]

The various reactions taking place in DSSCs are given below:

(a) **Excitation of dye:** Sunlight passes through the TCO and excites the electron of the dye molecule from the HOMO level to the LOMU level.

$$hv + dye \rightarrow dye^{*} \quad (1)$$

(b) **Electron injection:** Transfer of electron from LUMO level of excited dye to conduction band of semiconductor takes place.

$$dye^{*} + semiconductor \rightarrow e^{-}(TiO_2) + dye^{+} \quad (2)$$

(c) **Working on load:** Electron reaches FTO, and, then, working through the load, it moves to the counter electrode.

$$e^{-}(TiO_2) + FTO \rightarrow TiO_2 + e^{-}(FTO) \quad (3)$$

(d) **Regeneration of dye:** The photoexcited dye gets regenerated by the oxidation of I^{-} to I_3^{-}.

$$3I^{-} + 2dye^{+} \rightarrow I_3^{-} + 2dye \quad (4)$$

(e) **At counter electrode:** The Pt catalyst reduces I_3^{-} to I^{-} at the counter electrode.

$$I_3^- + 2e^-(C.E.) \rightarrow 3I^- + (C.E.) \quad (5)$$

Besides the above processes, electron at the conduction band of semiconductor can also recombine with I_3^- in the electrolyte, leading to the reduced performance of a DSSC. Therefore, the performance of DSSCs is actually determined by the competition between the desired processes of forward electron injection and transport and the unwanted backward electron recombination [29].

1.3.3.9 Artificial Photosynthesis

DSSC technology arose from the concept of "artificial photosynthesis" - attempting to replicate the ability of plants to turn sunlight into useful energy. In DSSCs, chlorophyll is replaced by a light absorbing dye, the molecules of which are excited into a higher energetic state by incoming light. This energy is collected by a structure of electrolytes and catalysts, much like the surrounding structure of a leaf in photosynthesis [17].

1.3.4 Recent Advances in DSSCs

Advances in DSSCs research have produced designs for cells which may eventually rival silicon cells for conversion efficiency, making them a serious competitor to the current commercial technology. Presently, dye-sensitized solar panels convert about 11 – 12% of the sunlight striking them, into electricity. The researchers are trying to increase the efficiency and make it comparable with silicon-based solar panels.

Michael Gratzel in 1991 was the first to introduce dye sensitized solar cell based on nanoporous film of TiO_2 [16]. Since 1991, various high surface area electrodes of wide band gap semiconductors have been tested in DSSCs starting with TiO_2 [16], through SnO_2 [30,31], ZnO [32,33], Nb_2O_5 [34,35], $SrTiO_3$ [35] etc.

The most extensively applied and successful material so far is the high bandgap semiconductor TiO_2, which has achieved highest efficiency of 11%. TiO_2 remains the most commonly employed semiconductor because its conduction band energy is in a region accessible to many types of dyes, and it has useful surface chemistry and excellent materials properties [36]. Among other materials ZnO is getting more attention because of the similar energy level position of the conduction band as of TiO_2. In addition, the electron mobility and the electron transfer process from the excited dyes are similar [37].

Extensive research is being carried out on dyes, semiconductor oxides, and redox electrolytes and porosity of electrodes to further enhance the DSSC efficiency [25, 38, 39].

Also different morphologies such as nanorods [40], nanowire arrays [41], nanoflowers [42], ellipsoidal shaped nanoparticles [43], tetrapods [44] of ZnO and TiO_2 have been employed as photoanode for fabrication of dye sensitized solar cells.

Most of the present research on DSSCs is focused on improving spectral absorbance by making modifications in the dye, enhancing hole transport, replacement of the liquid electrolyte with conducting polymers or ionic solids and improving electron transport using alternative core-shell structures or wide band gap semiconductor materials.

One source of energy loss in DSSC is the charge recombination processes predominantly occurring at the semiconductor/dye/electrolyte interface. On illuminating with light, the electron in the conduction band of TiO_2 can either de-excite to the HOMO level of dye (recombine with oxidized dye molecule) or recombine with the electrolyte ions (redox species) present in the system [45]. However, charge recombination can also occur at the TCO glass support, where

oxidized species, in the electrolyte, can be reduced by electrons flowing out of the cell [46]; the overall effect being a reduction in the device current. This interfacial charge recombination still remains one of the major limiting factors to the efficiency of DSSCs.

To reduce this unwanted recombination, various methods have been tried by different research groups. One approach is to coat the TCO with a thin compact blocking layer of TiO_2 through hydrolysis of $TiCl_4$ solution. The researchers demonstrate that a compact blocking layer on the TCO significantly improves the performance of DSSCs [47]. Another approach is to modify the surface of the nanoporous TiO_2 film with certain materials, and, thus, build an energy gradient on the surface of the electrode to reduce the recombination [48]. In addition, doping ions like Fe, S, N have been found to increase the photoactivity because these ions not only reduce the recombination of electron and hole, but also extend the absorption wavelength to the visible region [3, 49,50]. Another method involves deposition of an oxide layer onto the surface of TiO_2 nanoparticles to improve the performance of the DSSC through interaction on the surface.

The literature reveals an increasing interest in the approach that is to grow a thin coating layer of oxide having a higher band gap on the nanoparticles. Coating on the surface of nanoparticles acts as an energy barrier at the electrode/electrolyte interface, which reduces this interfacial recombination process in DSSC. Suppression of charge recombination at semiconductor/dye/electrolyte interface can be achieved by coating a higher band gap oxide layer on the semiconductor, which allows the electrons generated upon photo-excitation of the dye to tunnel through the coating to the semiconductor, thereby retarding the back transfer of electron to the electrolyte solution [51-54]. However, the thickness of the coating layer should be appropriate

(less than or equal to 1nm), or else the chance of the electron injection into the semiconductor would be reduced. Over the past twenty years, a number of high band gap materials such as MgO [55,56], SnO_2 [57], Al_2O_3 [58], $MgTiO_3$ [59], rare earth oxides [60-62] have been used as coatings on semiconductor oxides (ZnO, TiO_2) and their effect on the performance of DSSCs has been investigated. However, there has been relatively little attention paid to structural, morphological and optical characterization of the $CaCO_3$ and Eu_2O_3 coated ZnO and TiO_2 nanoparticles for application as photo-anode in DSSCs.

Rare-earth oxides have aroused extensive interest and research due to their specific 4f electronic structure, high band gap and unique photo-electro and magneto properties [60-62]. The rare earth oxide layer forms energy barrier on nanoparticles, which effectively inhibits the surface charge recombination and improves the energy conversion efficiency of the DSSCs. The dye adsorption and light harvesting capability of electrodes are also increased by coating of rare earth oxides, which enhances the photocurrent density and the open-circuit voltage of the DSSCs. Rare earth oxide, coupled with semiconductor, induces energy band bending in the junction region which facilitates its photo-activity under visible light irradiation. This has been a motivation for the present work. Yu et. al. [60] investigated the effect of La_2O_3 coating on TiO_2 nanoparticles and found that La_2O_3 layer acts as the electrode-electrolyte recombination barrier and its presence improves the DSSC efficiency. The photoelectrochemical properties of rare earth ions (La, Ce, Nd, Sm and Gd)-modified ZnO films based DSSC were explored and compared by Lu et al. [61]. Zalas et al. [62] studied the electrochemical properties of DSSC fabricated using lanthanide ions (Ce, Yb, Sc, Y, Pr, Sm, Eu, Gd, Dy, and Tm)-modified TiO_2 films. Reports are available on the synthesis of Eu_2O_3/ZnO nanostructures and investigation of their

structural, optical, and morphological properties [63-65]. But to the best of our knowledge, no report on the synthesis of Eu_2O_3-coated ZnO and TiO_2 nanoparticles for the application as photo-anode in DSSC has been found in the literature. In the present study, Eu_2O_3 has been selected as the coating material, due to its high band gap (4.1 eV), and isoelectric point (IEP), i.e., 8.0, which assists the dye adsorption [66,67].

There have been significant reports on coating TiO_2 with large band-gap semiconducting metal oxides, but a little attention has been paid to electronic-insulating materials as the coating layer to retard the charge recombination in DSSCs. $CaCO_3$ is one of the electronic insulator materials. Coating semiconductor with $CaCO_3$ may be effective to physically separate the injected electrons and electron acceptors and hence retard the charge recombination in DSSCs. Wang et al. used TiO_2 nanocrystalline electrode coated with $CaCO_3$, sensitized with N719 as photoanode in DSSC, and revealed an improvement of 14.4% in efficiency as compared to that of bare TiO_2 based DSSC, using an antireflective film on the cell surface [68]. S. Lee et al. have reported the optical and electrical investigations on $CaCO_3$ coated TiO_2 nanoparticles as well as the improvement in the energy conversion efficiency, by 2.4%, of $CaCO_3$ coated TiO_2 based DSSC as compared to that of TiO_2 based DSSC [69,70]. In the present study, $CaCO_3$ has been selected as the coating layer, due to its high band gap (6.0 eV), and IEP (8.3) [68-70].

This thesis presents the synthesis of $CaCO_3$ and Eu_2O_3 coated ZnO and TiO_2 nanoparticles by chemical synthesis route as well as the investigations of structural, morphological and optical properties of the synthesized nanoparticles. These nanoparticles have been employed as photoanode in DSSCs, and their photocurrent density-voltage (J-V) characteristics have been studied.

Chapter-2

Materials and characterization

Chapter-2

With significant media attention focused on nanoscience and nanotechnology in recent years, materials science is becoming more widely known as a specific and unique field of science and engineering. Syntheses of nanoparticles allow the development of new functional materials which have raised attention for both scientific and industrial applications. The understanding of key parameters such as structure, chemical composition and investigation of interfaces provide base for their various applications. The basis of materials science involves relating the desired properties and relative performance of a material in a certain application to the structure of the atoms and phases in that material through characterization.

2.1 Introduction

In DSSC, among all the components, semiconductor oxide film plays a very significant role. This is because photovoltaic performance depends considerably on kind of inorganic material, morphology of nanoparticles, band gap and film porosity. In DSSC, the semiconductor oxide film bears three major functions: (i) providing a substrate for dye adsorption, (ii) harvesting the electrons injected from the dye, and (iii) transporting the electrons toward the load through FTO [18]. Semiconductor metal oxide materials must have properties of high surface area, high electron mobility and good reactivity with sunlight. Also, the band energy levels of the semiconductor must match with those of dye molecules to improve the separation of photogenerated charges and minimize the e^-/h^+ recombination [71]. In addition, the surface microstructures, particle size and shape, doping concentration, porosity, and film thickness of semiconductors must also be considered and optimized. Among the several candidates for photoanode materials, TiO_2 and ZnO have been usually adapted as appropriate materials for DSSC since they have demonstrated best performance

compared to other oxide materials. These two materials have been taken for the present study and are discussed in detail as follows:

2.2 Titanium Oxide

Titanium oxide (TiO_2) is a stable, nontoxic oxide, having a high refractive index (2.5) and is widely used as a white pigment in paint, toothpaste, sunscreen, self-cleaning materials, and food. TiO_2 is a very well-known and well-researched material due to the stability of its chemical structure, biocompatibility, physical, optical, and electrical properties. Its photocatalytic properties have been utilized in various environmental applications to remove contaminants from both water and air. Since then, enormous efforts have been devoted to the research of TiO_2 material, which has led to many promising applications in areas ranging from photovoltaics and photocatalysis to photo-electrochromics and sensors. There is close match of the band gap of TiO_2 to energy of the electrons emitted by many of the metallo-organic dyes used as sensitizer in DSSC [19].

TiO_2 has been known to be the best semiconductor electrode material due to its chemical stability and excellent charge transport ability [72]. TiO_2 exists in three polymorphs: anatase, rutile and brookite (figure 2.1). Pure brookite phase is unstable and difficult to synthesize. Anatase is considered to be photo-active while rutile phase scatters light due to its high refractive index as compared to anatase. Pure rutile phase has limited photoactivity whereas it has a considerable contribution when mixed with anatase phase [73]. In general, TiO_2 is preferred in anatase form because of its high photocatalytic activity, which is due to its more negative conduction band edge potential, high specific area, photochemical stability as compared to other phases of TiO_2 [74].

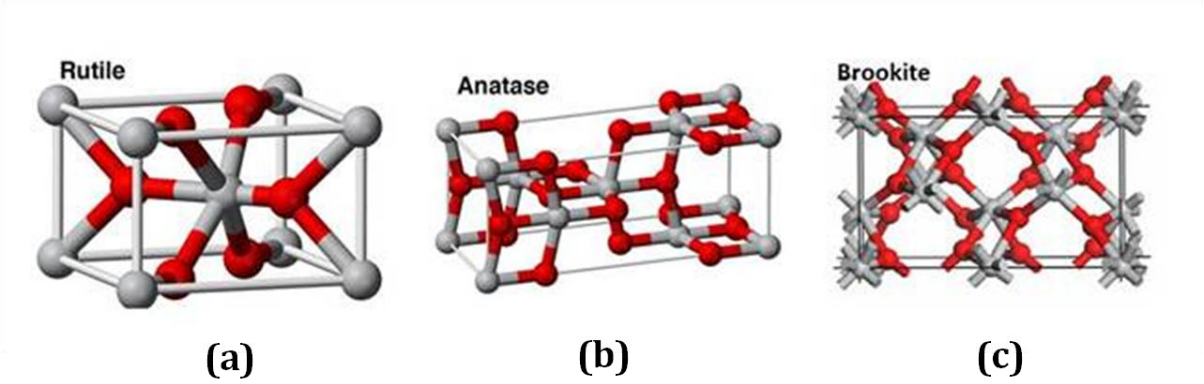

Figure 2.1 Unit cell of the (a) rutile (b) anatase and (c) brookite TiO_2 [75]

Various applications of TiO_2 nanoparticles are associated to its optical properties. However, due to its wide band gap, the highly efficient use of TiO_2 nanomaterials is sometimes prevented. The band gap of bulk TiO_2 lies in the UV regime (3.0eV for rutile phase and 3.2eV for anatase phase), which is merely (<10%) of the sun's energy [76]. To shift the absorbance onset of TiO_2 nanoparticles from UV to visible, various methods have been employed. Modification of the surface of TiO_2 nanoparticles with other semiconductors, doping of some elements, and metal-TiO_2 nanocomposites can change the charge transfer properties of TiO_2, thus improving the performance of TiO_2 nanomaterials based devices. Another approach is to sensitize TiO_2 with colourful inorganic or organic compounds that improve its optical activity in the visible region. Improvements to the TiO_2 in the DSSC have been made in terms of light absorption, light scattering, charge transport, interfacial kinetics, along with suppression of charge recombination [77].

Several methods to synthesize TiO_2 nanoparticles with controlled crystalline phase and size distribution, such as, chemical solution decomposition (CSD), chemical vapor decomposition, two-step wet chemical method, sol–gel, ultrasonic irradiation, hydrothermal method [78-80] have been reported.

In particular, the sol-gel process has attracted considerable attention due to the ease of controlling various parameters such as surface area, morphology, crystallite size,

crystallinity, and the phase structure of nanoparticles [81]. The sol–gel method is the most commonly used for the preparation of either bare TiO_2 or modified TiO_2. The advantage of the sol–gel method is that it facilitates the synthesis of nanometer sized crystallized TiO_2 powder of high purity at relatively low temperature [82].

In a typical sol-gel process, a colloidal suspension, called sol, is formed by the hydrolysis and polymerization reactions of the precursors, which are usually inorganic metal salts or metal organic compounds such as metal alkoxides. Complete polymerization and loss of solvent leads to the transition from the liquid sol into a solid gel phase. On heating the solid gel phase, nanoparticles can be obtained. The as-obtained TiO_2 nanoparticles are amorphous. The amorphous particles get converted to the crystalline phase on calcination. On calcination the phase variation along with the loss of OH and OR groups takes place, which plays a role in changing the surface and the photo-electrochemical properties of TiO_2 nanoparticles. The amorphous TiO_2 gets converted to anatase and as the calcination temperature is increased, anatase starts transforming to rutile. However, the reported transition temperature varies in the range 400-1100°C, owing to the use of different precursors and processing techniques [83].

In the present study, TiO_2 nanoparticles have been synthesized with the sol-gel method from hydrolysis of a titanium precursor. This process normally proceeds via an acid-catalyzed hydrolysis step of titanium(IV) alkoxide followed by condensation.

2.2.1 Experimental procedure

2.2.1.1 Synthesis of TiO_2 nanoparticles

In a typical experiment, titanium isopropoxide was dissolved in 150 ml of anhydrous isopropyl alcohol. A second solution was prepared in which measured quantity of water was dissolved in 150 mL of anhydrous isopropyl alcohol. Both the solutions were covered and stirred rapidly using the magnetic stirrer to obtain the homogeneous solutions. The water solution was then added to the alkoxide solution under continuous stirring of 5 hour. As a result of hydrolysis of titanium isopropoxide, white coloured precipitates were formed. The reaction of hydrolysis of the titanium isopropoxide proceeds as follows [83]:

$$Ti(C_3H_7O)_4 + (2+n)H_2O \rightarrow TiO_2.nH_2O + 4C_3H_7OH$$

The precipitates were filtered, washed using deionized water and dried at 70°C to get the TiO_2 powder. The powder obtained was calcined at 450°C for 2 hour.

2.3 Zinc Oxide

Zinc Oxide (ZnO) is one of the group II-VI compound semiconductors, generally existing in two main forms: cubic zinc blende and hexagonal wurtzite structure (figure 2.2). The wurtzite structure is most stable at ambient conditions and thus most common. The wurtzite structure consists of a hexagonal unit cell composed of alternating planes of tetrahedrally coordinated oxygen and zinc atoms stacked along the c-axis in the [0001] direction [84]. Each of one type of atom is surrounded by four of another type and vice versa.

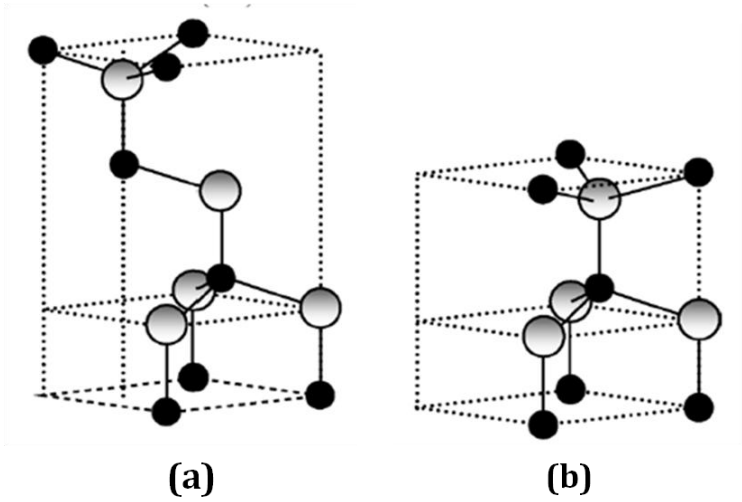

Figure 2.2 Crystal structure of (a) cubic zinc blende (b) hexagonal wurtzite zinc oxide [84]

ZnO is a wide-band-gap semiconductor that possesses an energy-band structure and physical properties similar to those of TiO_2, but has higher electronic mobility that is favorable for electron transport, with reduced recombination loss when used in DSSCs. Many studies have already been reported on the use of ZnO material for application in DSSCs. Although the conversion efficiency, 0.4–5.8%, obtained for ZnO is much lower than that of TiO_2 (11%); ZnO is still thought of as a distinguished alternative to TiO_2 due to its ease of crystallization and anisotropic growth. These properties allow ZnO to be produced in a wide variety of nanostructures, thus presenting unique properties for electronics, optics, or photocatalysis [85, 86]. In particular, recent studies on ZnO-nanostructure-based DSSCs have delivered many new concepts, leading to a better understanding of photoelectro-chemical based energy conversion. As ZnO is a direct wide band-gap (3.37 eV) biocompatible material having large excitation binding energy (60 meV) at room temperature, it is one of the most important semiconductor materials for applications in optoelectronics, sensors and actuators [87]. With these attributes, ZnO has been regarded as one of the most important nanomaterials in research and applications.

ZnO nanostructures have been synthesized into a variety of morphologies including nanowires, nanorods, tetrapods, nanobelts, nanoflowers and nanoparticles. ZnO nanoparticles can be obtained with different techniques such as, chemical precipitation, hydrothermal synthesis, chemical vapor deposition, and thermal oxidation [88]. The chemical precipitation method is the most popular method due to its low cost, reliability, and environmentally friendly synthetic routes. Moreover, this method provides rigorous control of the size and shape of the nanoparticles.

2.3.1 Experimental procedures

2.3.1.1 Synthesis of ZnO nanoparticles

The chemicals and reagents used for the synthesis were of research grade and used without purification. The synthesis of ZnO nanoparticles has been carried out using chemical precipitation method. In typical synthesis procedure, 0.1M of $Zn(CH_3COO)_2.2H_2O$ and NaOH were dissolved in water [89]. The addition of reactant solutions of zinc acetate and sodium hydroxide initiate the process of precipitation. The acetate group reacted with base, converting zinc acetate into zinc oxide. ZnO nanoparticles are originated from the product solution, during the process of precipitation. The mixture was stirred for 3 hour. So obtained particles were washed several times with ethanol and water, and dried at 60˚C for 12 hour and further, calcined at 300°C for 1 hour.

2.4 Fabrication of dye sensitized solar cell

The fabrication process of DSSC has been shown in figure 2.3 and discussed in detail as follows:

2.4.1 Cleaning of the FTO substrate

The fluorine doped tin oxide (FTO) glass substrates with dimensions 2 x 2 cm^2 have been used for the fabrication of DSSC. FTO glasses have been chosen as the

transparent conducting oxide because of the advantages in terms of sunlight transmittance and electrical conductivity. Cleaning of the substrates was done thoroughly using ethanol, acetone and distilled water assisted with ultrasonic treatment for 5 minutes in each bath, to completely eliminate mineral and organic contaminants.

2.4.2 Fabrication of photo-anode by doctor blade technique

Many methods are used to fabricate photo-anodes for DSSCs, including electrophoretic deposition (EPD), screen printing, and doctor blade deposition. The simplest and most widely used method for depositing semiconductor on the substrate is the so-called doctor-blade method.

Doctor blade technique is based on the principle of spreading the slurry through a moving blade onto a stationary substrate. In the doctor blade technique, well-mixed slurry consisting of particles along with additives such as binders, dispersants is placed on a substrate using the doctor blade. When a constant relative movement is established between the blade and the substrate, the slurry spreads on the substrate to form a thin sheet resulting in formation of film, with a thickness determined by a spacer. The simplest spacer is adhesive tape, which, on an average, is between 8 and 10 mm thick, and it is placed on opposite sides of the area where the film is to be laid, and the doctor blade is dragged across. The surface structure produced by this method is flat, with variations based on rolling technique, flatness of the spacing material, and position of the blade during the process. The doctor blade technique is suitable to coat the substrate with a very wide range of film thicknesses ranging from 20 to several hundred microns [90,91].

Typically with the FTO's conducting side facing up, two parallel strips of scotch tape on the edges of the glass plate were applied. Edges masked by the tape give the space

for electrical contacts. To make homogeneous slurry, synthesized nanoparticles were mixed with water, acetylacetone and triton-X 100 in pestle and mortar. On the top edge of the uncovered area of the FTO, slurry of the semiconductor nanoparticles was applied. The slurry was then spread across the FTO using a microscope slide by means of doctor blade technique. Thin films of area 1 x 1 cm^2 were prepared, dried at room temperature, followed by sintering at 450°C for 30 minute.

2.4.3 Dye sensitization

A dye solution was made by dissolving N719 dye powder in 20mL of ethanol in a container and stirred until no traces of solid were visible. The solution becomes deeply coloured very quickly even when only a small amount of the dye has actually been dissolved. In this solution, the photo-electrode was slowly immersed with the semiconductor layer facing up. The electrode was kept in the dye solution for 12 hour for its sensitization, with container completely covered and kept in dark. Finally, the sensitized photo-electrodes were taken out and rinsed with ethanol to remove the unadsorbed dye [92].

2.4.4 Counter electrode

An efficient counter electrode for a DSSC consists of a thin platinum layer on the FTO substrate. The platinized counter electrode is typically prepared with thermal decomposition of isopropyl alcohol and platinum precursor solution on the substrate. In the present study, the counter electrode was made by spin coating 5mM $H_2PtCl_6.6H_2O$ in isopropyl alcohol on FTO glass. The electrode was dried at room temperature for 2 minutes, followed by sintering at 385°C for 15 minute.

2.4.5 Injection of electrolyte

The sensitized electrode and the counter electrode electrodes were put together with some space left for electrical contacts. The electrodes were held together with a binder

clip. A few drops of electrolyte comprising of LI, I_2, TBP, and TBAI, in acetonitrile were placed at the interface of the two glass plates with a dropper. The electrolyte gets drawn into the cell by capillary effect. The excess electrolyte was wiped off with tissue paper.

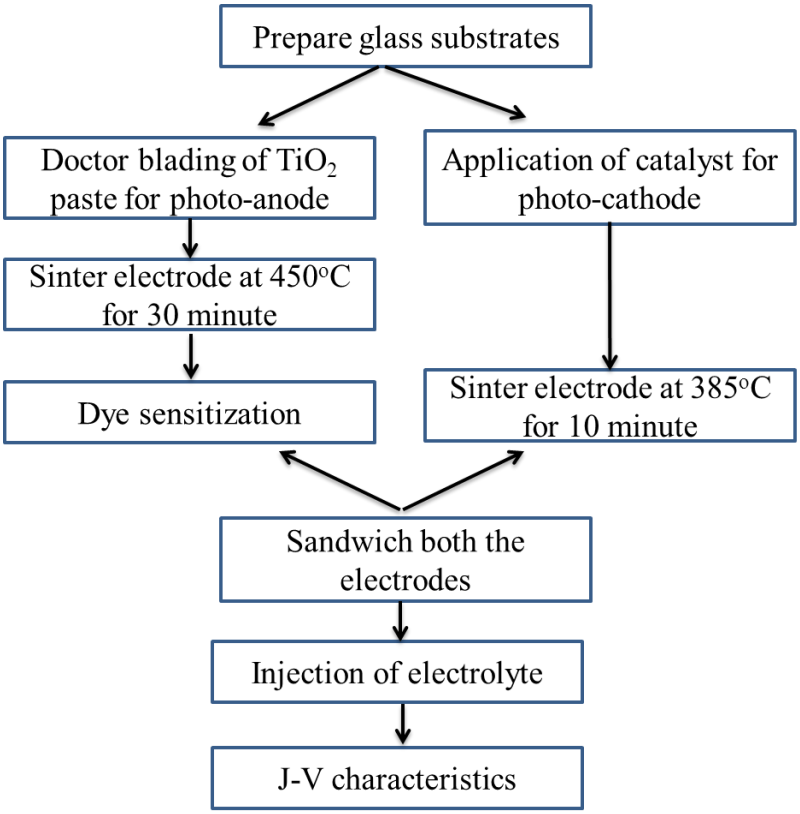

Figure 2.3 Flow chart of the procedure for the fabrication of DSSC

2.5 Characterization techniques

In materials science, characterization refers to the use of external techniques to probe into the internal structure and properties of the material. Characterization can take the form of actual materials testing or analysis, for example, in some form of microscope. Analysis techniques are used simply to magnify the specimen, to visualize its internal structure, and to gain knowledge as to the distribution of elements within the specimen and their interactions. Recent advances in nanotechnology have enabled materials and devices to be fabricated at the nanoscale. Several articles reveal how these improved tools enabled characterization of entirely new types of materials,

including nano-materials from quantum dots to nano-photonics to nano-composites, studies of spintronics and quantum-computing-related systems, and the extension of materials characterization techniques into areas that blur the boundaries between physics, chemistry and biology, just to name a few. New tools are being developed to meet the challenges of manipulating structures of nanomaterials.

2.5.1 X-ray diffraction

"Every crystalline substance gives a pattern; the same substance always gives the same pattern; and, in a mixture of substances each produces its pattern independently of the others"

2.5.1.1 Introduction

X-rays are electromagnetic radiation with energy in the range of 100eV - 100keV. Because the wavelength of x-rays is comparable to the size of atoms, they are ideally suited for probing the structural arrangement of atoms and molecules in a wide range of materials. X-ray diffraction (XRD) technique uses x-rays to investigate and quantify the crystalline nature of materials by measuring the diffraction of x-rays from the planes of atoms within the material.

2.5.1.2 Theory and methodology

When an x-ray beam strikes a sample and is diffracted, the distances between the atomic planes can be measured by applying Bragg's Law (figure 2.4), the equation of which is stated as

$$n.\lambda = 2d\ sin\theta$$

where n is the order of the diffracted beam, λ is the wavelength of the incident x-ray beam, d is the distance between the adjacent atomic planes and θ is the glancing angle of the x-ray beam. Since λ and θ are known, interplanar spacing can be calculated.

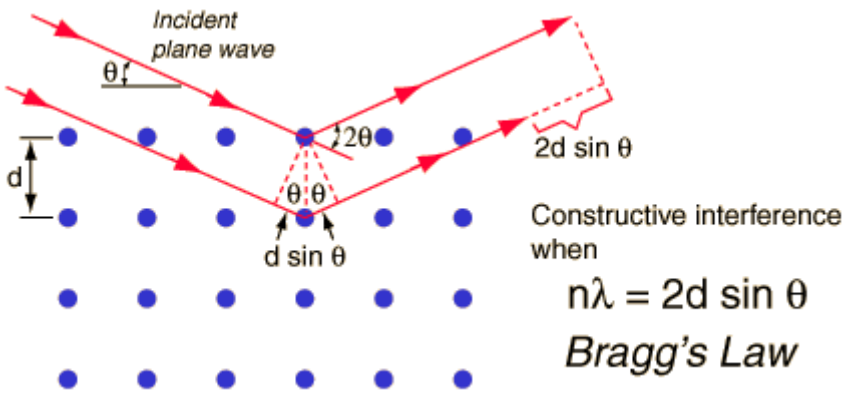

Figure 2.4 Bragg's law of diffraction [93]

2.5.1.3 Instrumental and working of XRD

X-ray diffractometer consist of three basic elements: an x-ray tube, a sample holder, and an x-ray detector. X-rays are generated within a sealed tube which is under vacuum. On applying current, the filament gets heated within the tube; the higher the current, the greater are the number of electrons emitted from the filament. These x-rays are collimated and directed onto the sample. As the sample and detector are rotated, the intensity of the reflected x-rays is recorded. When the geometry of the incident x-rays impinging the sample, satisfies the Bragg's Equation, constructive interference occurs. A detector records and processes this x-ray signal and converts the signal to a count rate which is then output to computer monitor [94]. The pictorial view of x-ray diffractometer is shown in figure 2.5.

Figure 2.5 Pictorial view of x-ray diffractometer

2.5.1.4 Sample preparation

For XRD, the sample is grounded down to produce particle size less than 10 microns. The sample is the pressed into a sample holder in order to have a smooth flat surface.

2.5.1.5 Information from XRD

The XRD pattern that includes position and intensities of the diffracted beam, provides different information about the sample and are discussed below:

- The peak positions (2θ) and intensity values used to identify the type of material by comparing them with patterns in the International Powder Diffraction File (PDF) database, complied by the Joint Committee for Powder Diffraction Standards (JCPDS). By this method, identification of any crystalline compounds, even in a complex sample, can be made. Also, the purity of a sample and the composition of any impurities present can be determined from XRD diffraction pattern.

- Width of the diffracted peaks is used to determine the interplanar atomic spacing (d-spacing), crystallite size and micro-strain in the sample.

- A diffraction pattern can also be used to determine the lattice parameters of a crystal structure.

- The position of diffracted peaks also provides information about how the atoms are arranged within the crystalline compound (unit cell size or lattice parameter). The intensity information is used to assess the type and nature of atoms.

- The 2θ and intensity values of peaks from a phase can be used to quantitatively estimate the amount of that phase in a multi-component mixture [95].

In the present study, the nanoparticles have been characterized through XRD by PANalytical X'PertPRO MRD with CuKa (k = 1.54 A˚) radiation operated at 45 kV and 40 mA.

2.5.2 Scanning electron microscope

"Seeing is believing" therefore, imaging of nanomaterials is an essential part of nanoscience and nanotechnology.

2.5.2.1 Introduction

Scanning electron microscopy (SEM) reveals levels of detail and complexity of a material by using a focussed beam of electrons, which is unobtainable by light microscopy. SEM uses a focused beam of high-energy electrons to generate a variety of signals at the surface of solid specimens. SEM enables the investigation of specimens with a resolution down to the nanometer scale. Hardly any segment of high technology development - aerospace, electronics, energy, catalysis, environmental, photonics, chemicals - would be possible without the data provided by SEM. In

conventional SEM, which operates in high vacuum, the specimen has to be electrically conductive or coated with a conductive layer (e.g. Carbon, Gold etc.).

2.5.2.2 Theory and methodology

As accelerated electrons in the primary beam are scanned across the sample surface, the kinetic energy of the electrons gets dissipated and a variety of signals are produced by electron-sample interaction (figure 2.6). These signals include secondary electrons, backscattered electrons (BSE), diffracted backscattered electrons, photons, cathodoluminescence (CL), and heat. For imaging samples, secondary electrons and backscattered electrons are commonly used; the secondary electrons are most significant for showing morphology and topography of samples whereas the backscattered electrons are useful for illustrating contrasts in composition in multiphase samples. Consequently, the secondary electron micrograph is virtually a direct image of the real surface structure [96].

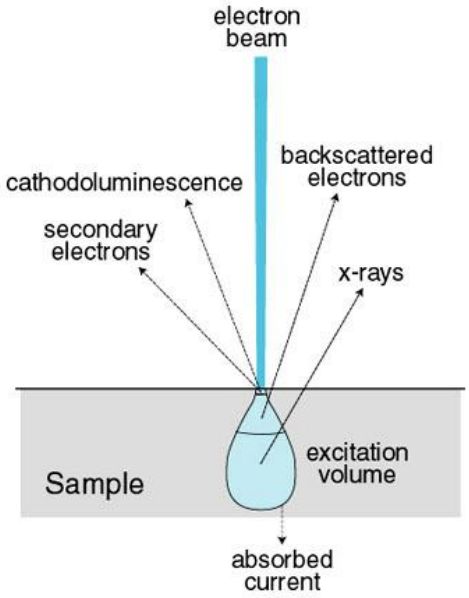

Figure 2.6 Signals produced by electron beam and sample interaction in SEM [97]

2.5.2.3 Instrumental and working

The diagram in figure 2.7 shows the major components of an SEM. These components are part of seven primary operational systems: vacuum, beam generation, beam manipulation, beam interaction, detection, signal processing, and display and record. These systems function together to determine the results and qualities of a micrograph such as magnification, resolution, depth of field, contrast, and brightness. A source of electrons is focused in vacuum into a fine probe that is rastered over the surface of the specimen. The electron beam passes through scan coils and objective lens that deflect horizontally and vertically so that the beam scans the surface of the sample. As the electrons penetrate the surface, a number of interactions occur that result in the emission of electrons or photons from the surface. A reasonable fraction of the electrons emitted can be collected by appropriate detectors, and the output can be used to modulate the brightness of a cathode ray tube (CRT) whose x- and y-inputs are driven in synchronism with the x-y voltages rastering the electron beam. In this way an image is produced on the CRT; every point that the beam strikes on the sample is mapped directly onto a corresponding point on the screen [98].

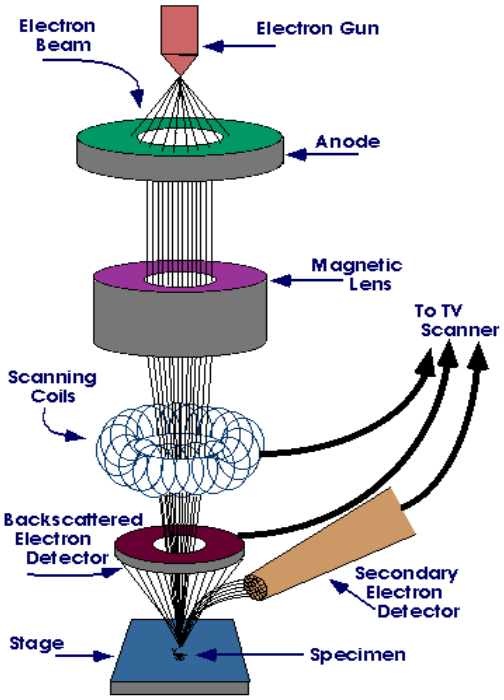

Figure 2.7 Working of SEM [99]

The attainable resolution of the technique is limited by the minimum spot size that can be obtained with the incident electron beam, and ultimately by the scattering of this beam as it interacts with the sample. With modern instruments, a resolution of better than 5 nm is achievable. Figure 2.8 shows the pictorial view of SEM.

Figure 2.8 Pictorial view of SEM

2.5.2.4 Sample preparation

In the present study, SEM has been used to analyse the morphology, porosity and homogeneity of the fabricated electrodes. The dried electrodes prepared form the synthesized nanoparticles were mounted on aluminium stub using double tape. Subsequently the electrode was coated with thin film of gold. The electrode was put into the jaw of sample holder of SEM for analysis.

2.5.2.5 Information from SEM

- SEM plays a key role in many topics of current interest such as nanotubes and nanofibres, high temperature superconductors, mesoporous architectures. The homogeneity, porosity and texture of the electrodes are determined by SEM analysis of the photo-electrodes.

- The investigation of grain size distributions and texture analysis can be done by SEM analysis.

In the present study, thin film of gold was coated using (JEOL, FINE SPUTTER JFC-1100) sputter coating unit and viewed under SEM (JEOL, JSM-6510LV).

2.5.3 Transmission electron microscope

2.5.3.1 Introduction

Transmission Electron Microscopy (TEM) is a technique where an electron beam interacts and passes through a sample. TEM is an immensely valuable and versatile technique for the characterisation of nanomaterials. It exploits the very small wavelengths of high-energy electrons to probe solids at the atomic scale. In addition, information about local structure (by imaging of defects such as dislocations), average structure (using diffraction to identify crystal class and lattice parameter) and chemical composition may be collected almost simultaneously.

2.5.3.2 Theory and methodology

TEM exploits various interactions of electron beam-specimen; unscattered electrons (transmitted beam), elastically scattered electrons (diffracted beam) and inelastically scattered electrons (figure 2.9).

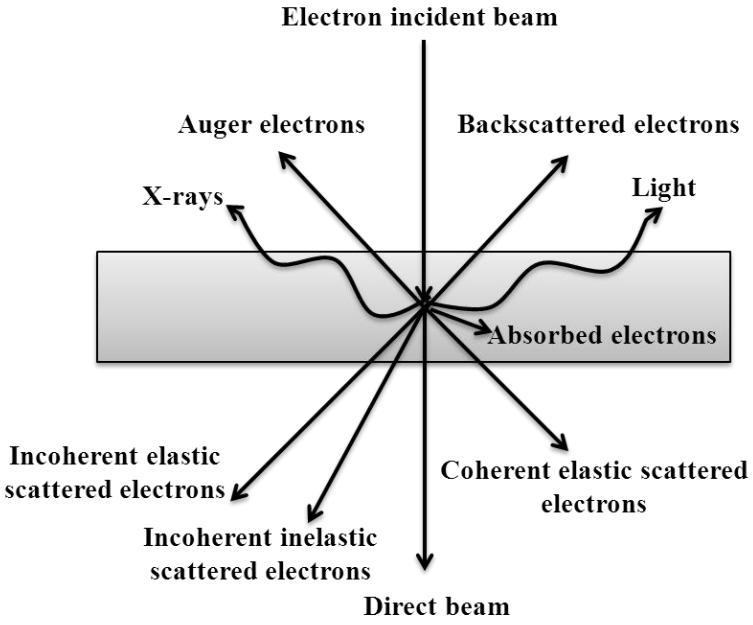

Figure 2.9 Signals generated by the interaction of electron beam and sample in TEM

When incident electrons are transmitted through the thin specimen without any interaction occurring inside the specimen, then the beam of these electrons is called transmitted. The transmission of unscattered electrons is inversely proportional to the specimen thickness. Areas of the specimen that are thicker will have fewer transmitted unscattered electrons and so will appear darker, conversely the thinner areas will have more transmitted and thus will appear lighter [98].

2.5.3.3 Instrumental and working

There are four main components of TEM: a vacuum system, an electron emission source for generation of the electron stream, a series of electromagnetic lenses and electrostatic plates (figure 2.10).

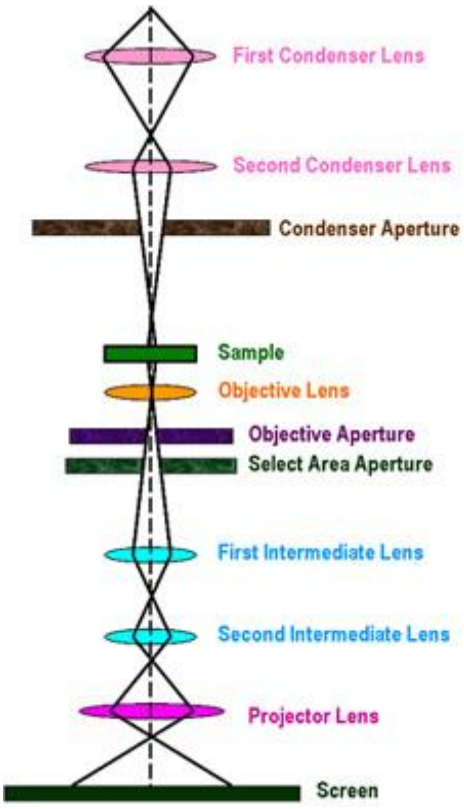

Figure 2.10 Working of TEM [100]

The latter two let the operator to guide and manipulate the beam as required. The electron beam emerges from the electron gun, and passes through a thin specimen, transmitting electrons which are collected, focused, and projected onto the viewing device at the bottom of the column. Imaging devices are subsequently used to create an image from the electrons that exit the system. The entire electron path from gun to camera is under vacuum. Figure 2.11 shows the pictorial view of TEM.

Figure 2.11 Pictorial view of TEM

2.5.3.4 Sample preparation

The powdered samples were ultrasonically dispersed in ethanol, and a drop of this solution was spread on carbon coated copper grid to view images.

2.5.3.5 Information from TEM

- TEM provides topographical, morphological, and crystalline information of the nanoparticles. From the TEM analysis, the size, shape, morphology and size distribution of the nanostructures can be determined.
- In TEM, regions with higher thickness or higher atomic numbers appear darker in the resulting image. This fact is used for imaging multi-component systems. Hence, the coating over the surface of nanoparticles can be easily established making the images more perceptive for interpretation.

- In high resolution transmission electron microscopy (HRTEM), the electron beam interactions with the atomic columns of a crystalline specimen leads to different contrast mechanism called phase contrast. This effect is used for imaging the atomic distances in a crystal. It gives an additional information like crystal lattice distances and interface information to a limit below 1 nm. An HRTEM can show details as small as a single column of atoms.

In the present study, TEM has been carried out using Hitachi H-7500.

2.5.4 Energy dispersive X-Ray analysis

"Compositional analysis allows one to identify what those particular elements are and their relative proportions"

2.5.4.1 Introduction

Energy Dispersive X-Ray Analysis (EDAX) is an analytical tool used to identify the elemental composition of materials. EDAX systems are attachments to SEM and TEM instruments where the imaging capability of the microscope identifies the specimen of interest. The data generated by EDAX analysis consist of spectra showing peaks corresponding to the elements making up the true composition of the sample being analysed.

2.5.4.2 Theory and methodology

When the sample is bombarded by the electron beam, electrons are ejected from the atoms comprising the sample's surface. The resulting electron vacancies are filled by electrons from a higher state, and an x-ray is emitted to balance the energy difference between the two states. Each element emits a different set of x-ray energy and is characteristic of the element from which it was emitted. EDAX detector separates the characteristic x-rays of different elements into an energy spectrum, and EDAX system

software analyzes the energy spectrum in order to determine the presence of specific elements (figure 2.12). Measuring these emissions provides both qualitative and quantitative information about the near-surface makeup of the sample [101].

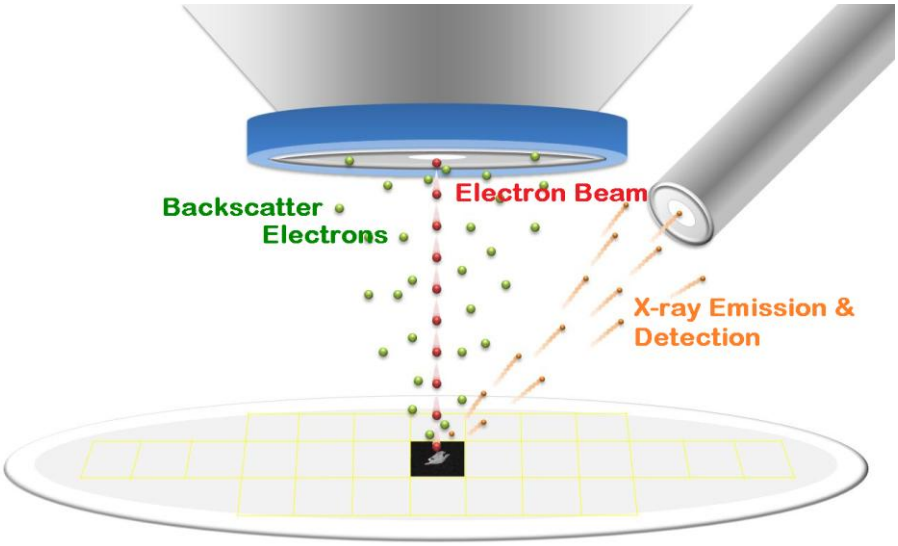

Figure 2.12 Signals generated by the interaction of electron beam and sample in EDAX [102]

EDAX is used to find the chemical composition of materials down to a spot size of a few microns, and to create element composition maps over a much broader raster area. Together, these capabilities provide fundamental compositional information for a wide variety of materials.

2.5.4.3 Instrumental and working

EDAX are integrated into SEM or TEM instruments. EDAX system include a sensitive x-ray detector, a liquid nitrogen dewar for cooling, and software to collect and analyze energy spectra. The detector is mounted in the sample chamber of the main instrument at the end of a long arm, which is itself cooled by liquid nitrogen. The most common types of detectors are made of Si(Li) crystals and silicon drift detectors. An EDAX detector absorbs the energy of incoming x-rays by ionization, yielding free electrons in the crystal that become conductive and produce an electrical

charge bias. The x-ray absorption thus converts the energy of individual x-rays into electrical voltages of proportional size; the electrical pulses correspond to the characteristic x-rays of the element [103]. The pictorial view of EDAX attached to SEM has been shown in figure 2.13.

Figure 2.13 Pictorial view of EDAX attached to SEM [104]

2.5.4.4 Sample preparation

The sample preparation for EDAX is same as for SEM. The dried electrodes prepared form the synthesized nanoparticles are mounted on aluminium stub. Subsequently the electrode is coated with thin film of gold. The electrode is put into the jaw of sample holder of SEM for analysis.

2.5.4.5 Information from EDAX

- EDAX is a powerful tool for contamination analysis and industrial forensic science investigations. The EDAX spectrum gives a quick compositional analysis.

- EDAX provides the spatial distribution of elements through mapping from which the homogeneity of multi-phase systems can be ascertained. Analysis of the resulting x-ray energy spectrum at each position provides plots of the relative elemental concentration variance for each element as a function of those position-point values along the given path.

In the present study, the quantitative elemental composition analysis has been carried out by energy dispersive X-ray spectroscopy (EDAX, OXFORD analytical), attached with SEM.

2.5.5 Photoluminescence spectroscopy

2.5.5.1 Introduction

Photoluminescence (PL) spectroscopy is a powerful optical method used for characterizing materials. A material absorbs light, creating an electron hole pair; an electron from the valence band jumps to the conduction band leaving a hole. The photon emitted upon recombination corresponds to the energy difference between the valence and conduction bands, and is hence lower in energy than the excitation photon.

2.5.5.2 Theory and methodology

When a photon strikes a sample having energy greater than the band gap energy, it gets absorbed and thereby an electron from the valence band up to the conduction band gets excited across the forbidden energy gap. In this process of photoexcitation, the electron generally has excess energy which it loses before coming to rest at the lowest energy in the conduction band. The electron eventually falls back to the valence band. As it falls down, the energy it loses is converted back into a luminescent photon which is emitted from the material. Thus the energy of the emitted photon is a direct measure of the band gap energy (E_g). The process of photon excitation followed by photon emission is called photoluminescence**.**

2.5.5.3 Instrumental and working

The design of fluorescence illuminators is based on control of excitation light and emission light by readily changeable filter insertions into the light path on the way toward the specimen and then emanating from the specimen.

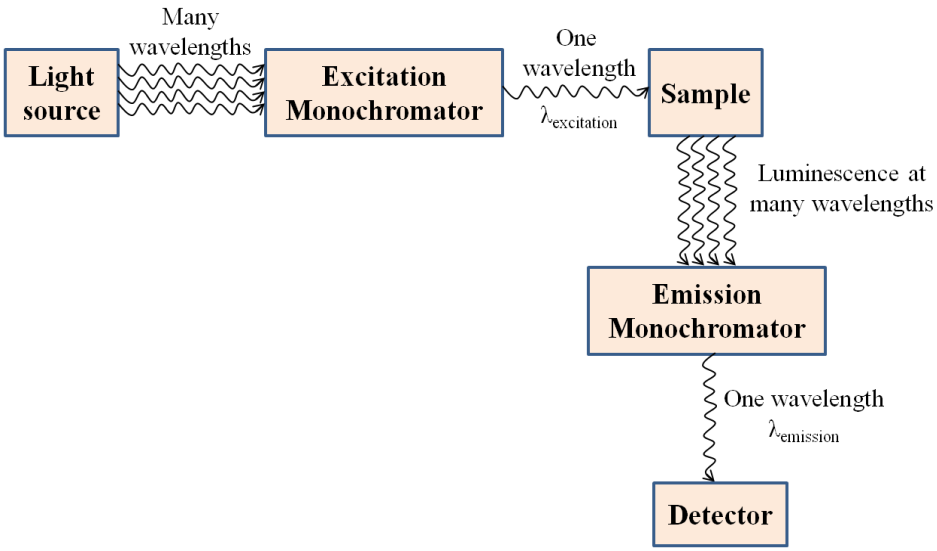

Figure 2.14 Working of PL spectrometer

It consists of four main components a light source, a sample, a light filtering system, and a light detector. The light from the source hits the sample which causes production of electron-hole pairs as well as electron interactions. Some of these interactions cause an emission of light, which is then filtered to its different energies and then recorded by the detector. A schematic of an emission experiment is illustrated in figure 2.14 and pictorial view of photoluminescence spectrometer is shown in figure 2.15. An excitation wavelength is selected by one monochromator, and luminescence is observed through a second monochromator, usually positioned at 90° to the incident light to minimize the intensity of scattered light reaching the detector. If the excitation wavelength is fixed and the emitted radiation is scanned, an emission spectrum is produced [105].

Figure 2.15 Pictorial view of photoluminescence spectrometer

2.5.5.4 Sample preparation

The sample for PL analysis was prepared by dispersing the nanoparticles ultrasonically in ethanol.

2.5.5.5 Information from PL

Impurity levels and defect detection: Radiative transitions in semiconductors also involve localized defect levels. The PL energy associated with these levels can be used to identify specific defects, and the PL intensity can be used to determine their concentration.

Recombination mechanisms: The emission process involves both radiative and non-radiative recombination processes. The PL intensity and its dependence on the level of photo-excitation and temperature are directly related to the dominant recombination process. Analysis of PL helps to understand the underlying physics of the recombination mechanism.

Material quality: In general, non-radiative processes are associated with localized defect levels, whose presence is detrimental to material quality and subsequent device performance. Thus, material quality can be measured by quantifying the amount of radiative recombination [106].

The PL spectra of the synthesized nanoparticles have been recorded using xenon lamp equipped in the Perkin Elmer fluorescence spectrometer.

2.5.6 Fourier transform infrared spectroscopy

2.5.6.1 Introduction

Fourier transform infrared spectroscopy (FTIR) is an analytical tool which provides the molecular and structural information of organic and inorganic materials. It is used to identify unknown materials, study the quality of materials, and understand mixtures of materials. Infrared light is absorbed within molecular bonds, causing the bonds to vibrate. Since different molecules have different bond energies, infrared absorption is a useful tool for both qualitative and quantitative analysis of samples. An infrared spectrum represents a fingerprint of a sample with absorption or transmission peaks which correspond to the frequencies of vibrations between the bonds of the atoms. Because each different material is a unique combination of atoms, no two compounds produce the same infrared spectrum. In addition, the size of the peaks in the spectrum is a direct indication of the amount of material present.

2.5.6.2 Theory and methodology

When the sample is exposed to infrared radiation, molecules selectively absorb radiation of specific wavelengths which causes the change of dipole moment of molecules. As a result, the vibrational energy levels of molecules transfer from ground state to excited state. The frequency of the absorption peak is determined by the vibrational energy gap. The number of absorption peaks is related to the number of vibrational freedom of the molecule. The intensity of absorption peaks is related to the change of dipole moment and the possibility of the transition of energy levels. Most molecules are infrared active except for several homonuclear diatomic molecules such as O_2, N_2 and Cl_2 due to the zero dipole change in the vibration and

rotation of these molecules. The common used region for infrared absorption spectroscopy is 4000 ~ 400 cm^{-1} because the absorption radiation of most organic compounds and inorganic ions is within this region.

2.5.6.3 Instrumental and working

The instrumentation of FTIR is derived from the classical attempt by Michelson to measure the ether wind. A typical FTIR spectrometer consists of a blackbody infrared (IR) source, a 50% beam splitter, a fixed and movable mirror and an IR detector (figure 2.16). Incoming IR beam is split in two parts by the beam splitter that reflects back from the fixed mirror and the movable mirror, respectively. The two reflected beams are combined at the beam splitter but the difference in path lengths creates constructive and destructive interference [107].

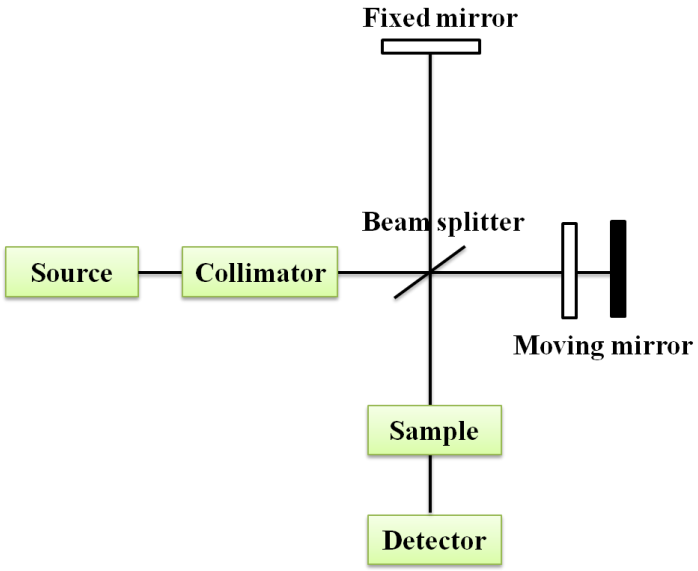

Figure 2.16 Block diagram of an FTIR spectrometer

After passing through the sample, the measured signal is called the interferogram. Performing Fourier Transform on this signal, results in the infrared spectrum. An FTIR Spectrometer collects and digitizes the interferogram, performs the FT function, and displays the spectrum. Figure 2.17 shows the pictorial view of FTIR spectrometer.

Figure 2.17 Pictorial view of FTIR spectrometer

2.5.6.4 Sample preparation

The standard method to prepare solid sample for FTIR spectrometer is to use KBr. About 2 mg of sample and 200 mg KBr were dried and ground. Then, the mixture was squeezed to form pellets, the FTIR was performed directly on the pellets.

2.5.6.5 Information from FTIR

- It can identify unknown materials. Individual absorption peaks can be identified and assigned to individual chemical bonds qualitatively or quantitatively to identify individual compounds in complex systems.

- It can determine the amount of components in a mixture

In the present study, FTIR spectroscopy of nanoparticle samples in the form of pellets has been carried out using Perkin Elmer 1615 spectrometer in the wave-number region of 400 – 4000 cm^{-1}.

2.5.7 UV-visible spectroscopy

2.5.7.1 Introduction

UV Visible spectroscopy studies the electronic transitions of molecules as they absorb light in the UV and visible regions of the electromagnetic spectrum. When radiation interacts with matter, a number of processes can occur (figure 2.18), including

reflection, scattering, absorbance, fluorescence/phosphorescence (absorption and reemission), and photochemical reaction (absorbance and bond breaking). In general, when measuring UV-visible spectra, only absorbance is allowed to occur. It involves absorption of ultraviolet or visible light by a molecule causing the promotion of an electron from a ground electronic state to an excited electronic state. UV-visible spectroscopy is a technique to determine the concentrations of substances and therefore enables to study the rates of reactions, and determine rate equations for reactions.

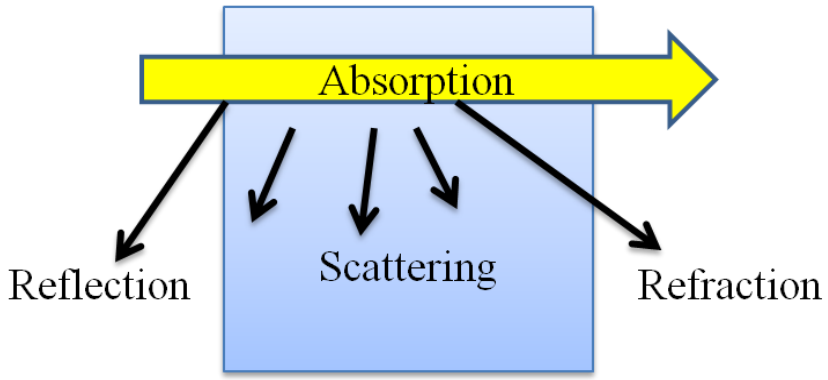

Figure 2.18 Different processes occur on light and matter interaction

2.5.7.2 Theory and methodology

When light passes through a sample (concentration, c) in cuvette (path length, b), the amount of light absorbed is the difference between the incident radiation (I_o) and the transmitted radiation (I) (Figure 2.19). The amount of light absorbed is expressed as either transmittance or absorbance. For most applications, absorbance values are used since the relationship between absorbance and both concentration and path length normally is linear.

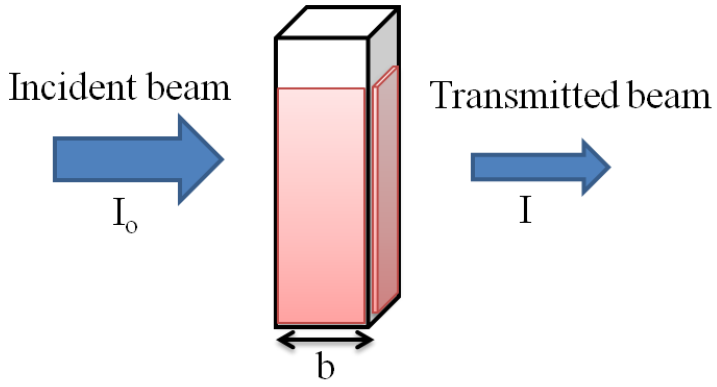

Figure 2.19 The graphic demonstration of Beer-Lambert Law

Transmittance (T) is defined in terms of fraction of 1 or as percentage and is defined as follows:

$$T = \frac{I}{I_o}$$

or $$\%T = \left(\frac{I}{I_o}\right) \times 100$$

Absorbance is defined as follows:

$$A = -\log T = log\left(\frac{I_o}{I}\right) = \varepsilon bc$$

where ε is the molar absorption or extinction coefficient. This expression is commonly known as Beer- Lambert law which states that the fraction of incident radiation absorbed is proportional to the number of absorbing molecules in its path. The greater the number of molecules that absorb light of a given wavelength, the greater the extent of light absorption and higher the peak intensity in absorption spectrum.

2.5.7.3 Instrumental and working

UV-visible spectrometers can be used to measure the absorbance of UV or visible light by a sample, either at a single wavelength or perform a scan over a range in the spectrum. A schematic diagram of a UV-visible spectrometer is shown in figure 2.20 and a pictorial view is shown in figure 2.21.

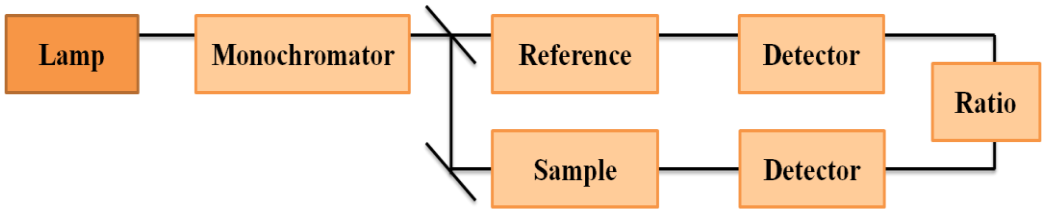

Figure 2.20 Working of UV-visible spectrometer

The light source is usually a deuterium lamp for UV measurements (190-400 nm) and a tungsten-halogen lamp for visible measurements (400-800 nm). For liquid samples, an optically flat, transparent container called cuvette is used. The reference cuvette contains the solvent in which the sample is dissolved and this is commonly referred to as the blank. The output from the light source is focused onto the monochromator which produces a beam of single wavelength, selected from a wide range of wavelengths. For each wavelength the intensity of light passing through both a reference cuvette (I_o) and the sample cuvette (I) is measured. The detector converts the incoming light into a current, the higher the current the greater the intensity. The chart recorder usually plots the absorbance against wavelength [108].

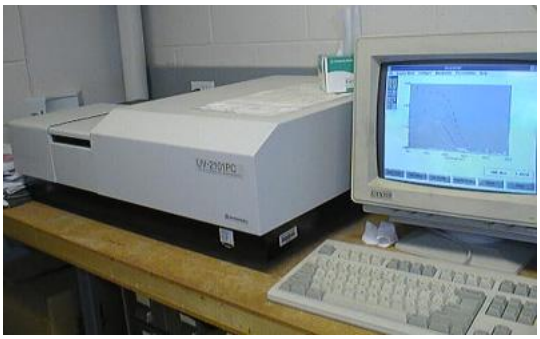

Figure 2.21 Pictorial view of UV-visible spectrometer

2.5.7.4 Sample preparation

For UV-Visible spectroscopy, the powdered sample is ultrasonically dispersed in ethanol. For the dye desorption studies, the electrodes were soaked in 0.1 mM aqueous NaOH solution. The UV-visible study is done on the desorbed dye solution.

2.5.7.5 Information from UV-Visible

- UV-visible analysis can be used to identify a compound by comparative analysis. UV visible spectrum of an unknown sample can be compared with the spectra of known suspects.
- Dye desorption studies: The amount of dye adsorbed on the fabricated electrodes is determined by the optical absorption spectra of dye-desorbed solution. The higher the intensity of UV-Visible spectrum, the more is the dye adsorbed on the electrode.

In the present study, UV–Vis absorption spectra of the desorbed dye solutions have been recorded using AnalytikJena Specord 205 spectrophotometer.

2.5.8 Photo-electrochemical characterization

The standard characterization technique of solar cells includes the determination of the current-voltage characteristics under light irradiance of a particular intensity. Current-voltage characteristics were measured using Source Meter interfaced with computer under illumination of simulated sunlight (solar simulator) as described below.

2.5.8.1 Solar simulator

A solar simulator provides illumination approximating natural sunlight. The purpose of the solar simulator is to provide indoor test facility for solar cells, sun screen, plastics, and other materials and devices, in laboratory. Figure 2.22 shows the optics of the solar simulator. Typically, high power solar simulators use an ellipsoidal reflector to capture light from an arc lamp source inside the reflector, an arrangement that results in a light pattern with a bright outer region and a dark centre. The xenon arc lamp at the heart of the simulator emits a 5800K blackbody-like spectrum. The system design features optical beam homogenization, filtering and collimation. The

result is a continuous output with a solar-like spectrum in a uniform collimated beam. Beam collimation simulates the direct terrestrial beam and allows characterization of radiation-induced phenomena [109].

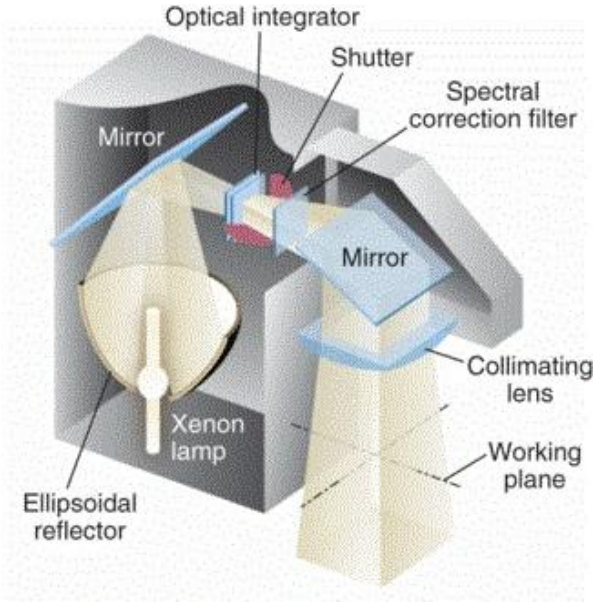

Figure 2.22 Optics of a solar simulator [109]

2.5.8.2 Source Meter

A Source Meter provides four-quadrant operation. In the first and third quadrants it operates as a source, delivering power to a load. In the second and fourth quadrants it operates as a sink, dissipating power internally. Voltage, current, and resistance can be measured during source or sink operation.

2.5.8.3 Current-Voltage characteristics

One of the key measurements needed to test solar cells is the determination of their I-V characteristics. By measuring the I-V curves, physical performances of solar cells such as open circuit voltage (V_{OC}), short circuit current (I_{SC}), photo-electric conversion efficiency (η) and fill factor (FF) can be determined which is important for reliable work in research and quality inspection. The current-voltage characteristics of a solar cell under illumination are shown in figure 2.23. The curve passes through the fourth quadrant and hence the device can deliver power. Generally, the I-V

characteristics are represented by rotating the current axis by 180° around the voltage axis.

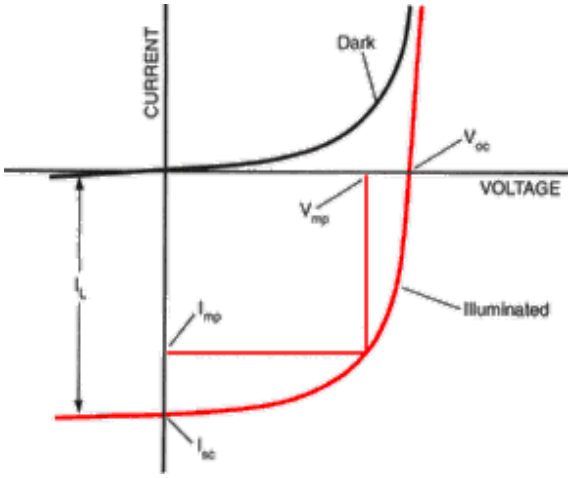

Figure 2.23 The current-voltage characteristics of a solar cell under illumination

2.5.8.4 Definitions & measuring conditions

2.5.8.4.1 Short-circuit current (I_{SC})

The short-circuit current is the current through the solar cell when the voltage across the solar cell is zero (i.e., when the solar cell is short circuited). The short-circuit current is due to the generation and collection of light-generated carriers. For an ideal solar cell at most moderate resistive loss mechanisms, the short-circuit current and the light-generated current are identical. Therefore, the short-circuit current is the largest current which may be drawn from the solar cell.

2.5.8.4.2 Short-circuit current density (J_{SC})

Short-circuit current density (J_{SC}) is short-circuit current per active area. To remove the dependence of the solar cell area, the short-circuit current density is listed rather than the short-circuit current.

2.5.8.4.3 Open-circuit voltage (V_{OC})

The open-circuit voltage (V_{OC}) is the maximum voltage available from a solar cell, and this occurs at zero current. In DSSC, Voc is defined by the difference between Fermi level of semiconductor and redox potential of electrolyte, under light illumination.

2.5.8.4.4 Maximum power (P_{max})

A DSSC operates over a wide range of voltages (V) and currents (I). As the resistive load on an illuminated solar cell is increased continuously from zero (short circuit condition) to the highest value (open circuit condition), the power delivered to the load first increases, reaches a maximum and then decreases to zero. The maximum power point (P_{max}) is achieved for a load for which the product of current and voltage is maximized.

2.5.8.4.5 Fill-factor (FF)

J_{SC} and V_{OC} are the maximum current and voltage respectively from a solar cell. However, at both of these operating points, the power from the solar cell is zero. The fill factor (FF), is a parameter which, in conjunction with Voc and Isc, determines the maximum power from a solar cell. The FF is defined as the ratio of the maximum power from the solar cell to the product of Voc and Isc. Graphically, the FF is a measure of the "squareness" of the solar cell and is also the area of the largest rectangle which will fit in the IV curve.

$$FF = \frac{P_{max}}{J_{sc} \times V_{oc}}$$

2.5.8.4.6 Efficiency (η)

The efficiency is the most commonly used parameter to compare the performance of one solar cell to another. Efficiency is defined as the ratio of energy output from the solar cell to input energy from the sun. The power conversion efficiency (η) of DSSC

is determined by the photocurrent density measured at short-circuit, Voc, FF of the cell, and the intensity of the incident light (P_i) as shown in follow equation.

$$\eta = \frac{I_{SC} \times V_{OC} \times FF}{P_i}$$

2.5.8.4.7 Air mass 1.5

Air mass refers to the relative path length of the direct solar beam through the atmosphere. The air mass (AM) coefficient defines the direct optical path length through the Earth's atmosphere, which is expressed as a ratio relative to the path length vertically upwards, i.e. at the zenith. When the sun is directly overhead (at zenith), the path length is 1.0 (AM 1.0). When the angle of the sun from zenith increases, the air mass increases so that at 48.2° from the vertical the air mass is 1.5 and at 60.1° the air mass is 2.0 (figure 2.24). The air mass coefficient is commonly used to characterize the performance of solar cells under standardized conditions. "AM1.5" is almost universal when characterizing terrestrial power-generating panels. The conditions for the AM 1.5 spectra were chosen by ASTM "because they are representative of average conditions in the 48 contiguous states of the United States" [109].

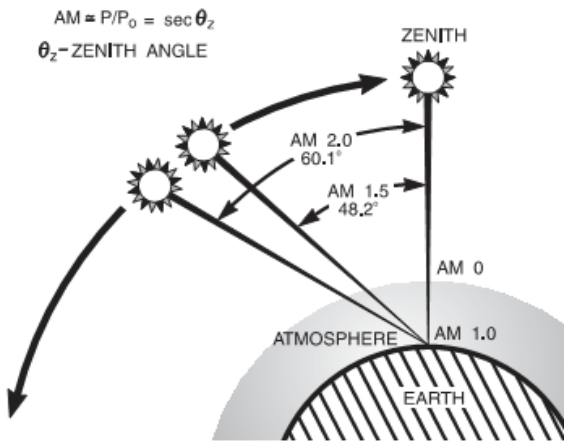

Figure 2.24 The path length in units of Air Mass, changes with the zenith angle [109]

In operation, these instruments can act as a voltage source, a current source, a voltage meter, a current meter, and an ohmmeter. The I-V testing has been done by setting the voltage and measuring the current while keeping the light source constant. The efficiency of solar cell is determined current density-voltage (J-V) characteristics obtained under illumination. A lamp with a spectrum very similar to the solar AM1.5 spectrum is used for illumination and calibrated to an intensity of 1000 Wm^{-2} for measurements at 1 sun intensity. A Newport solar simulator model 96000 was used for the illumination of DSSC. A voltage is applied between the working and counter electrode of the solar cell and the current output is measured. The voltage range should include the voltage at which the current is zero (the open-circuit voltage) and 0 V, at which the short-circuit current density is measured. The resulting current-voltage curve is usually referred to as a J-V curve. The collected information is sufficient to plot the J-V characteristics and to extract the different parameters discussed above.

In the present study, J-V characteristics were measured using Keithley 2400 Source Meter interfaced with computer under simulated sunlight from solar simulator (Model 96000, Newport).

Chapter-3

Oxide-layer coated ZnO nanoparticles and their applications in dye sensitized solar cells

Chapter-3

This chapter deals with the various studies conducted for Eu_2O_3 and $CaCO_3$ coated ZnO nanoparticles based dye sensitized solar cells. The structural, morphological and optical properties of the synthesized nanoparticles and the analyses of the obtained current density-voltage (J-V) characteristics of the fabricated DSSCs are presented.

3.1 Eu_2O_3 coated ZnO nanoparticles based dye sensitized solar cells

3.1.1 Synthesis of Eu_2O_3 coated ZnO nanoparticles

Synthesis of Eu_2O_3/ZnO nanoparticles was done by a two-step process. First, ZnO nanoparticles were synthesized by the method described in section 2.3.1.1 (sample named as ZE0). For Eu_2O_3 coating, firstly, the synthesized ZnO nanoparticles were ultrasonically dispersed in ethanol. In another beaker, 0.01M $EuCl_3$ in ethanol was reduced with $NaBH_4$ and magnetically stirred for 15 minute. Now, this solution was added drop-wise to the dispersed ZnO nanoparticles. In this technique, the primarily synthesized ZnO nanoparticles act as nucleation sites for the Eu_2O_3 coating. To allow uniform coating on the particles and prevent the coating material from being produced separately from the particles, the coating solution was added drop-wise. Further, the above mixture was transferred to Teflon container and autoclaved for 14 hour at 150°C. The particles were washed and filtered. The particles thus obtained were calcined at 500°C for 30 minute, to obtain crystalline nanoparticles (this sample is named as ZE1). Similarly, two more samples were synthesized by adjusting the concentration of $EuCl_3$ to 0.02M and 0.03M (ZE2 and ZE3).

3.1.2 Structural and phase analyses

Figure 3.1 shows the XRD patterns of ZE0, ZE1, ZE2 and ZE3 samples. All the peaks in the XRD pattern of ZE0 are indexed to hexagonal structure with wurtzite phase, (JCPDS card No: 80-0075) with strong reflections from (101), (100) and (002) planes. The XRD pattern of ZE1 shows no peak related to Eu_2O_3 which shows Eu_2O_3 formed a very thin layer, which was too thin to be detected by XRD. In the XRD patterns of ZE2 and ZE3, the diffraction peak from cubic phase Eu_2O_3 is indexed to (222) (marked with * in figure 3.1), as confirmed by the JCPDS card No: 74-1988, which demonstrates the existence of Eu_2O_3 on the surface of ZnO nanoparticles.

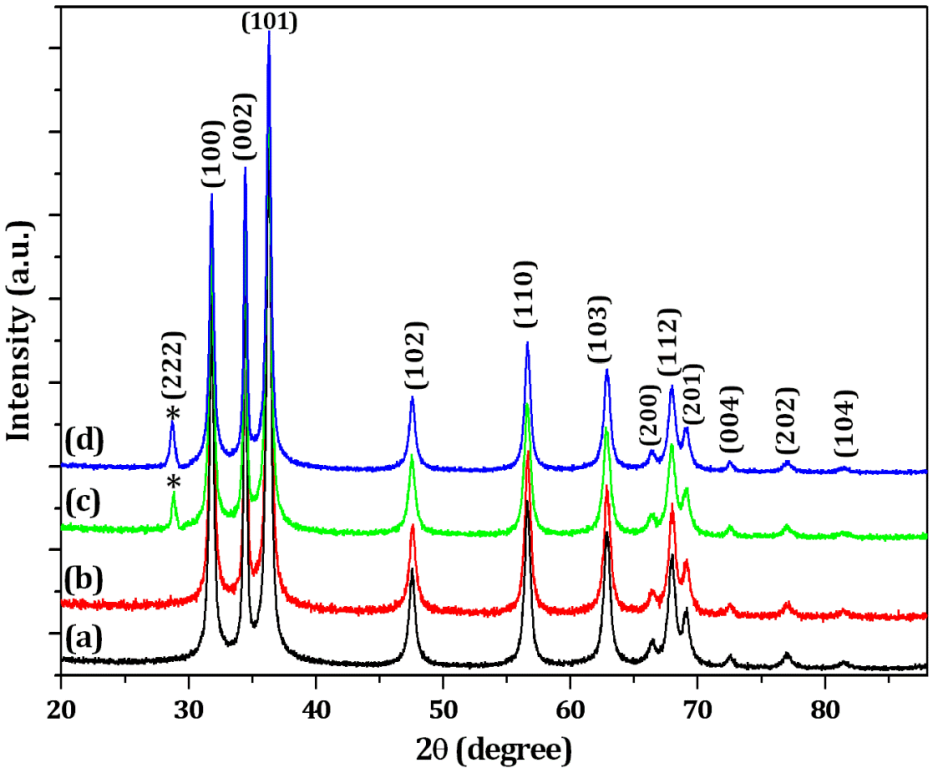

Figure 3.1 X-ray diffractogram of (a) ZE0 (b) ZE1 (c) ZE2 and (d) ZE3 samples

3.1.3 Compositional analysis

Further to corroborate the XRD results, EDAX analysis has been carried out and shown in figure 3.2. For the sample, ZE0, the EDAX spectrum (figure 3.2(a)) shows distinct peaks of Zn and O, with atomic percentage 51.33 and 48.67, respectively, concluding stoichiometric formation of ZnO nanoparticles. The EDAX spectrum of the samples ZE1, ZE2 and ZE3 (figure 3.2(b), 3.2(c) and 3.2(d)) show the presence of Zn, O and Eu elements, indicating the presence of Eu_2O_3 coating on the ZnO nanoparticles, as observed in XRD patterns as well (figure 3.1). A systematic decrease in Zn content and a relative increase in the atomic percentage of Eu have been observed with the increasing concentration of Eu_2O_3 in the samples.

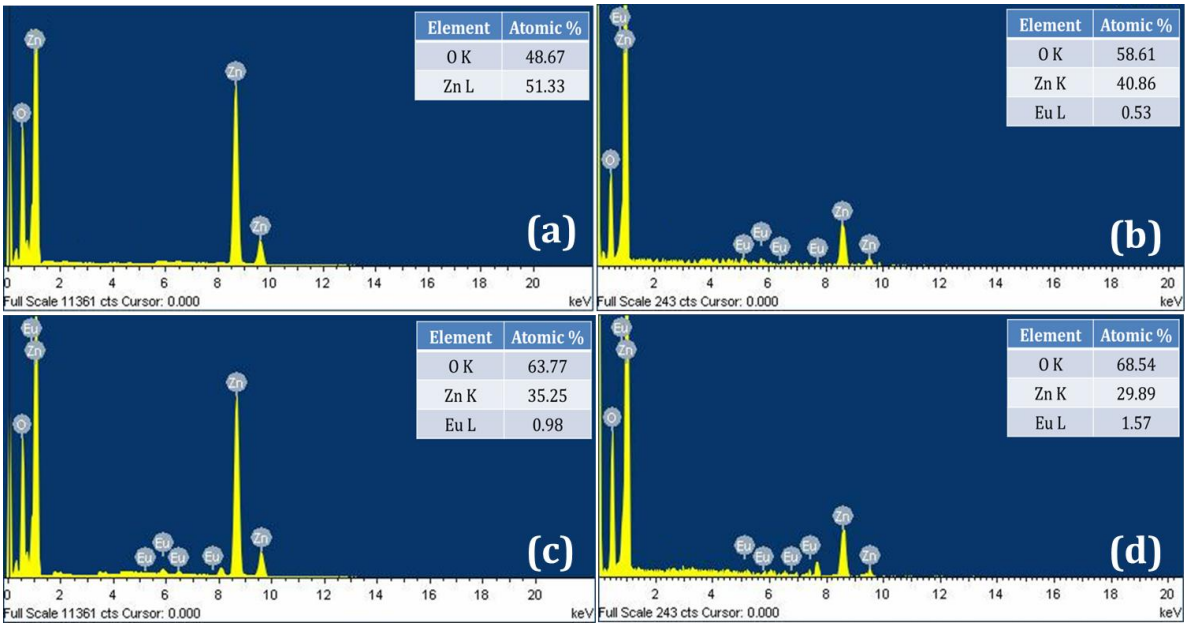

Figure 3.2 EDAX spectrum of (a) ZE0 (b) ZE1 (c) ZE2 and (d) ZE3 samples

3.1.4 Morphological study

The presence of Eu_2O_3 on the surface of the ZnO nanoparticles has been established from TEM of ZE2 sample. TEM micrographs of ZE0 (figure 3.3(a)) and ZE2 (figure

3.3(b)) samples reveal their spherical nature with average particle size 9.4 nm and 10.1 nm, respectively. Figure 3.3(b) confirms the coating (shown by arrows in the inset) of Eu_2O_3 on ZnO nanoparticles.

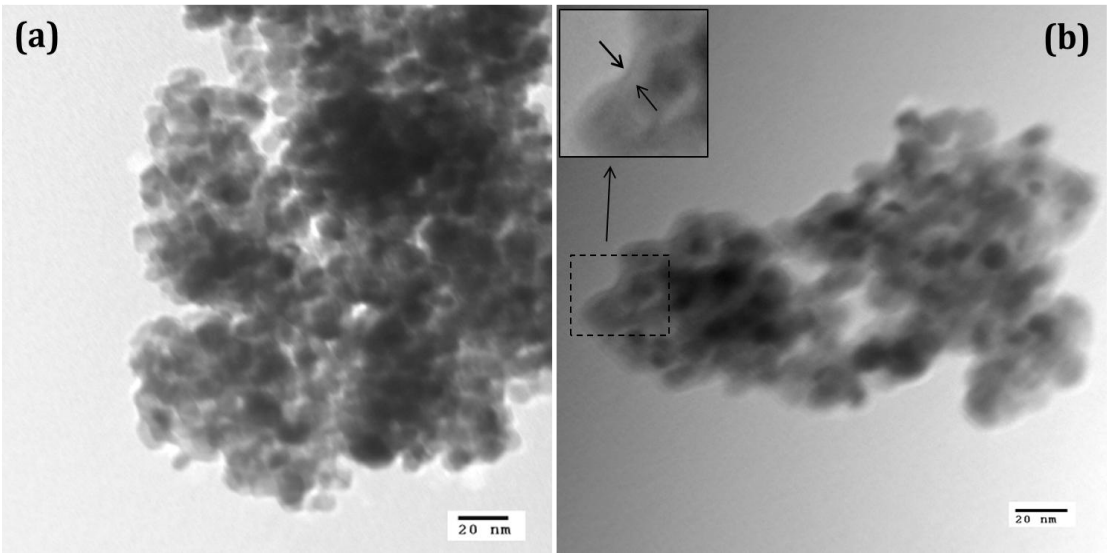

Figure 3.3 TEM micrographs of (a) ZE0 and (b) ZE2 samples

3.1.5 FTIR spectroscopy

The FTIR spectra (figure 3.4) reveals a series of absorption peaks, corresponding to the vibration modes of hydroxyl, carboxylate, and alkane groups in the synthesized samples. To be more specific, a broadband peaked at 3424 cm^{-1} has been assigned to the O-H stretching mode of hydroxyl group, which results from the hygroscopic nature of ZnO. Small peaks at 2853 and 2927 cm^{-1} are due to C-H stretching vibration of alkane groups. The peaks at 560 and 901 cm^{-1} correspond respectively to the bending vibration and stretching vibrations of Zn-O bond [110]. The peak at 1680 cm^{-1} has been assigned to the first overtone of fundamental stretching mode of O-H [111]. The peak observed at 1386 cm^{-1} is due to the symmetrical stretching of the zinc carboxylate COO^- bond.

In case of Eu_2O_3/ZnO, the FTIR signatures of these bonds decrease which suggest that Eu_2O_3 exists on the surface of ZnO nanoparticles. In the FTIR spectra of ZE1, ZE2 and ZE3 samples, the band at 3424 cm^{-1} representative of free-OH shows decrease in intensity suggesting that the hydroxyl functional groups are occupied with Eu_2O_3 coating. Other bands of the spectra also show significant decrease in the peak intensity indicating an interaction between the Eu_2O_3 coating and ZnO nanoparticles.

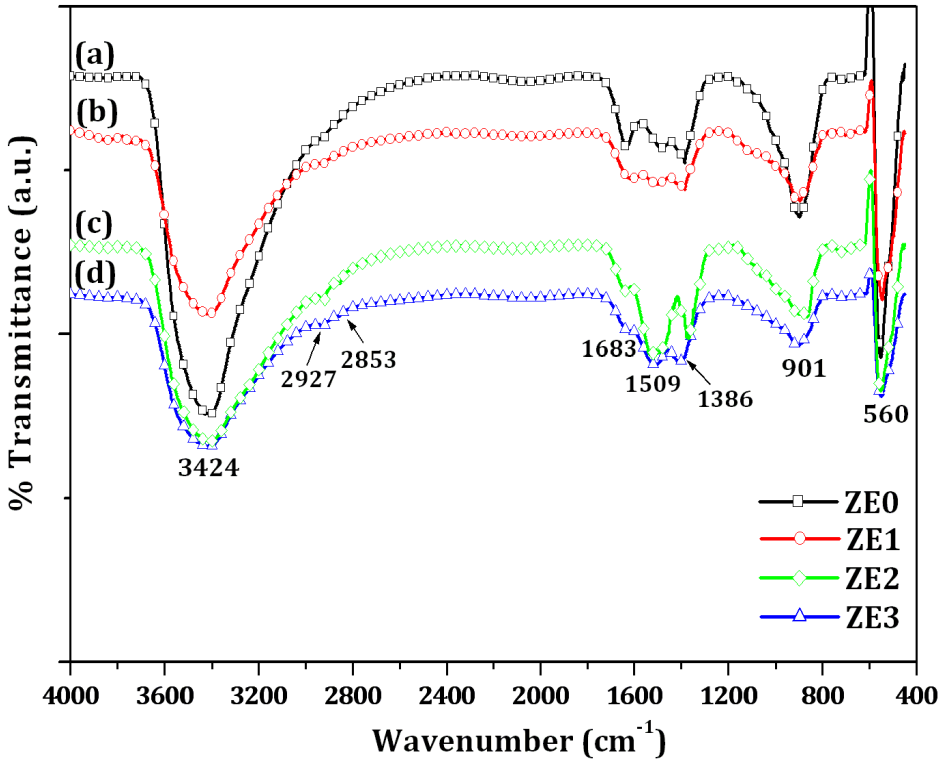

Figure 3.4 FTIR spectra of (a) ZE0 (b) ZE1 (c) ZE2 (d) ZE3 samples

3.1.6 Optical analyses

3.1.6.1 Photoluminescence studies

PL spectroscopy has been performed in order to study and understand the phenomenon of electron–hole recombination process occurring in the bare ZnO and Eu_2O_3/ZnO nanoparticles. Figure 3.5 shows the PL spectra of the synthesized

samples. In the PL spectrum of ZE0 sample, the peak at 409 nm has been assigned to zinc vacancy [112]. The blue emission around 428 nm has been ascribed to the excitons recombination between the electron localized at interstitial zinc and the holes in the valence band. The peaks at 486 nm and 529 nm are possibly due to the intrinsic defects such as oxygen vacancy [113]. The luminescence peak centered at 381 nm has been attributed to the near band-edge (3.37 eV) emission of ZnO [114]. In PL spectra of Eu_2O_3/ZnO nanoparticles, a violet band at 422 nm has been observed which may be attributed to the interstitial oxygen and/or transition between defects (interface traps) at grain boundaries and the valence band [115]. However, the PL intensity of ZnO decreased with Eu_2O_3 coating. The decrease in the intensity has been attributed to the fewer defects and low electron–hole (e^-/h^+) recombination process with the surface modification of the Eu_2O_3 layer located at the boundaries of ZnO nanoparticles. In ZnO there exist some intrinsic defects, such as oxygen vacancies. The defects at the surface may act as adsorption sites for O_2 and H_2O. These sites can trap free electrons and serve as non-radiative recombination centers. The coating of Eu_2O_3 on ZnO nanoparticles remarkably decreases the non-radiative recombination rate [115]. Thus the PL intensity of Eu_2O_3 coated ZnO nanoparticles is less that of bare ZnO nanoparticles. The intensity of ZE1 and ZE2 are almost same and least of all, which is most likely due to Eu_2O_3 playing the role of electrons captures, thereby depressing the recombination process.

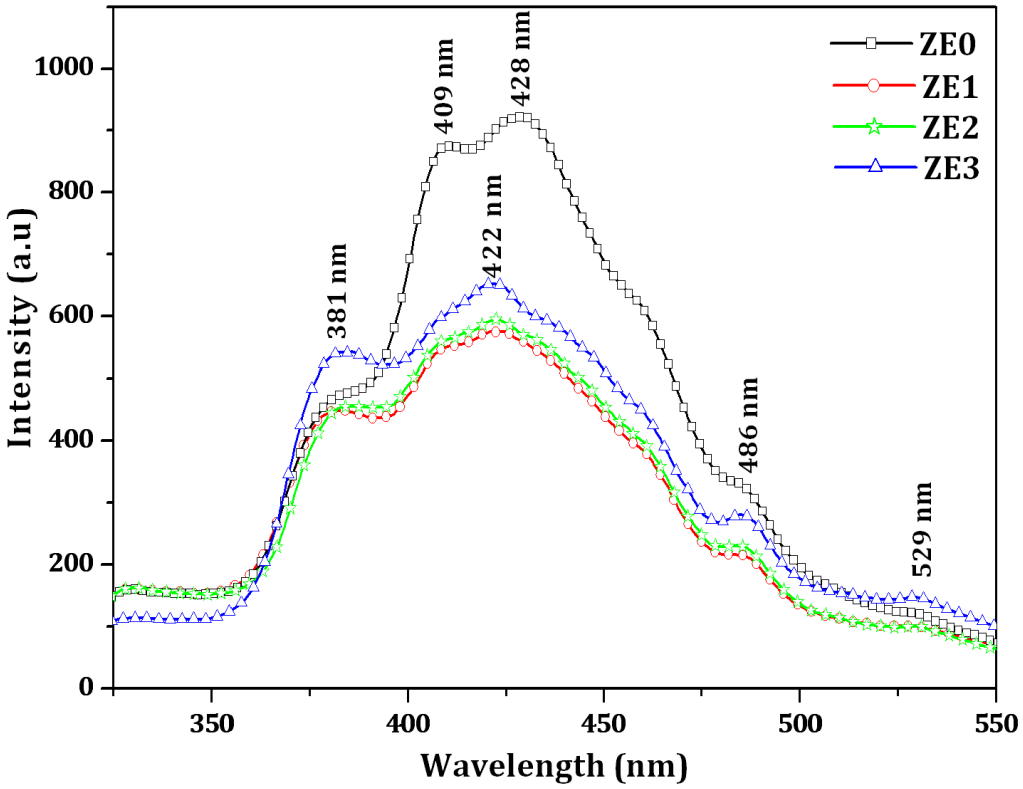

Figure 3.5 Photoluminescence spectrum of (a) ZE0 (b) ZE1 (c) ZE2 and (d) ZE3 samples

3.1.6.2 Dye desorption studies

The fabricated photoelectrodes were immersed in 0.3mM ethanolic solution of N719 dye (20mL) for 20 hour. To desorb the dye molecules from the electrodes, they were soaked in 0.1mM aqueous NaOH solution. Figure 3.6 shows the UV-visible absorption spectra of the desorbed dye obtained from the electrodes. The peaks at 370 nm and 500 nm correspond to the characteristic absorption of N719 dye. The degree of dye adsorption on the electrode is proportional to the intensity of the optical absorption of dye. From the absorption study, it has been found that the amount of dye adsorbed on the ZE1, ZE2 and ZE3 electrodes show enhanced dye adsorption as compared to the ZE0 electrode.

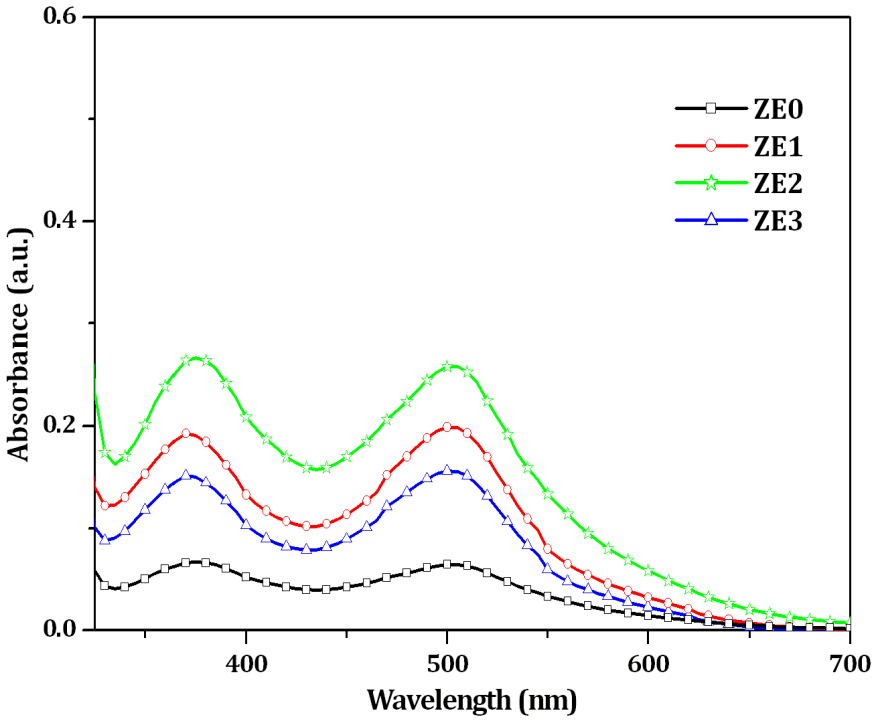

Figure 3.6 UV–Vis absorption spectra of the N719 dye desorbed from (a) ZE0 (b) ZE1 (c) ZE2 and (d) ZE3 electrodes

The better adsorption of the dye molecules on Eu_2O_3/ZnO nanoparticles enhances the DSSC performance, as this increases the concentration of photogenerated electrons by visible light [117]. The photocurrent of DSSC is influenced by the initial number of photogenerated electron-hole pairs, which depend on the film structure of the electrodes. The modification in film structure leads to the change in the light-harvesting capacity of photoelectrodes [118]. Figure 3.6 illustrates that the electrode fabricated from the sample, ZE2 ensures maximum photon capturing in the visible region and furthermore indicates strong light-harvesting capacity. For the generation of high photocurrent density, the amount of dye adsorbed on nanocrystalline film should be high. The decrease in the adsorbed dye from ZE3 electrode is due to the decrease in the surface area of the working electrode due to high concentration of coating precursor.

3.1.7 Photocurrent density-Voltage (J-V) characteristics

Figure 3.7 shows the J-V curves obtained from DSSC fabricated using ZE0, ZE1, ZE2 and ZE3 nanoparticles, with an active area of 1 x 1 cm^2. Various parameters calculated from J-V curve are summarized in table 3.1. From the table, it can be seen that there is an increase in the short circuit current density (J_{SC}), open circuit voltage (V_{OC}), fill factor (FF) and efficiency (η) of DSSC fabricated from Eu_2O_3/ZnO nanoparticles compared to ZnO nanoparticles based DSSC. The coating Eu_2O_3 on ZnO acts as an energy barrier, which minimizes the e^-/h^+ recombination and retards the back electron transfer to the electrolyte, resulting in increase in the value of open circuit voltage from 602 mV to 704 mV in case of ZE0 DSSC and ZE2 DSSC, respectively. The increased Voc for Eu_2O_3/ZnO DSSC indicates the introduction of coating on ZnO nanoparticles has decreased the recombination rate of the electron to the electrolyte by changing the conduction band edge of ZnO [119]. The interfacial charge recombination between the electrons in the ZnO conduction band to the oxidized electrolyte species (I_3^-) and oxidized dye molecules at the surface of the nanostructured working electrode has reduced.

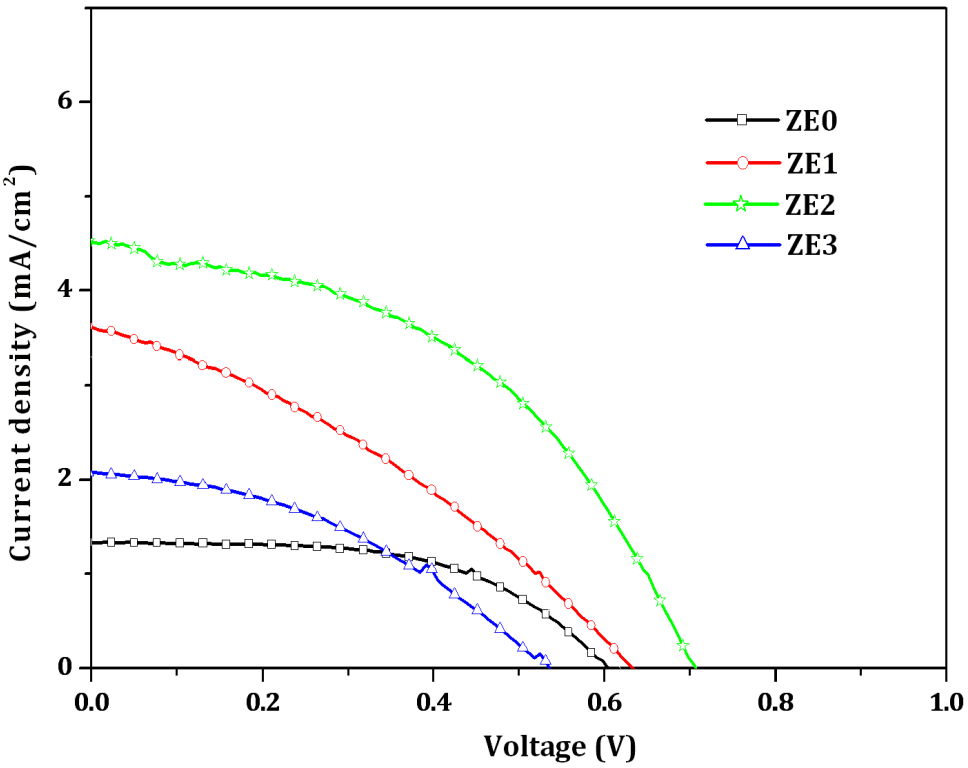

Figure 3.7 J-V characteristics of DSSC fabricated using ZE0, ZE1, ZE2 and ZE3 samples

Table 3.1 The different parameters of DSSC (J_{SC}, V_{OC}, FF and η), as calculated from the J-V characteristics

Sample	J_{SC} (mA/cm^2)	V_{OC} (mV)	FF	η (%)
ZE0	1.34	602	0.56	0.44
ZE1	3.61	630	0.33	0.77
ZE2	4.51	704	0.45	1.45
ZE3	2.06	536	0.38	0.43

An increase in the short circuit current density from 1.34 mA/cm^2 for ZE0 DSSC to 4.51 mA/cm^2 for ZE2 DSSC has been observed. The increase in short circuit current

density can be explained by the fact that the amount of dye molecules adsorbed on Eu_2O_3/ZnO electrode is higher than the bare ZnO electrode [118]. The enhancement of V_{OC}, J_{SC} and FF in case of ZE2 DSSC as compared to ZE0 DSSC leads to an increase in the overall efficiency from 0.44% to 1.45%. However, ZE3 DSSC shows a decline in efficiency, from 1.45% down to 0.43% for DSSC fabricated from ZE2 sample. This is due to the fact that thicker coating more effectively reduces the charge recombination but it also reduces the rate of electron injection into ZnO [45]. With the increased distance for electrons to tunnel through the Eu_2O_3 coating to ZnO, J_{SC} has decreased due to a reduced interfacial charge transfer rate.

The studies on all the next samples ($CaCO_3$/ZnO, Eu_2O_3/TiO_2 and $CaCO_3$/TiO_2), J-V characteristics of different coating concentrations were first obtained in order to determine the sample with maximum efficiency. The rest of the characterizations were performed for that sample only.

3.2 $CaCO_3$ coated ZnO nanoparticles based dye sensitized solar cells

3.2.1 Synthesis of $CaCO_3$/ZnO nanoparticles

For the synthesis of $CaCO_3$/ZnO nanoparticles, 0.01M Na_2CO_3 and $CaCl_2$ were dissolved in water. This solution was then added drop-wise to the ethanolic dispersion of ZnO nanoparticles (synthesis procedure described in section 2.3.1.1) and stirred for about 2 hour. The solution was transferred to autoclave and put in oven at 140˚C for 14 hour. The $CaCO_3$/ZnO nanoparticles formed were filtered and washed with ethanol and water. The particles thus obtained were calcined at 300°C for 1 hour, to obtain crystalline nanoparticles.

3.2.2 Structural and phase analyses

Figure 3.8 shows the XRD patterns of ZnO and $CaCO_3$/ZnO nanoparticles. It is clear that in case of ZnO (figure 3.8(a)), the diffraction peaks positioned at 2θ values of 31.7˚, 34.4˚, 36.2˚, 47.5˚, 56.6˚, 62.8˚, 66.4˚, 67.9˚, 69.0˚, 72.8˚, and 77.0˚ and, respectively, indexed as *(100), (002), (101), (102), (110), (103), (200), (112), (201), (004)* and *(202)* well match with wurtzite structure having hexagonal phase (JCPDS No. 80-0075). From the figure 3.8(b), it has been found that in case of $CaCO_3$/ZnO nanoparticles there are several small diffraction peaks centred between the strong peaks of ZnO of $CaCO_3$. The diffraction peaks positioned at 2θ values of 29.3˚, 39.4˚, 43.9˚, and 60.7˚ indexed as *(104), (113), (202),* and *(214)* correspond to rhomb-centred structure having hexagonal phase $CaCO_3$ (JCPDS No. 85-1108). XRD peaks corresponding to ZnO and $CaCO_3$ are marked as 'Z' and 'C', respectively (figure 3.8 (b)).

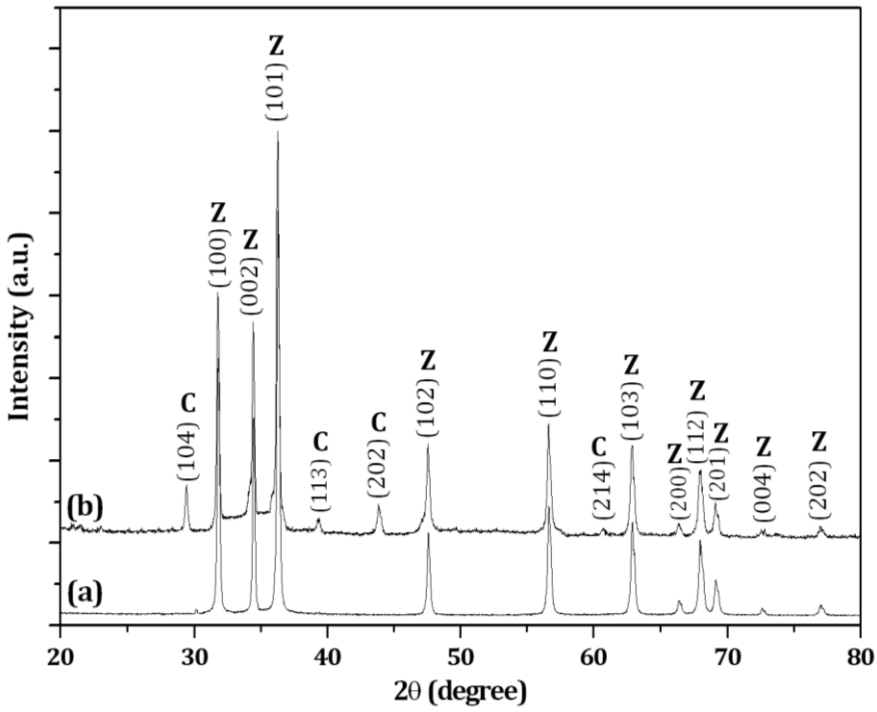

Figure 3.8 XRD patterns of (a) ZnO nanoparticles and (b) $CaCO_3$/ZnO nanoparticles

The crystallite size as calculated using Debye-Scherrer formula has been found to be 20.0 nm and 19.3 nm, for ZnO and $CaCO_3$/ZnO nanoparticles, respectively. Crystallite size decreased on $CaCO_3$ coating, as the coating constrains the growth of grains [120].

3.2.3 Compositional analysis

EDAX spectrum of $CaCO_3$/ZnO nanoparticle based electrode (figure 3.9) reveals that the atomic % of the elements has been found to be Ca (1.02%), C (2.92%), Zn (24.99%) and O (71.07%). This clearly reveals that $CaCO_3$/ZnO nanoparticles, are in stoichiometric ratio, and confirms the presence of $CaCO_3$ coating on the surface of ZnO nanoparticles as observed in TEM images (figure 3.10(b)).

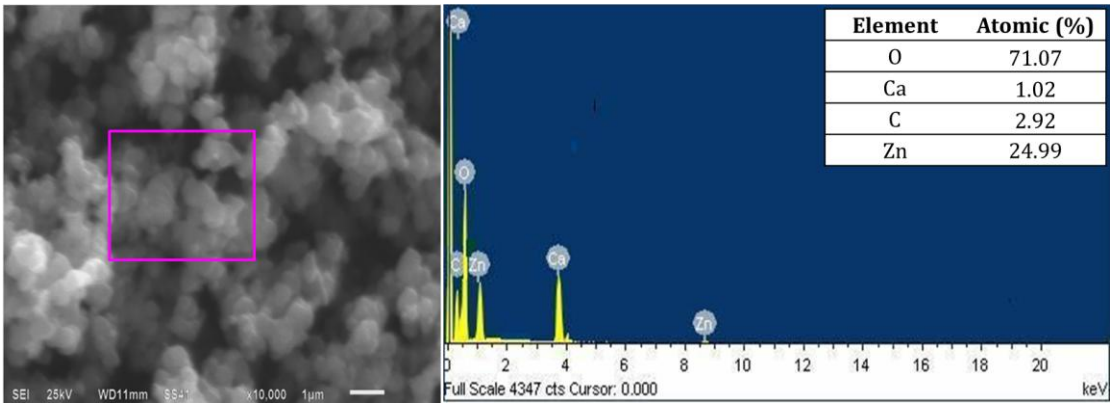

Figure 3.9 EDAX spectrum of $CaCO_3$/ZnO nanoparticles based electrode, the inset shows the atomic and weight % of elements detected

3.2.4 Morphological study

Figure 3.10(a) and 3.10(b) show TEM image of ZnO and $CaCO_3$/ZnO nanoparticles, respectively, which reveals their spherical nature. The average particle size of ZnO nanoparticles and $CaCO_3$/ZnO nanoparticles as calculated from histograms (figure 3.10(inset)) were found to be, respectively, 6.2 and 6.7 nm. The HRTEM image

(figure 3.10(c)) confirms the presence of $CaCO_3$ coating on ZnO nanoparticles' surface.

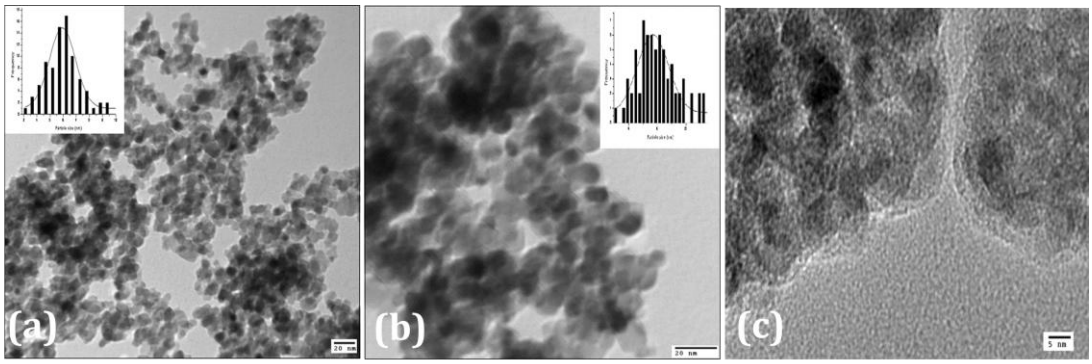

Figure 3.10 TEM images of (a) ZnO nanoparticles and (b) $CaCO_3$/ZnO nanoparticles (c) HRTEM image of $CaCO_3$/ZnO nanoparticles

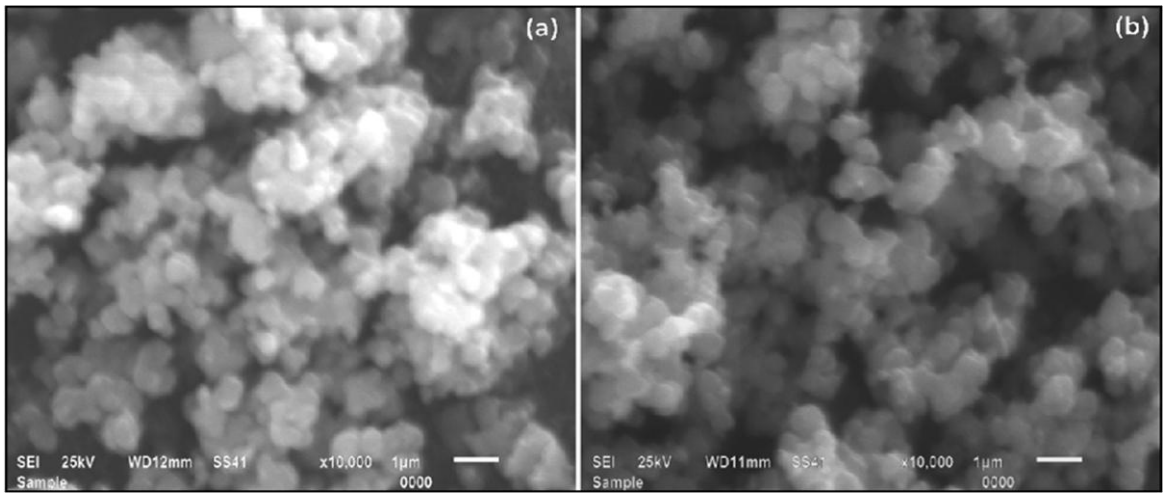

Figure 3.11 SEM images of (a) ZnO, (b) $CaCO_3$/ZnO nanoparticles based electrode

The morphological study of fabricated electrodes has been carried out using SEM (figure 3.11). Figure 3.11(a) clearly reveals that ZnO nanoparticles possess spherical symmetry having less porosity. The $CaCO_3$/ZnO nanoparticles (figure 3.11(b)) are found to be nearly spherical and possessing higher porosity as compared to the electrode fabricated using ZnO nanoparticles (figure 3.11(a)). Higher surface area and

porosity of the electrode fabricated from $CaCO_3$/ZnO nanoparticles leads to higher dye adsorption (figure 3.14).

3.2.5 FTIR spectroscopy

In the FTIR spectrum (figure 3.12) of bare ZnO nanoparticles, a broadband peaked at 3422cm^{-1} has been assigned to the O-H stretching mode of hydroxyl group, which results from the hygroscopic nature of ZnO. The peaks at 548cm^{-1} and 890cm^{-1} correspond, respectively, to the bending vibration and stretching vibrations of Zn-O bond [110]. The FTIR spectrum of $CaCO_3$/ZnO nanoparticles confirms the existence of C-O in CO_3^{2-} represented by the peaks due to antisymmetric stretching, and out of plane bending [68]. The peak at 1636cm^{-1} has been assigned to O-H bending vibrations.

The peaks at 871cm^{-1} and 1002cm^{-1} correspond to ν2 vibration mode of CO_3^{2-}. The peak observed at 1444cm^{-1} has been assigned to ν3 vibration mode of CO_3^{2-}. Peak at 785cm^{-1} is due to the ν4 vibration mode of CO_3^{2-}. The absorption peaks 1140 cm^{-1} is assigned to the stretching vibration of C-O bond [121]. The peaks at 511cm^{-1} and 598cm^{-1} correspond to Zn-O bond [122]. The broadband at 3521cm^{-1} and the peak at 1624cm^{-1} have been assigned to O-H stretching modes and O-H bending vibrations of hydroxyl group.

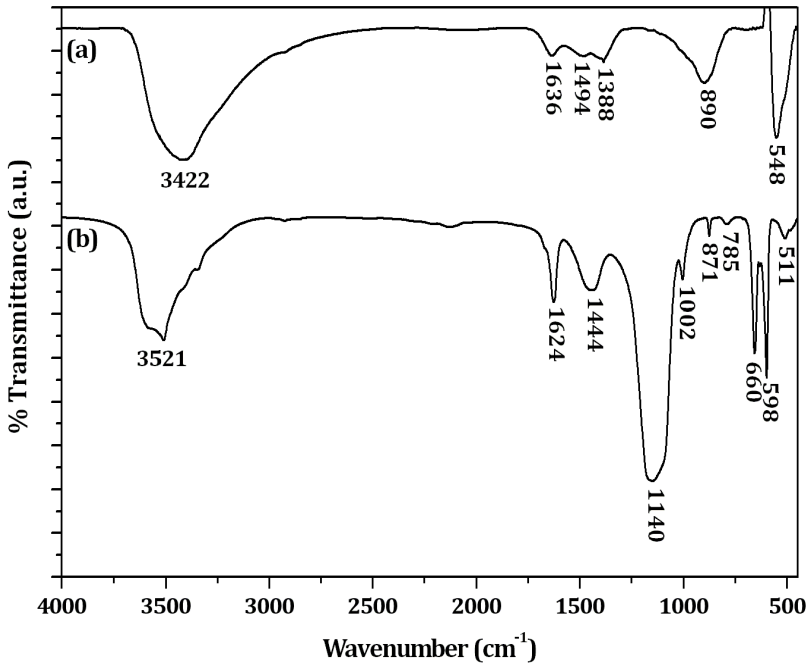

Figure 3.12 FTIR spectra of (a) ZnO and (b) $CaCO_3$/ZnO nanoparticles

In the FTIR spectra of $CaCO_3$/ZnO nanoparticles, the band at 3422 cm^{-1} representative of free-OH shifted to higher wavenumber (3521 cm^{-1}). This has been attributed to weakening of the hydrogen bonding interaction, suggesting that the hydroxyl groups are occupied with $CaCO_3$ coating [123]. In general, the electron injection efficiency is reduced by hydroxyl groups and physisorbed water molecules present on the surface of ZnO nanoparticles. Consequently, the increase in the electron injection efficiency from ZnO to FTO is expected, which enhances the overall conversion efficiency of DSSC.

3.2.6 Optical analyses

3.2.6.1 Photoluminescence studies

Photoluminescence spectrum of bare ZnO and $CaCO_3$/ZnO nanoparticles has been shown in figure 3.13. An appreciable change in the PL emission spectra of

$CaCO_3$/ZnO nanoparticles has been observed due to surface modification of ZnO with $CaCO_3$. In the PL spectrum, peak at 402 nm has been attributed to the exciton transitions. The violet emission at 423 nm is due to the recombination of carriers between the electrons at interstitial zinc and the holes in the valence band [115]. The peaks at 486 nm and 529 nm are possibly due to the intrinsic defects such as oxygen vacancy [113]. The blue emission at 445 nm can be attributed to the surface defects of ZnO nanostructure [124]. The emission at 460 nm has been referred to as deep-level emission and attributed to recombination of electrons trapped in oxygen vacancies and zinc interstitials, with photogenerated holes [125].

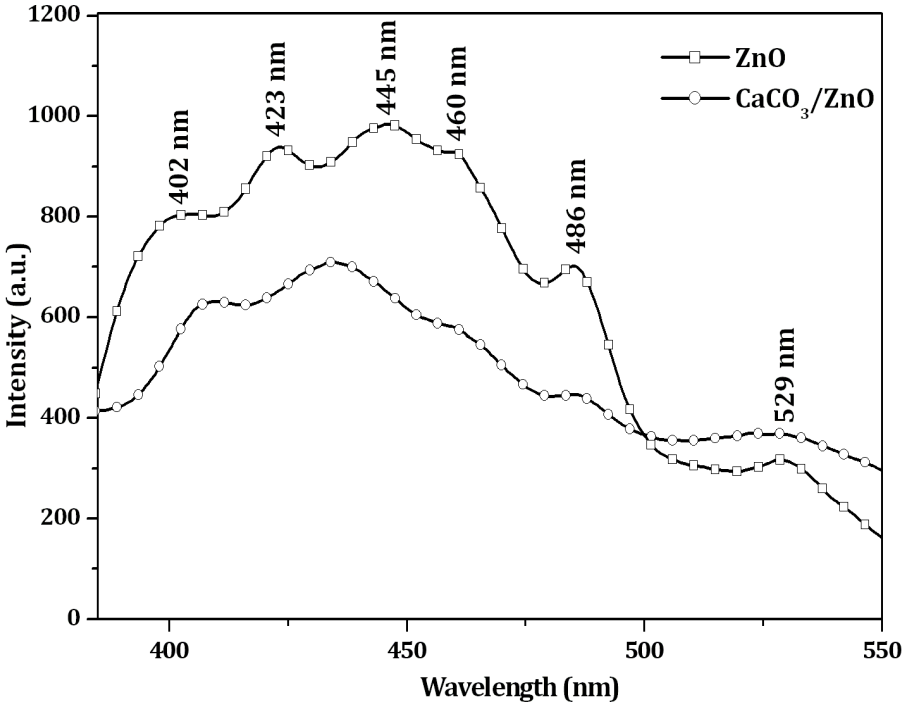

Figure 3.13 Photoluminescence spectrum of ZnO and $CaCO_3$/ZnO nanoparticles

However, the PL intensity of ZnO decreased with coating of $CaCO_3$. The PL emission mainly results from the recombination of excited electrons and holes, and thus the lower PL intensity indicates the decrease in recombination rate. The decrease in the intensity can be attributed to the fewer defects and low electron–hole (e^-/h^+)

recombination process with the surface coating of $CaCO_3$ on ZnO nanoparticles. In ZnO there exist some intrinsic defects, such as oxygen vacancies which act as adsorption sites for O_2 and H_2O. These sites can trap free electrons and serve as non-radiative recombination centers. Also, the surface O-H groups are reduced on coating, thus resulting in reduction of the unwanted non-radiative decay pathways thereby increasing the electron injection efficiency.

3.2.6.2 Dye desorption studies

In order to compare the amount of dye adsorbed on the electrode fabricated using ZnO and $CaCO_3$/ZnO nanoparticles, UV-visible absorption study has been performed of the N719 dye desorbed from ZnO electrode and $CaCO_3$/ZnO electrode. For this, ZnO and $CaCO_3$/ZnO photoelectrodes were immersed in 0.3mM ethanolic solution of N719 dye (20mL) for 20 hour. The dyed film was dipped in 0.1mM aqueous NaOH solution for 30 minute so that dye gets desorbed from the surface of the film. Figure 3.14 shows the UV-visible absorption spectra of the desorbed dye obtained from both the electrodes. The absorbance of the desorbed dye from $CaCO_3$/ZnO electrode has been found to be more than 200% higher than that of bare ZnO electrode. The better adsorption of the dye molecules on $CaCO_3$/ZnO electrode is expected to enhance the DSSC performance, as the extent of dye adsorbed decides the concentration of photogenerated electrons by visible light.

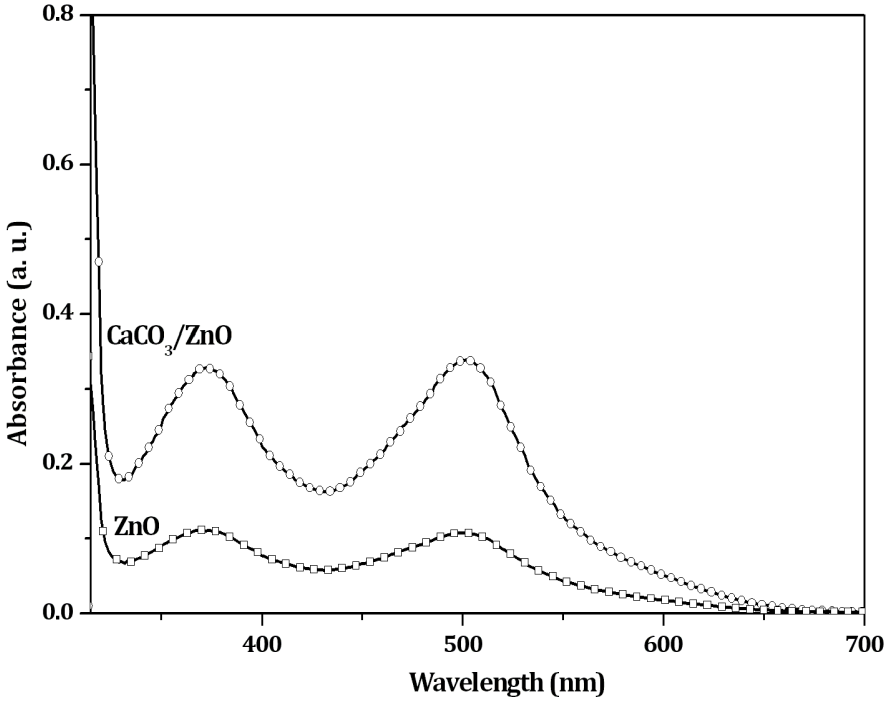

Figure 3.14 UV-Vis absorption spectra of dye desorbed from ZnO and $CaCO_3$/ZnO nanoparticles based electrodes

3.2.7 Current density-voltage (J-V) characteristics of DSSC

The performance of fabricated DSSC and its efficiency has been measured from the J-V curves (figure 3.15). The short circuit current density (J_{SC}) and open circuit voltage (V_{OC}) for $CaCO_3$/ZnO nanoparticle based DSSC has been found to be higher than that of ZnO nanoparticle based DSSC (Table 3.2).

An increase of over 100% in efficiency has been observed on using $CaCO_3$ coated ZnO based DSSC as compared ZnO based DSSC. This increase in efficiency can be attributed to the increase in porosity of the nanoparticles due to coating of $CaCO_3$ on ZnO nanoparticles as illustrated in SEM analysis. The dye adsorption studies reveal that $CaCO_3$/ZnO based electrode adsorbs more dye molecules as compared to bare ZnO based electrode. The increase in dye adsorption by $CaCO_3$/ZnO electrode leads to an increase in J_{SC} as compared to ZnO based electrode. The basic $CaCO_3$ coating on

ZnO facilitates the better adsorption of the dye due to intermolecular electrostatic attraction through carboxylic acid group of the N719 dye. The coating of $CaCO_3$ results in increase in absorbance due to its higher band gap energy (6.0 eV) and high isoelectric point (8.2) [68].

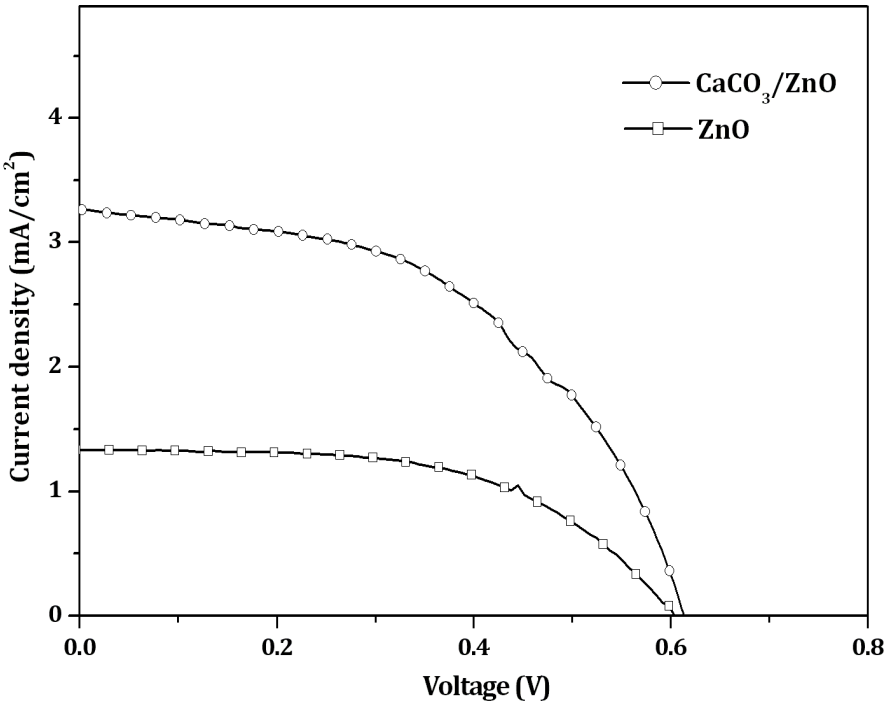

Figure 3.15 Photocurrent density-voltage (J-V) curve of DSSC employing ZnO nanoparticles and $CaCO_3$/ZnO nanoparticles

Table 3.2 The different parameters of DSSC (J_{SC}, V_{OC}, FF and η), as calculated from the J-V characteristics

Material	J_{SC} (mA/cm^2)	V_{OC} (mV)	FF	Efficiency (%)
ZnO	1.33	604	0.55	0.45
$CaCO_3$/ZnO	3.26	613	0.50	1.00

Also, as discussed in FTIR analysis (section 3.4) the decrease in OH bonds due to coating leads to faster electron injection efficiency from ZnO to FTO. The increase in V_{OC} is attributed to the fact that $CaCO_3$ coating forms an energy barrier which decreases the recombination rate of the photo-injected electrons with the oxidized dye and ions in the electrolyte. Similar results have been observed using $CaCO_3$ coated TiO_2 nanoparticles [68]. The performance of the DSSC has been significantly improved by the use of $CaCO_3$ coating, which precisely controls back electron transfer by reducing the electron hole recombination.

Chapter-4

Oxide-layer coated TiO_2 nanoparticles and their applications in dye sensitized solar cells

Chapter-4

This chapter deals with the various studies conducted for Eu_2O_3 and $CaCO_3$ coated TiO_2 nanoparticles based dye sensitized solar cells. The structural, morphological and optical properties of the synthesized nanoparticles and the analyses of the obtained current density-voltage (J-V) characteristics of the fabricated DSSCs are presented.

4.1 Eu_2O_3 coated TiO_2 nanoparticles based dye sensitized solar cells

4.1.1 Synthesis of Eu_2O_3 coated TiO_2 nanoparticles

Synthesis of Eu_2O_3 coated TiO_2 (Eu_2O_3/TiO_2) nanoparticles was done by a two-step process. The synthesis of TiO_2 nanoparticles has been described in section 2.2.1.1. For the coating of Eu_2O_3 on TiO_2 nanoparticles, 0.01M $EuCl_3$ in ethanol was reduced with $NaBH_4$, and, added in ethanolic solution of TiO_2 nanoparticles. Further, it was autoclaved for 14 hour at 150°C. The so obtained precipitates were filtered, washed and dried at 60°C for about 24 hour, and calcined at 500°C.

4.1.2 Structural and phase analyses

For the efficient performance of DSSC, it has been reported that the anatase phase of TiO_2 nanoparticles is more preferred than rutile and brookite phases [73]. The unstability of brookite phase and slow electron transport in case of rutile phase, make them less desirable for DSSC applications [126]. Considering the favourable surface chemistry and potentially higher conduction-band edge energy of anatase phase, it was utilized for the fabrication of DSSC in the present work.

To know the phase of TiO_2 nanoparticles and to validate the presence of Eu_2O_3 on TiO_2 nanoparticles, XRD analyses have been carried out. Figure 4.1 shows the XRD patterns of bare TiO_2 and Eu_2O_3/TiO_2 nanoparticles. XRD pattern of bare TiO_2 nanoparticles (figure 4.1(a)) reveals the formation of anatase phase with body-centered tetragonal structure (JCPDS Card No. 841286). In case of Eu_2O_3/TiO_2 nanoparticles, some additional peaks related to the body-centered structure of Eu_2O_3 (marked as E, figure 4.1(b)) have been observed (JCPDS Card No. 760154) along with anatase phase of TiO_2 (marked as T). These additional peaks corresponding to the cubic phase of Eu_2O_3 validate the presence of Eu_2O_3 on the surface of TiO_2.

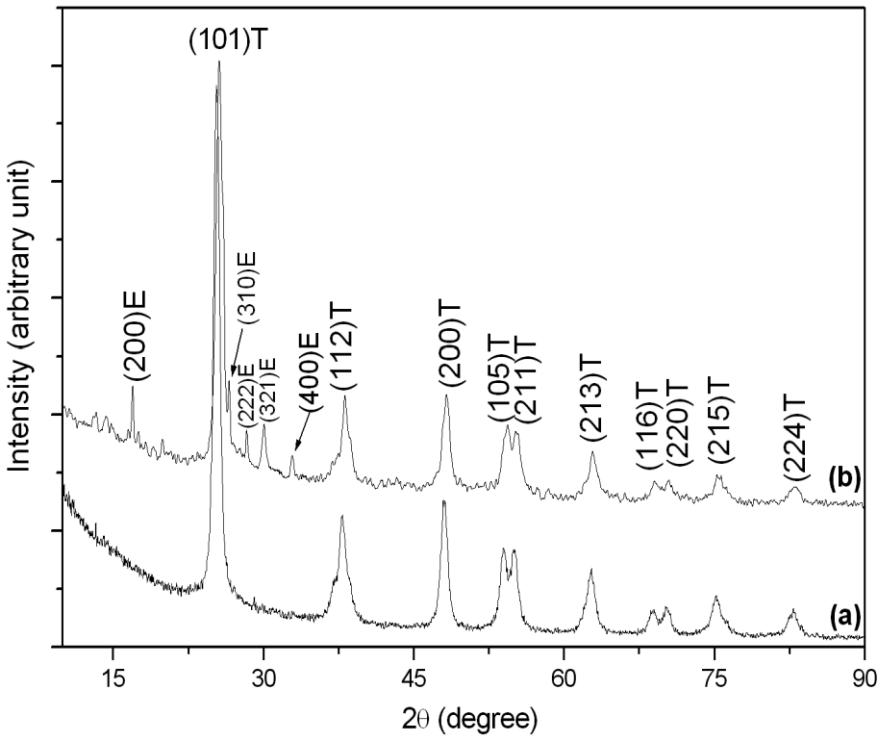

Figure 4.1 X-ray diffractogram of (a) TiO_2 nanoparticles (b) Eu_2O_3/TiO_2 nanoparticles

Table 4.1 shows the crystallite size (D) of the nanoparticles as calculated from the XRD patterns, using Debye-Scherrer formula [127] (eq. 4.1)

$$D = \frac{0.89\lambda}{\beta \cos\theta} \qquad (4.1)$$

where λ is the wavelength (λ = 1.54 Å), β is the full width at half maxima of the (101) peak, and θ is the corresponding diffraction angle.

Table 4.1 Crystallite size calculated from the XRD pattern using Debye-Scherrer formula

Sample	FWHM	2θ	D (nm)	Phase
TiO_2	0.61	25.32	13.14	Anatase
Eu_2O_3/TiO_2	0.65	25.60	12.37	Cubic/Anatase

The crystallite size of the Eu_2O_3/TiO_2 nanoparticles has been found to be smaller than the bare TiO_2 nanoparticles.

4.1.3 Compositional analysis

Further to corroborate the XRD results, EDAX analysis has been carried out. The distribution of the Ti, O and Eu elements on the electrode surface were evaluated by EDAX dot-mapping (figure 4.2). The green, red and blue colours, respectively, show the EDAX dot mapping profile of Ti, O and Eu. It is clear from the EDAX dot mapping spectrum that the surface of TiO_2 contains Eu and O, which supports and confirms the formation of Eu_2O_3 coating on the surface of TiO_2 nanoparticles, as observed in XRD patterns as well (figure 4.1). Moreover, the EDAX spectrum also confirms the homogeneous presence of Eu_2O_3 coating on the TiO_2 surface.

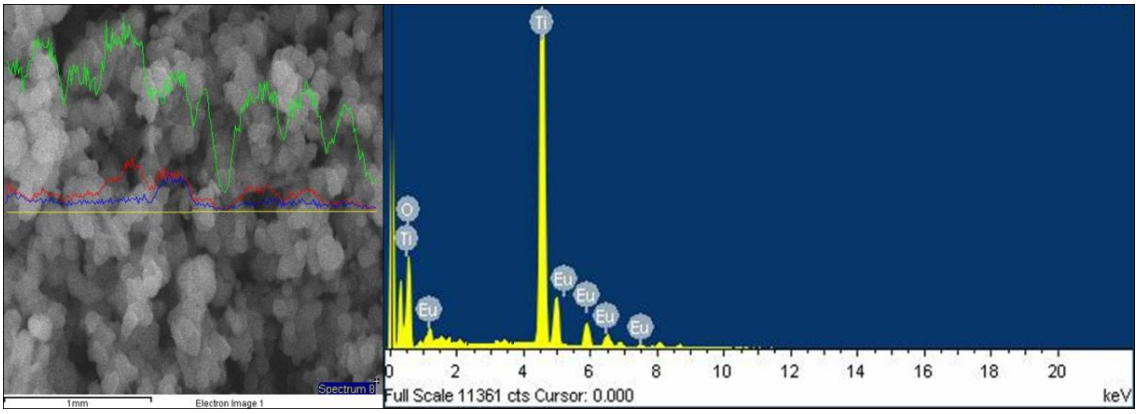

Figure 4.2 EDAX dot maping spectrum of Eu_2O_3/TiO_2 nanoparticles

4.1.4 Morphological study

SEM micrographs of TiO_2 and Eu_2O_3/TiO_2 electrodes (figure 4.3(a) and 4.3(b)), show the formation of spherical nanoparticles, exhibiting porous nature. An increase in surface roughness is noticed in case of Eu_2O_3/TiO_2 (figure 4.3(b)) electrode, which leads to enhacement in the dye loading capability.

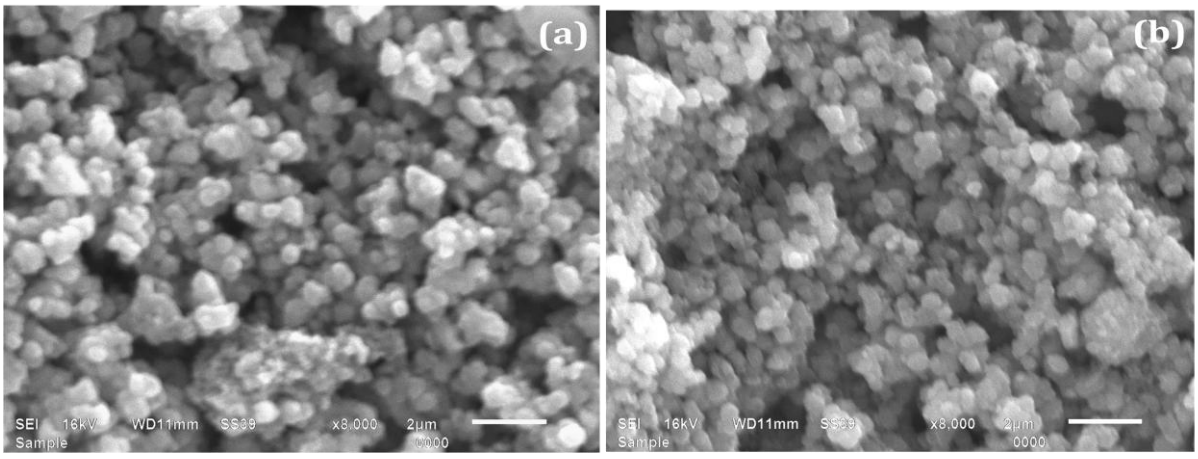

Figure 4.3 SEM micrograph of (a) TiO_2 electrode, (b) Eu_2O_3/TiO_2 electrode

As it was difficult to distinguish Eu_2O_3 coating on the surface of TiO_2 nanoparticles from SEM analysis, hence the TEM study was carried out and micrographs are

shown in figure 4.4(a) and 4.4(b), respectively, for TiO_2 and Eu_2O_3/TiO_2 nanoparticles.

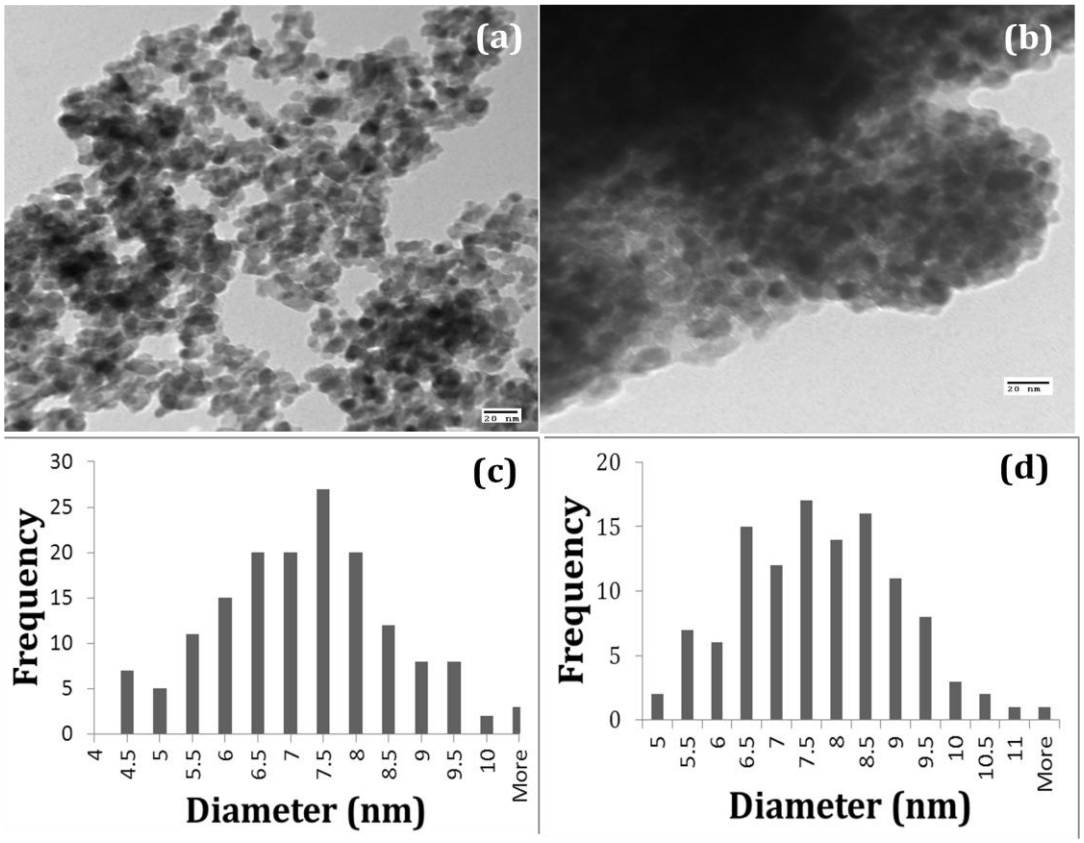

Figure 4.4 TEM micrograph of (a) TiO_2, (b) Eu_2O_3/TiO_2 nanoparticles, Histogram of (c) TiO_2, (d) Eu_2O_3/TiO_2 nanoparticles

The narrow size distribution of the approximately equiaxed particles is well evident from the histogram in figure 4.4(c) and 4.4(d). The mean size of the bare TiO_2 and Eu_2O_3/TiO_2 nanoparticles has been found to be, respectively, 7 nm and 8 nm.

4.1.5 Optical study

4.1.5.1 Photoluminescence study

Figure 4.5 shows the PL spectra of both the synthesized samples. The emission signal at 485 nm is attributed to the charge-transfer from Ti^{3+} to oxygen anion in a TiO_6^{8-}

complex, related with oxygen vacancies at the TiO_2 surface [128]. The emission peak at 384 nm corresponds to a direct band emission of TiO_2, whereas the emission peak at 465 nm associates to the emission process related to the presence of oxygen vacancy defects in TiO_2 [129]. The peak observed around 421 nm is attributed to the self-trapped excitons [130]. On exciting the Eu_2O_3/TiO_2 nanoparticles at 350 nm, the Eu^{3+} ions give emission corresponding to the $^5D_2$-$^7F_3$ and $^5D_0$-$^7F_2$ transitions, respectively, at around 510 nm [131] and 628 nm [132]. A wide band in the 400 to 500 nm region related to anatase TiO_2 has also been observed.

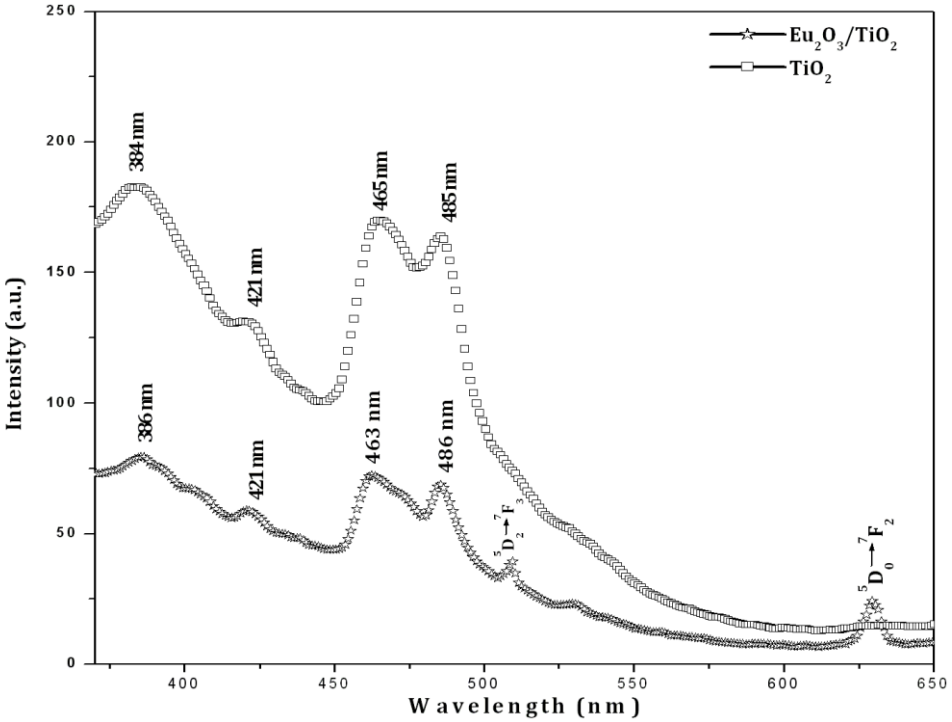

Figure 4.5 Room temperature PL spectra of TiO_2 nanoparticles and Eu_2O_3/TiO_2 nanoparticles

It has been observed from the PL analysis that Eu_2O_3/TiO_2 nanoparticles give emission having lower intensity compared to the bare TiO_2 nanoparticles. Generally, PL emission intensity increases with the increasing number of emitted electrons resulting from recombination between excited electrons and holes, and, consequently,

decreasing the photoactivity [133]. Electron injection efficiency is reduced by hydroxyl groups and physisorbed water molecules present on the surface of TiO_2 nanoparticles. Eu_2O_3 coating on TiO_2 nanoparticles decreases surface OH-groups, resulting in reduction of the unwanted non-radiative decay pathways, thus increasing the electron injection efficiency [134]. The decreased intensity of PL signal at 386 nm inferred that Eu_2O_3 coating on TiO_2 suppresses the electron-hole recombination process on TiO_2 surface. The strong quenching of photoluminescence is due to the increase in the separation efficiency of the photogenerated electron-hole pairs. This enhances the transferring process to the FTO, leading to easier electron transfer activities. Therefore, it can be anticipated that the performance of DSSC, fabricated using Eu_2O_3/TiO_2 nanoparticles, is likely to be better than that of bare TiO_2 DSSC.

4.1.5.2 Dye desorption study

The TiO_2 and Eu_2O_3/TiO_2 photoelectrodes were immersed in 0.5mM ethanolic solution of N719 dye (20mL) for 20 hour. In order to compare the amount of dye adsorbed on the electrode fabricated using TiO_2 and Eu_2O_3/TiO_2 nanoparticles, UV-visible absorption study has been performed on the N719 dye desorbed from TiO_2 electrode and Eu_2O_3/TiO_2 electrode. The dyed film was dipped in 0.1 mM aqueous NaOH solution for 30 minute so that dye gets desorbed from the surface of the film. Figure 4.6 shows the UV-visible absorption spectra of N719 dye desorbed from both the films.

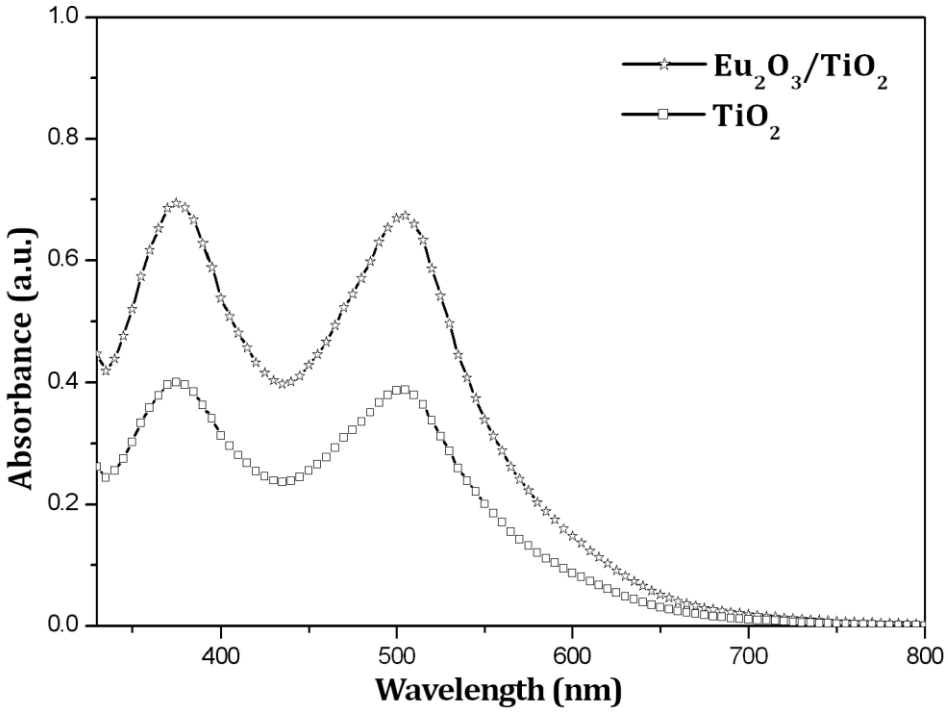

Figure 4.6 UV–Vis absorption spectra of the N719 dye desorbed from TiO_2 electrode and Eu_2O_3/TiO_2 electrode

The better adsorption of the dye molecules on Eu_2O_3/TiO_2 nanoparticles is expected to enhance the DSSC performance, as the extent of dye adsorbed decides the concentration of photogenerated electrons by visible light [135]. The absorbance of the desorbed dye from Eu_2O_3/TiO_2 nanoparticles film has been found to be 72% higher than that of bare TiO_2 nanoparticles, which makes the Eu_2O_3/TiO_2 nanoparticles a potential candidate for DSSC.

4.1.6 Photocurrent density-Voltage (J-V) characteristics

Figure 4.7 shows the typical J-V curves of the DSSCs fabricated using TiO_2 and Eu_2O_3/TiO_2 nanoparticles. J-V characteristics have been obtained by irradiating the assembled solar cells with simulated solar light (100 mW cm^{-2}).

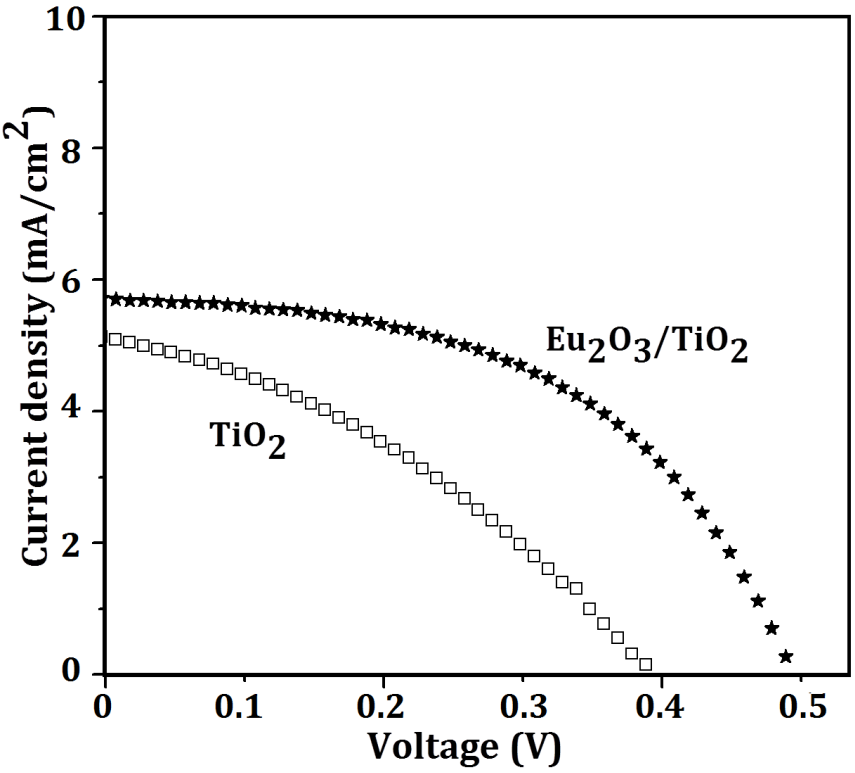

Figure 4.7 J-V curves of TiO_2 and Eu_2O_3/TiO_2 dye sensitized solar cell

Table 4.2 summerizes the different parametrs short-circuit current density (J_{SC}), open circuit voltage (V_{OC}), fill factor (FF) and efficiency (η), as calculated from the J-V curves. An increase in J_{SC}, V_{OC}, FF and η has been observed in DSSC fabricated from Eu_2O_3/TiO_2 nanoparticles compared to TiO_2 nanoparticles.

Table 4.2 Photovoltaic parameters as obtained from the J-V curve of DSSCs

Sample	J_{SC} (mA/cm^2)	V_{OC} (V)	FF	η (%)
TiO_2	5.0	0.39	0.37	0.71
Eu_2O_3/TiO_2	5.7	0.49	0.53	1.48

The increase in J_{SC} can be explained by the fact that the amount of dye molecules adsorbed on Eu_2O_3/TiO_2 electrode is higher than the bare TiO_2 electrode as observed from dye desorbed studies (figure 4.6). The higher extent of absorption of dye molecules in case of Eu_2O_3/TiO_2 leads to higher J_{SC}, which results in greater light harvesting efficiency, and, hence, improves the performance of DSSC [135]. The coating of higher band gap Eu_2O_3 (4.1 eV) on TiO_2 acts as an energy barrier minimizing the electron-hole recombination by increasing the surface resistance of TiO_2 and retarding the back electron transfer to the electrolyte. Therefore, recombination rate decreases between the electrons in the conduction band of TiO_2 and the oxidized dye molecules at the surface of working electrode [45], which enhances the value of V_{OC} from 0.39 V to 0.49 V. Moreover, the coating of Eu_2O_3 layer on TiO_2 surface lowers the electron loss between the FTO/electrolyte interface, which results in increasing the fill factor from 0.37 to 0.53. The efficiency of the DSSCs has been calculated using (eq. 4.2)

$$\eta = \frac{J_{SC} \times V_{OC} \times FF}{P_{in}} \qquad (4.2)$$

where P_{in} is the power of the input light. The efficiencies have been found to be 0.71% and 1.48% for TiO_2 and Eu_2O_3/TiO_2 nanoparticles based DSSC, respectively. Similar results have been observed using coating of higher band gap material such as SnO_2, $CaCO_3$ on TiO_2 nanoparticles by various researchers [68-70]. The enhancement of the cell parameters (V_{OC}, J_{SC}, FF) lead to an increase in the overall DSSC efficiency.

4.2 $CaCO_3$ coated TiO_2 nanoparticles based dye sensitized solar cell

4.2.1 Synthesis of $CaCO_3$ coated TiO_2 nanoparticles

For $CaCO_3$ coating, firstly, TiO_2 nanoparticles (synthesis described in 2.2.1.1) were ultrasonically dispersed in ethanol. In another beaker, 0.02M Na_2CO_3 and $CaCl_2$ were added in water and stirred for 15 minute. Now, this solution was added drop-wise to the dispersed TiO_2 nanoparticles. In this technique, the primarily synthesized TiO_2 nanoparticles act as nucleation sites for the $CaCO_3$ coating. To allow the coating to uniformly form on the particles, and prevent the coating material from being produced separately from the particles, the coating solution was added drop-wise. Further, the above mixture was transferred to Teflon container and autoclaved for 4 hour at 100°C. The particles were washed and filtered. The particles thus obtained were calcined at 300°C for 1 hour, to obtain crystalline nanoparticles.

4.2.2 Structural and phase analyses

The phase present in the synthesized samples has been determined by the use of XRD (figure 4.8) showing the presence of anatase TiO_2 with tetragonal structure (JCPDS No.84-1286).

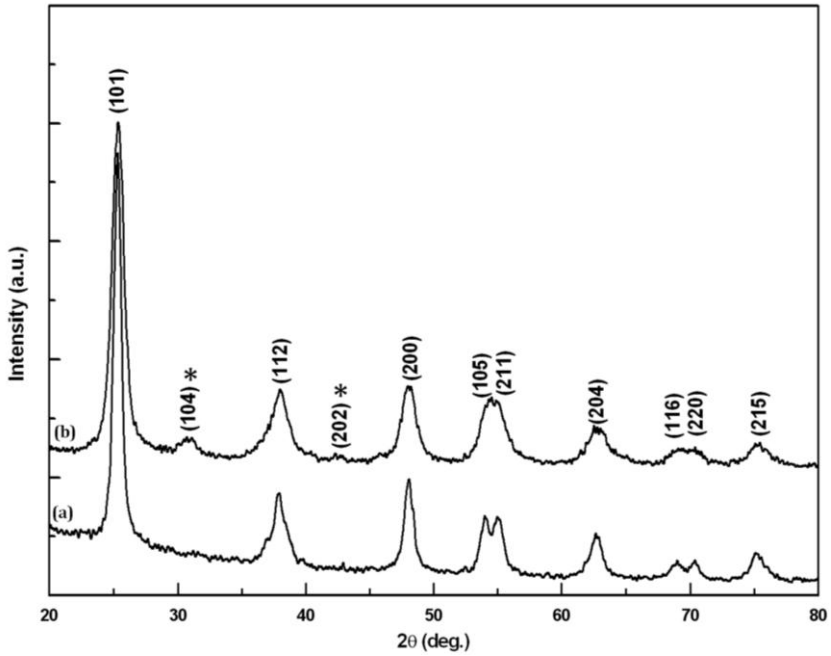

Figure 4.8 X-ray diffractogram of (a) TiO_2 and (b) $CaCO_3/TiO_2$ nanoparticles

The XRD pattern of $CaCO_3/TiO_2$ nanoparticles shows peaks at 29.41° and 42.60° (marked as * in figure 4.8), which correspond to $CaCO_3$ with hexagonal structure and rhomb-centered phase (JCPDS card No: 85-0849). The crystallite sizes of the samples, calculated using Debye–Scherrer formula [127], have been found to be 10.52 nm and 8.23 nm for bare and $CaCO_3/TiO_2$ nanoparticles, respectively; the crystallite size of the later being smaller than the bare TiO_2 nanoparticles. The growth mechanism for the bare TiO_2 nanoparticles involves the spreading of the domain structure throughout the grain up to grain boundaries whereas in case of coated TiO_2 nanoparticles, this spread of domain structure is restricted due to the surface coating. This results in decrease in the crystallite size of coated TiO_2 nanoparticles [120]. The presence of $CaCO_3$ over TiO_2 nanoparticles can be concluded from the XRD analysis.

4.2.3 Compositional analysis

Further to corroborate XRD results, EDAX analysis of TiO_2 and $CaCO_3/TiO_2$ nanoparticles has been shown in figure 4.9. The EDAX spectra of TiO_2 nanoparticles (figure 4.9(a)) reveal the presence of Ti and O elements with atomic percentage 23.86% and 76.14%, respectively. The EDAX spectrum of $CaCO_3/TiO_2$ nanoparticles (figure 4.9(b)), reveals the presence Ca, C, O and Ti elements with atomic percentage 0.30%, 25.86%, 56.76% and 17.08%, respectively. It confirms the $CaCO_3$ coating on the surface of TiO_2 nanoparticles, observed in XRD patterns as well (figure 4.8).

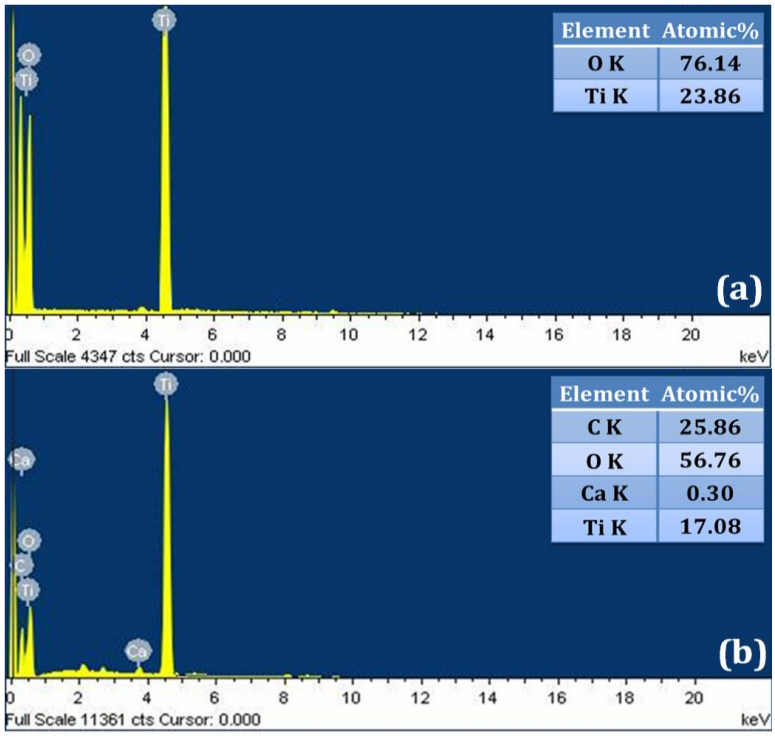

Figure 4.9 EDAX spectra of (a) TiO_2 and (b) $CaCO_3/TiO_2$ nanoparticles

4.2.4 Morphological analysis

TEM micrographs of TiO_2 and $CaCO_3/TiO_2$ nanoparticles are shown in figure 4.10(a, b). The histograms (inset) show the narrow size distribution of the approximately spherical particles. The average particle size of the bare TiO_2 and $CaCO_3/TiO_2$

nanoparticles has been found to be, 6.60 nm and 7.33 nm, respectively. HRTEM (figure 4.10(c)) has been used to confirm the coating of $CaCO_3$ on TiO_2 nanoparticles. The lattice fringes of TiO_2 nanoparticles confirm its crystalline nature. The HRTEM image also confirms the presence of $CaCO_3$ coating over the TiO_2 surface (shown by black line in figure 4.10(c)).

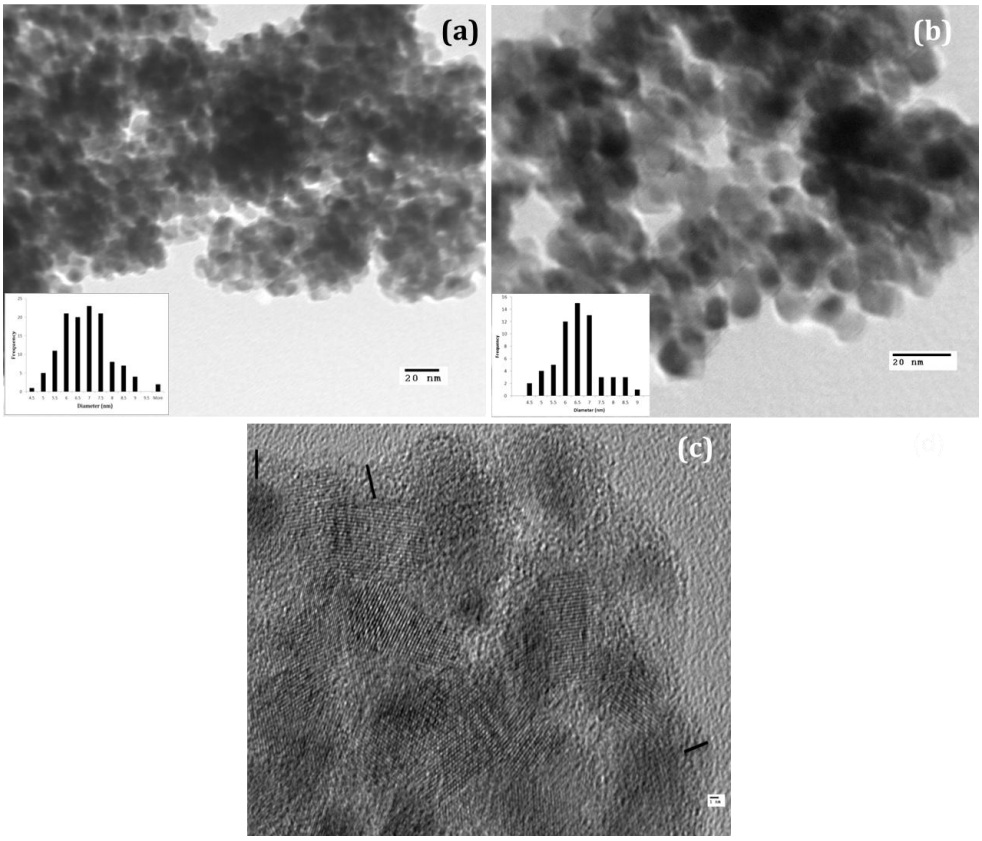

Figure 4.10 (a) TEM image of TiO_2 nanoparticles (b) TEM image (c) HRTEM image of $CaCO_3/TiO_2$ nanoparticles

4.2.5 FTIR spectroscopy

To confirm the chemical interactions of TiO_2 with $CaCO_3$, FTIR study has been done and compared with the FTIR spectra of uncoated TiO_2 nanoparticles, as shown in figure 4.12. The spectra of TiO_2 and $CaCO_3/TiO_2$ show a band observed at around 3421 cm^{-1} characteristic of non-hydrogen bonded hydroxyl groups; this is because the

hydroxyl group and adsorbed water dominate the surface chemistry of TiO_2 [136]. The peak observed in both the spectra at 1632 cm^{-1} is attributed to the bending modes of adsorbed water [137]. The characteristic vibrations of the inorganic Ti-O stretch have been observed in the range 400-900 cm^{-1}. The FTIR spectrum confirms the existence of C-O in CO_3^{2-} in the region of 1600 cm^{-1} to 1300 cm^{-1} due to antisymmetric stretching as well as by the band at 800 cm^{-1} to 600 cm^{-1} due to the out of plane bending [138]. Overlap occurs between the stretching modes of the Ti-O and the out of plane bending modes of the CO_3^{2-} band. Two peaks, 1497 cm^{-1} and 1380 cm^{-1}, corresponding to the asymmetric and symmetric stretching vibrations of O-C-O have been observed in the spectrum of $CaCO_3/TiO_2$ nanoparticles, which is due to the carboxylate group-Ti bridging structure; this confirms the presence of $CaCO_3$ coating over TiO_2 nanoparticles [68].

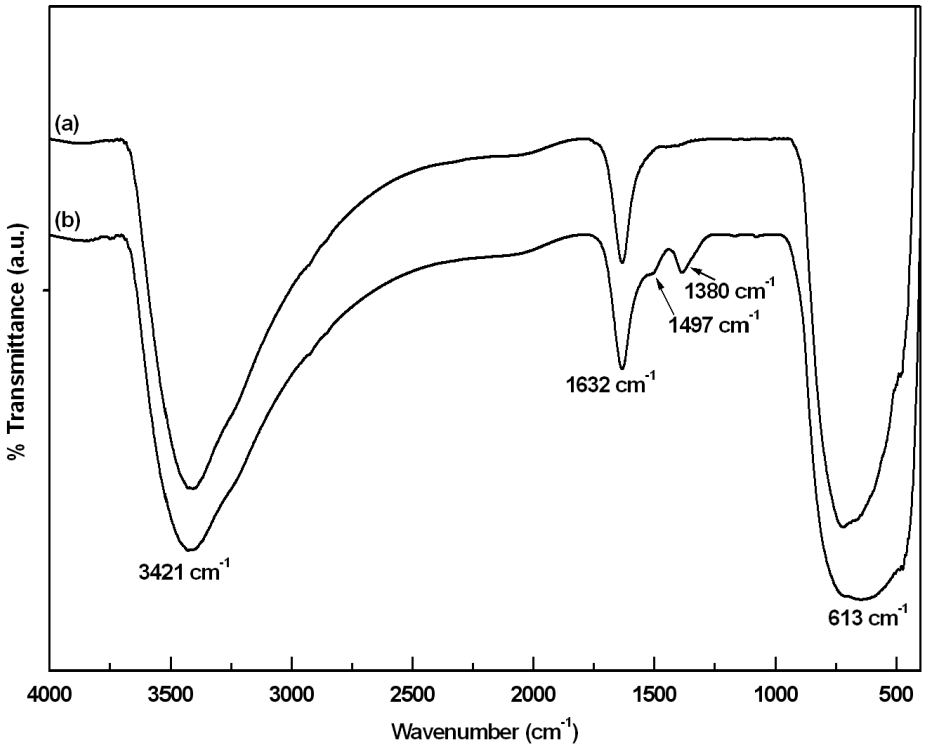

Figure 4.11 FTIR spectra of (a) TiO_2 and (b) $CaCO_3/TiO_2$ nanoparticles

In general, the electron injection efficiency is reduced by hydroxyl groups and physisorbed water molecules present on the surface of TiO_2 nanoparticles. The coating of $CaCO_3$ on TiO_2 nanoparticles leads to reduction in surface O-H groups, which is evident from slight decrease in the intensity of the O-H band at 3421 cm^{-1}. Consequently, the increase in the electron injection efficiency from TiO_2 to FTO is expected, which enhances the overall conversion efficiency (η) of DSSC.

4.2.6 Optical analyses

4.2.6.1 Photoluminescence studies

Due to surface modification of TiO_2 with $CaCO_3$ (figure 4.12), an appreciable change in the PL emission spectra of $CaCO_3/TiO_2$ nanoparticles has been observed. The emission in nanocrystalline TiO_2 is due to the defects resulting from under coordinated Ti^{4+} ions, oxygen vacancies, chemisorbed surface species, which result in the localized intra-band gap states that serve as electron traps. In the emission spectra of TiO_2 nanoparticles, the emission peak, 384 nm, corresponds to a direct band emission of the fundamental band gap of anatase TiO_2, whereas the emission peak, 440 nm, relates to the emission process of oxygen vacancy defects in TiO_2 [129]. The peak, 421 nm, is attributed to the self-trapped excitons [130], and, the emission signal, 485 nm, to the charge-transfer from Ti^{3+} to oxygen anion in a TiO_6^{8-} complex, related with oxygen vacancies at the TiO_2 surface [128]. The green emission, 530 nm, can be associated with anion vacancies on the surface of TiO_2 nanoparticles [139]. In case of $CaCO_3/TiO_2$ nanoparticles, the strong quenching of PL emission is due to the increase in the separation efficiency of the photo-generated electron–hole pairs.

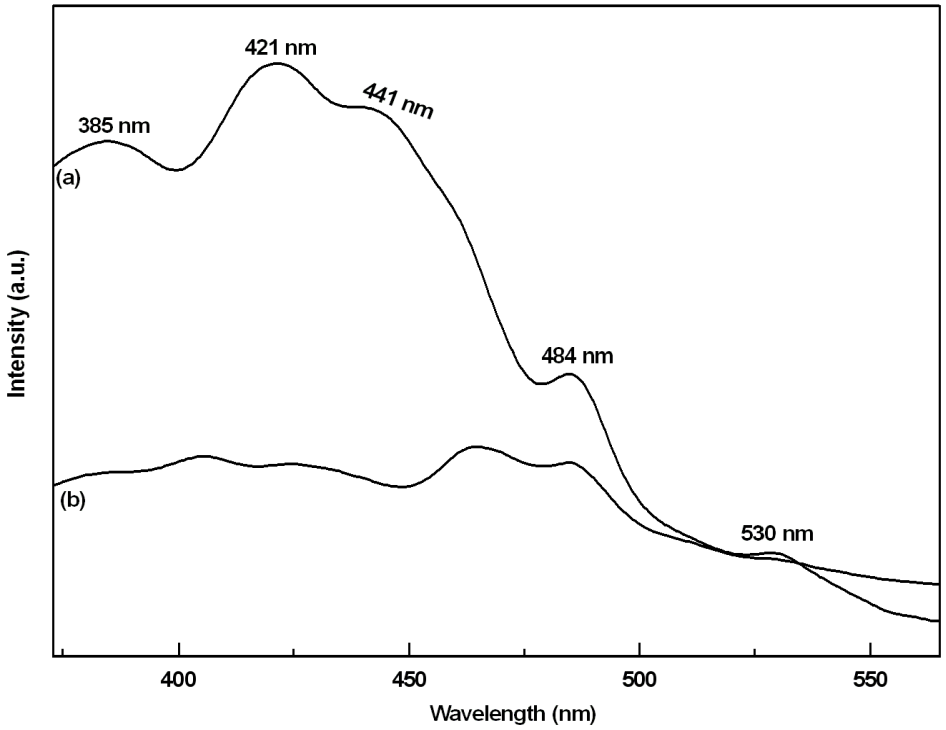

Figure 4.12 PL spectra of (a) TiO_2 and (b) $CaCO_3/TiO_2$ nanoparticles

The PL emission mainly results from the recombination of excited electrons and holes, and thus the lower PL intensity indicates the decrease in recombination rate. Also, the electron injection efficiency is reduced by the hydroxyl groups and physisorbed water molecules present on the surface of TiO_2 nanoparticles (as discussed in section 4.2.5). The surface O-H groups are reduced on coating, thus resulting in reduction of the unwanted non-radiative decay pathways thereby increasing the electron injection efficiency. This ensures better performance of $CaCO_3/TiO_2$ DSSC as compared to the bare one.

4.2.6.2 Dye desorption studies

The TiO_2 and $CaCO_3/TiO_2$ photoelectrodes were immersed in 0.3mM ethanolic solution of N719 dye (20mL) for 12 hour. Figure 4.13 shows the UV-visible absorption spectra of the desorbed dye obtained from both the electrodes. The peaks

found near 370 nm and 500 nm correspond to the characteristic absorption of N719 dye.

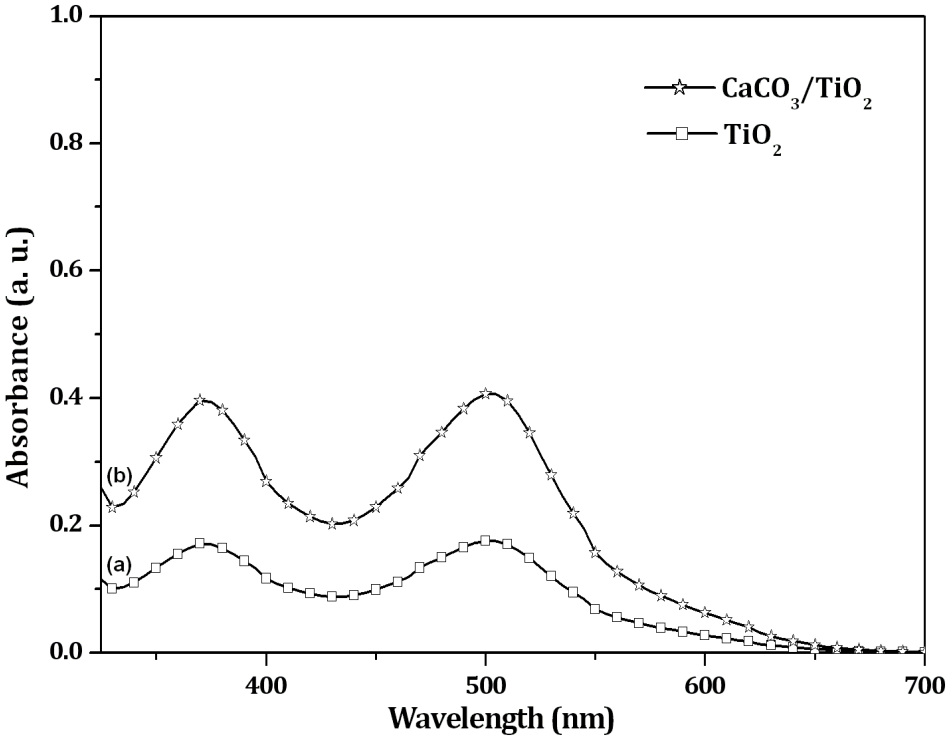

Figure 4.13 UV-visible absorption spectra of the N719 dye desorbed from (a) TiO_2 and (b) $CaCO_3/TiO_2$ electrode

From the desorbed dye spectra analysis, it has been found that the amount of dye adsorbed on the $CaCO_3/TiO_2$ photoelectrode has been found to be higher than that of bare TiO_2 electrode. The higher basicity of the $CaCO_3$ favours the dye adsorption through the carboxylic acid group of the N719 dye [140]. It is less probable for the N719 dye to fully cover the TiO_2 surface without the basic $CaCO_3$ coating due to intermolecular electrostatic repulsion. Further, the increased dye adsorption facilitates the enhancement of short circuit current in $CaCO_3/TiO_2$ based DSSC; since the current density is influenced by the initial number of photo-generated electron-hole pairs [117]. Thus, $CaCO_3/TiO_2$ electrode ensures more efficient photon capturing in the visible region.

4.2.7 Photocurrent density–voltage (J–V) characteristics

DSSC fabricated using synthesized nanoparticles have been characterized by measuring the current density–voltage (J-V) behaviour while irradiating simulated AM 1.5 sunlight, with a power density of 100 mW/cm^2. Figure 4.14 shows the typical J–V curves of the DSSC fabricated using TiO_2 and $CaCO_3/TiO_2$ nanoparticles. Table 4.3 summarizes the different parameters calculated from the J-V curve viz. open circuit voltage, short circuit current density, fill factor (FF), and overall energy conversion efficiency. From the Table, it is clear that, the efficiency achieved by DSSC, fabricated using $CaCO_3/TiO_2$ nanoparticles, is 1.44%, and, that of TiO_2 nanoparticles based DSSC, 0.46% - an increase in efficiency by over 200%.

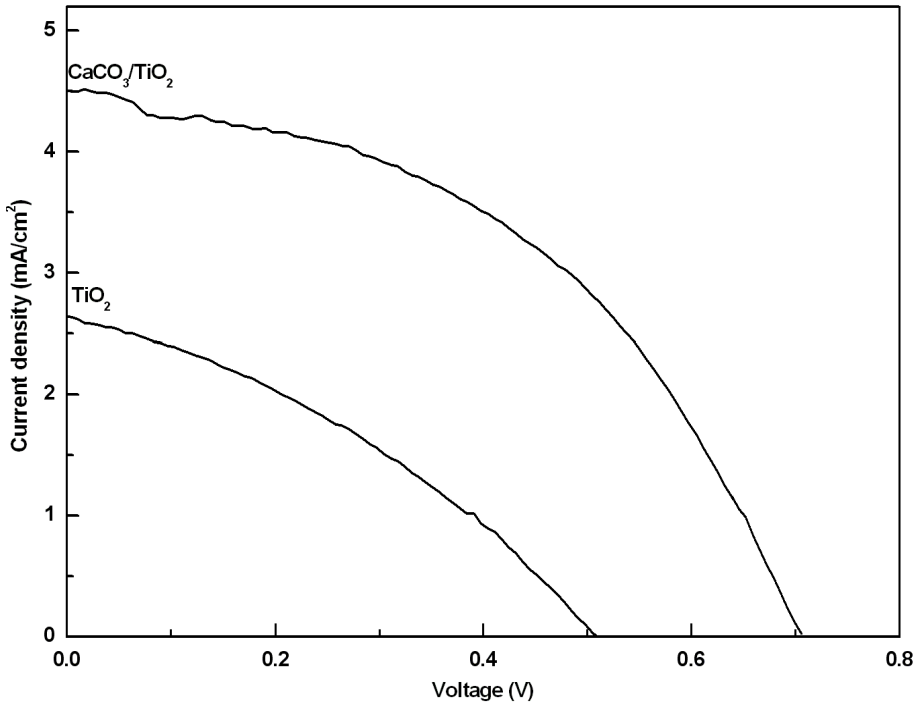

Figure 4.14 J-V curves of the DSSC fabricated using (a) TiO_2 and (b) $CaCO_3/TiO_2$ nanoparticles

Table 4.3 The different parameters J_{SC}, V_{OC}, FF and η, as calculated from the J-V curve

Sample	J_{SC} (mA/cm^2)	V_{OC} (V)	FF	η (%)
TiO_2	2.64	0.50	0.34	0.46
$CaCO_3/TiO_2$	4.49	0.71	0.45	1.44

The current density is influenced by the initial number of photo-generated electron-hole pairs and the electron injection efficiency from dye molecules to semiconductor. The increase in dye adsorption of $CaCO_3/TiO_2$ electrode leads to an increase in the probability of interaction between the photons and the dye molecules, and, thus, resulting in the generation of more electron-hole pairs. Also, by $CaCO_3$ coating, the surface O-H groups are reduced resulting in reduction of the unwanted non-radiative decay pathways; this increases the electron injection efficiency. Thus the current density of $CaCO_3/TiO_2$ based DSSC is 70% higher than that of the TiO_2 based DSSC. The $CaCO_3$ being more basic than TiO_2 introduces the electrostatic field since it attracts more dye molecules, which can deprotonate the TiO_2 nanoparticles [141]. The $CaCO_3$ coating increases open circuit voltage as its high band gap and high isoelectric point (IEP) result in reduction of electron recombination [141]. Consequently, the open circuit voltage increases due to the increased offset between the quasi Fermi level of TiO_2 nanoparticles and the redox level of electrolytes. The fill factor reflects the quality of the electrode and the extent of electrical and electrochemical losses taking place during the operation of the DSSC. The fill factors for TiO_2 and $CaCO_3/TiO_2$ have been found to be 0.34 and 0.45, respectively. Due to the reduction

in recombination between photoexcited carriers in the $CaCO_3/TiO_2$ electrode and triiodide ions in the electrolyte, the cell resistance decreases, which, consequently, increases the fill factor [142]. The increase in short circuit current density, open circuit voltage and fill factor in case of $CaCO_3/TiO_2$ based DSSC has led to an increase in efficiency as compared to TiO_2 based DSSC.

Chapter-5

Conclusions and future scope

Chapter-5

5.1 Conclusions

This chapter concludes the complete work of the thesis. The research work done has been divided into two main parts:

1. Synthesis of Eu_2O_3 and $CaCO_3$ coated ZnO and TiO_2 nanoparticles and their structural, morphological and optical characterizations;

2. Fabrication of dye sensitized solar cells using the synthesized nanoparticles and their current density-voltage (J-V) measurements.

Four different combinations (Eu_2O_3/ZnO, $CaCO_3$/ZnO, Eu_2O_3/TiO_2, and $CaCO_3$/TiO_2) have been employed for the photoelectrode material in DSSCs. The summary of the present work is given below:

1. **Eu_2O_3/ZnO based DSSC**

- The synthesis of ZnO, Eu_2O_3 coated ZnO nanoparticles have been carried out by chemical precipitation method and solvothermal treatment.
- The diffraction plane (222) of Eu_2O_3 detected in XRD pattern demonstrated the existence of Eu_2O_3 on the surface of ZnO, which was further verified using EDAX and FTIR.
- The strong quenching in photoluminescence emission, in case of Eu_2O_3/ZnO nanoparticles, has been attributed to the decrease in recombination rate of photo-generated electron–hole pairs.
- From the dye desorption study, it has been concluded that as compared to ZnO electrodes, Eu_2O_3 coated ZnO electrodes adsorbed more dye.
- The photoelectrochemical properties of the Eu_2O_3/ZnO electrodes have been found to improve and the energy conversion efficiency increases from 0.44%

to 1.45% under the illumination of simulated light of 100 mW/cm^2. Eu_2O_3 coating on ZnO forms an energy barrier, which suppresses the charge recombination. The significant improvement of the open-circuit voltage has been ascribed to the barrier layer effect of Eu_2O_3, which depresses the recombination process in DSSC. The improvement in DSSC efficiency has been attributed to the enhanced dye adsorption as well as retardation of the back electron transfer.

2. **$CaCO_3$/ZnO based DSSC**

- For $CaCO_3$ coating the synthesized ZnO nanoparticles were treated hydrothermally.

- XRD patterns of synthesized nanoparticles reveal that the ZnO and $CaCO_3$-coated ZnO nanoparticles have, respectively, wurtzite and rhomb-centred structure and both having hexagonal phase.

- TEM study reveals that ZnO and $CaCO_3$-coated ZnO nanoparticles possess spherical symmetry and have average particle size, respectively, 6.2 nm and 6.7 nm.

- UV-Vis absorption spectra shows that the electrodes fabricated from the $CaCO_3$-coated ZnO nanoparticles have higher absorbance that shows their higher dye adsorbing power.

- DSSCs fabricated using ZnO and $CaCO_3$-coated ZnO nanoparticles, have been found to have efficiency respectively, 0.44% and 1.00%. An increase of over 100% in efficiency has been registered for $CaCO_3$/ZnO based DSSC as compared to ZnO based DSSC. Coating of $CaCO_3$ on ZnO

enhances the dye adsorption and consequently its efficiency. This study reveals that the coating of wide band gap materials such as $CaCO_3$ on ZnO nanoparticles enhances the efficiency of DSSCs.

3. **Eu_2O_3/TiO_2 based DSSC**

- TiO_2 and Eu_2O_3/TiO_2 nanoparticles have been successfully synthesized via sol-gel and their arrested solvothermal process.

- XRD of Eu_2O_3/TiO_2 shows the presence of cubic Eu_2O_3 and anatase phase of TiO_2, both having body-centred tetragonal structure.

- SEM images reveal an increase in surface roughness in case of Eu_2O_3/TiO_2 electrode, which lead to enhancement in its dye loading capacity as compared to bare TiO_2 electrode.

- The decreased intensity of PL intensity of Eu_2O_3/TiO_2 sample infers that Eu_2O_3 coating suppresses the electron–hole recombination process on TiO_2 surface.

- DSSC fabricated using Eu_2O_3 coated TiO_2 nanoparticles as electrode, exhibit a higher conversion efficiency, 1.48%, - 52 % higher as compared to that of the bare TiO_2 nanoparticles, 0.71%.

- Coating of high band gap Eu_2O_3 on TiO_2 nanoparticles increases the dye adsorption, which leads to greater light harvesting efficiency, and, hence, J_{SC} increases. Also the coating acts as an energy barrier, which minimizes the electron–hole recombination at the TiO_2/dye/electrolyte interface by

increasing the surface resistance of Eu_2O_3 coated TiO_2 and retarding the back electron transfer to the electrolyte; this, in turn, increases V_{OC}.

4. **$CaCO_3/TiO_2$ based DSSC**

- $CaCO_3$ coating on TiO_2 nanoparticles has been successfully done by hydrothermal method.

- In the XRD pattern of $CaCO_3/TiO_2$ nanoparticles, $CaCO_3$ has been detected, demonstrating its coating on the surface of TiO_2, which has been further verified using HRTEM, EDAX and FTIR.

- The strong quenching in photoluminescence emission, in the case of $CaCO_3/TiO_2$ nanoparticles, has been attributed to the decrease in recombination rate of photo-generated electron-hole pairs.

- The dye desorption studies reveal that $CaCO_3/TiO_2$ electrodes adsorbed more dye than the bare TiO_2 electrode.

- $CaCO_3/TiO_2$ based DSSC shows improved photo-electrochemical properties as compared to the bare TiO_2 based DSSC. This is due to the fact that $CaCO_3$ coating on TiO_2 forms an energy barrier, which consequently suppresses the charge recombination, and, thus, improves the overall energy conversion efficiency (η) from 0.46% to 1.44% under the illumination of simulated light of 100mW/cm^2. The increase in J_{SC} is attributed to higher dye adsorption of $CaCO_3/TiO_2$ electrode as compared to that of the bare TiO_2 electrode.

5.2 Future scope

A large number of investigations over the past 20 years have led to significant advances in the development of DSSCs. In future, work can be carried out to synthesize nanowires-hollow nanoparticles composites. These nanocomposites can be employed as photo-anode material for DSSC. The approach of using nanowires (1-D system) is motivated by the fact that the electron transport and collection are improved in nanowires compared to the traditional nanostructures based on interconnected nanoparticles. In addition, the 1-D systems significantly scatter light, and hence enhance light harvesting efficiency. Moreover, hollow nanostructures show both light scattering and light trapping, which makes them promising for DSSC applications. Additionally, hollow nanoparticles with varying size can be employed as a photo-electrode material in DSSC.

References

1. http://www.wallstformainst.com/2012/07/17/indias-energy-crisis/
2. J. Chow, R. J. Kopp, P. R. Portney, Science 302 (5650), 2003, 1528
3. P. V. Kamat, J. Phys. Chem. C 111, 2007, 2834
4. http://www3.nd.edu/~kamatlab/research_solarCells.html
5. http://www.makeitsolar.com/solar-energy-information/07-solar-cells.htm
6. A. E. Becquerel, Comptes Rendus de L' Academie des Sciences 9, 1839, 145
7. J. Perlin, "From Space to Earth -The Story of Solar Electricity" published by arrangement with aatec publications, 2002
8. T. Penick, B. Louk "Photovoltaic power generation." *TEI Controls. December* (1998)
9. M. Niaz, S. Klassen, B. McMillan, D. Metz., Science Education 94(5), 2010, 903
10. R. L. Nersesian, Energy for the 21st Century: A Comprehensive Guide to Conventional and Alternative Sources (2nd edition)
11. http://www.iitk.ac.in/infocell/iitk/newhtml/storyoftheweek54.htm
12. A. Bosio, A. Romeo, D. Menossi, S. Mazzamuto, N. Romeo, Crystal Research and Technology 46(8), 2011, 857
13. http://www.engineersgarage.com/articles/solar-energy-panels-cells?page=4
14. S. R. Dhage, *IRSAPS Bulletin* (2011): 17
15. K. E. Jasim, Dye sensitised solar cells-working principles, challenges and opportunities, *A chapter in Solar Cells/Book* 2
16. B. O'regan, M. Gratzel, Nature 353, 1991, 737
17. http://www.azonano.com/article.aspx?ArticleID=3175

18. X. D. Gao, C. L. Wang, X. Y. Gan, X. M. Li, Ordered Semiconductor Photoanode Films for Dye-Sensitized Solar Cells Based on Zinc Oxide-Titanium Oxide Hybrid Nanostructures, InTech (2011)
19. K. Hara, H. Arakawa, *Handbook of Photovoltaic Science and Engineering* (2003)
20. M. Grätzel,, Accounts of chemical research 42(11), 2009, 1788
21. S. Kumar, N. Sharma, N. K. Verma, S. K. Chakarvarti, Optoelectronics and advanced materials – rapid communications 1(12), 2007, 677
22. Y. Fang, D. Agrawal, G. Skandan, M. Jain, Materials Letters 58, 2004, 551
23. M. Grätzel, Journal of Photochemistry and Photobiology C: Photochemistry Reviews 4, 2003, 145
24. E. R. Leite, ed. Nanostructured materials for electrochemical energy production and storage, Springer, 2009
25. A. Hagfeldt, G. Boschloo, L. Sun, L. Kloo, H. Pettersson, Chem. Rev. 110, 2010, 6595
26. Z. Yu, N. Vlachopoulos, M. Gorlov, L. Kloo, Dalton Trans. 40, 2011, 10289
27. Y. Gao, L. Chu, M. Wu, L. Wang, W. Guo, T. Ma, Journal of Photochemistry and Photobiology A: Chemistry 245, 2012, 66
28. A. McEvoy, T. Markvart, L. Castañer, T. Markvart, L. Castaner, eds. Practical Handbook of Photovoltaics: Fundamentals and Applications: Fundamentals and Applications. Elsevier, 2003
29. H. Wang, M. Liu, M. Zhang, P. Wang, H. Miura, Y. Cheng, J. Bell, Physical Chemistry Chemical Physics 13(38), 2011, 17359

30. D. N. Srivastava, S. Chappel, O. Palchik, A. Zaban, A. Gedanken, Langmuir 18, 2002, 4160
31. S. Ferrere, A. Zaban, B. A. Gregg, J. Phys. Chem. B 101, 1997, 4490
32. H. Rensmo, K. Keis, H. Lindstrom, S. Sodergren, A. Solbrand, A. Hagfeldt, S.E. Lindquist, L. N. Wang, M. Muhammed, J. Phys. Chem. B 101, 1997, 2598
33. K. Keis, C. Bauer, G. Boschloo, A. Hagfeldt, K. Westermark, H. Rensmo, H. Siegbahn, JPPA: Chemistry 148, 2002, 57
34. K. Sayama, H. Sugihara, H. Arakawa, Chem. Mater. 10, 1998, 3825
35. F. Lenzmann, J. Krueger, S. Burnside, K. Brooks, M. Gratzel, D. Gal, S. Ruhle and D. Cahen, J. Phys. Chem. B 105, 2001, 6347
36. S. Ferrere, B. A. Gregg, J. Phys. Chem. B 105, 2001, 7602
37. T.P. Chou, Q. Zhang, G. Cao, J. Phys. Chem. C 111, 2007, 18804
38. D. Jyoti, D. Mohan, R. Dhar, J. Renewable Sustainable Energy 5, 2013, 013112
39. D. Jyoti, D. Mohan, R. Dhar, Mod. Phys. Lett. B 26, 2012, 1250123
40. Y. Gao, M. Nagai, Langmuir 22, 2006, 3936
41. C. H. Ku, J. J. Wu, Nanotechnology 18, 2007, 505706
42. C. Y. Jiang, X. W. Sun, G. Q. Lo, D. L. Kwong, J. X. Wang, Appl. Phys. Lett. 90, 2007, 263501
43. I. C. Baek, M. Vithal, J. A. Chang, J. H. Yum, M. K. Nazeeruddin, M. Grätzel, Y. C Chung, S. I. Seok, Electrochemistry Communications 11, 2009, 909
44. H. Wang, Y. Liu, M. Li, H. Huang, M. Zhong, H. Shen, Appl Phys A 97, 2009, 25

45. D. B Menzies ,Q. Dai, L. Bourgeois, R. A. Caruso ,Y-B. Cheng, G. P. Simon, L Spiccia, Nanotechnology 18, 2007, 125608
46. M. Hamadanian, V. Jabbari, Applied Solar Energy 47(4), 2011, 281
47. J. K. Kim, K. Shin, K. S. Lee, J. H. Park, Journal of Electrochemical Science and Technology 1(2), 2010, 81
48. P. Wang, L. Wang, B. Ma, B. Li, Y. Qiu, J. Phys. Chem. B 110, 2006, 14406
49. L. C. K Liau, C. C. Lin, Applied Surface Science 253, 2007, 8798
50. Adriana Zaleska, Recent Patents on Engineering 2, 2008, 157
51. E. Palomares, J. N. Clifford, S. A. Haque, T. Lutz, J. R. Durrant, Chem. Commun. 14, 2002, 1464
52. D. B. Menzies, Q. Dai, Y. B. Cheng, G. Simon, L. Spiccia, Mater. Lett. 59, 2005, 1893
53. E. Palomares, J. N. Clifford, T Lutz, J. R. Durrant, J. Am. Chem. Soc. 125, 2003, 475
54. A. Kay, M. Gratzel, Chem. Mater. 14, 2002, 2930
55. H. S. Jung, J. K. Lee, M. Nastasi, S. W. Lee, J. Y. Kim, J. S. Park, K. S. Hong, H. Shin, Langmuir 21, 2005, 10332
56. N. O. V. Plank, H. J. Snaith, C. Ducati, J. S. Bendall, L. S. Mende, M. E. Welland, Nanotechnology 19, 2008, 465603
57. C. Lee, G. W. Lee, W. Kang, D. K. Lee, M. J. Ko, K. Kim, N. G. Park, Bull. Korean Chem. Soc. 31, 2010, 3093

58. B. C. O'Regan, S. Scully, A. C. Mayer, E. Palomares, J. Durrant, J. Phys. Chem. B 109, 2005, 4616

59. S. Yang, H. Kou, S. Song, H. Wang, W. Fu, Colloids and Surfaces A: Physicochemical and Engineering Aspects 340, 2009, 182

60. H. Yu, B. Xue, P. Liu, J. Qiu, W. Wen, S. Zhang, H. Zhao, ACS Appl. Mater. Interfaces 4(3), 2012, 1289

61. L. Lu, R. Li, T. Peng, K. Fan, K. Dai, Renew. Energy 36 (12), 2011, 3386

62. M. Zalas, M. Klein, Int. J. Photoenergy 2012, 927407

63. R. Chen, Y.Q. Shen, F. Xiao, B. Liu, G.G. Gurzadyan, Z.L. Dong, X.W. Sun, H.D. Sun, J. Phys. Chem. C 114, 2010, 18081

64. L. Yang, Y. She, S. Zhao, S. Yue, Q. Wang, A. Hu, W. Zhang, J. Appl. Phys. 108, 2010, 104301

65. W.L. Huang, J. Labis, S.C. Ray, Y.R. Liang, C.W. Pao, H. M. Tsai, C.H. Du, W.F. Pong, J.W. Chiou, M.H. Tsai, H.J. Lin, J.F. Lee, Y.T. Chou, J.L. Shen, C.W. Chen, G.C. Chi, Appl. Phys. Lett. 96, 2010, 062112

66. S. Sato, K. Mitsuhashi, T. Ohara, Separation science and technology 39(12), 2004, 2827

67. G. Concas, J. K. Dewhurst, A. Sanna, S. Sharma, and S. Massidda, Physical review B 84, 2011, 014427

68. Z. S. Wang, M. Yanagida, K. Sayama, and H. Sugihara: Chem. Mater. 18, 2006, 2912

69. S. Lee, J. Y. Kim, S. H. Youn, M. Park, K. S. Hong, H. S. Jung, J.K. Lee, H. Shin, Langmuir 23, 2007, 11907

70. S. Lee, J. Y. Kim, K. S. Hong, H. S. Jung, J.K. Lee, H. Shin, Solar Energy Materials & Solar Cells 90, 2006, 2405

71. F. Guo, G. Li, W. Zhang, International Journal of Photoenergy, 2010, 105878

72. D. P. Macwan, Pragnesh N. Dave, S. Chaturvedi, J. Mater. Sci. 46, 2011, 3669

73. N. T. Nolan, M. K. Seery, S. C. Pillai, J. Phys. Chem. C 113, 2009, 16151

74. H. M. Zhang, X. L Liu, Y.B. Li, Y. Li, H. J. Zhao, Sci. China Chem. 56(4), 2013

75. http://pavemaintenance.wikispaces.com/TiO2+Photocatalys+-+Shannon

76. X. Chen, S. S. Mao, Chem. Rev. 107, 2007, 2891

77. R.M. Mohamed, D.L. McKinney, W.M. Sigmund, Materials Science and Engineering R 73, 2012, 1

78. D. M. King, Y. Zhou, L. F. Hakim, X. Liang, P. Li, A. W. Weimer, Industrial & Engineering Chemistry Research 48, 2009, 352

79. X. M. Wang, P. Xiao, Journal of Materials Research 21, 2006, 1190

80. M. R. Oltani, K. Saberyan, F. Shahri, A. Simchi, Powder Technology 209, 15, 2011

81. S. H. Kang, J. W. Lim, H. S. Kim, J-Y Kim, Y-H Chung, Y-E Sung, Chem. Mater. 21, 2009, 2777

82. U. G. Akpan, B. H. Hameed, Journal of Hazardous Materials 170, 2009, 520

83. S. Kumar, N. K. Verma, M. L. Singla, Digest Journal of Nanomaterials and Biostructures 7, 2012, 607

84. H. Morkoç, O. Ümit "General properties of ZnO." *Zinc Oxide: Fundamentals, Materials and Device Technology*, 2009, 1-76.

85. Q. Zhang, C. S. Dandeneau, X. Zhou, G. Cao, Adv. Mater. 2009, 21, 4087

86. M.L. Singla, M. Shafeeq M, M. Kumar, Journal of Luminescence 129(5), 2009, 434

87. V. Kumar, S. Kumar, S. K. Chakarvarti, Journal of Materials Science: Materials in Electronics 21(12), 2010, 1277

88. S. S. Kumar, P. Venkateswarlu, V. R. Rao, G. N. Rao, International Nano Letters 3(1) 2013, 1

89. K. Lu, N. J. Manjooran, R. I. Murakam, G. Pickrell, eds. Advances in Synthesis, Processing, and Applications of Nanostructures: Ceramic Transactions. Vol. 241. John Wiley & Sons, 2012

90. M. A. Aegerter, M. Mennig, eds. Sol-gel technologies for glass producers and users, Springer, 2004

91. E. Khaleghi, E. Olevsky, M. Meyers, J. Am. Ceram. Soc. 92 (7), 2009, 1487

92. http://www.solaronix.com/documents/dye_solar_cells_for_real.pdf

93. http://hyperphysics.phy-astr.gsu.edu/hbase/quantum/bragg.html

94. http://serc.carleton.edu/research_education/geochemsheets/techniques/XRD.html

95. http://xray.tamu.edu/pdf/notes/intro2xrd.pdf

96. http://www.chem.qmul.ac.uk/surfaces/scc/scat7_2.htm

97. http://www4.nau.edu/microanalysis/Microprobe-SEM/Signals.html

98. B. Voutou, E. C. Stefanaki, Electron Microscopy: The Basics, Physics of Advanced Materials Winter School 2008

99. http://www.purdue.edu/rem/rs/sem.htm

100. http://bioweb.usu.edu/emlab/TEM-SEM%20Teaching/How%20TEM%20works.html

101. G. Piburn, A. Barron, An Introduction to Energy Dispersive X-ray Spectroscopy, Connexions Web site. http://cnx.org/content/m43555/1.1/, May 29, 2012.

102. http://www.aspexcorp.com/solutions/omegamax/edxspectroscopy.aspx

103. http://serc.carleton.edu/research_education/geochemsheets/eds.html

104. http://research.fit.edu/hrm/equipment-procedures.php

105. T. H. Gfroerer, "Photoluminescence in analysis of surfaces and interfaces." *Encyclopedia of Analytical Chemistry* (2000).

106. http://inventors.about.com/od/pstartinventions/a/Photoluminescen.htm

107. http://chemwiki.ucdavis.edu/Physical_Chemistry/Spectroscopy/Vibrational_Spectroscopy/Infrared_Spectroscopy/How_an_FTIR_Spectrometer_Operates#The_Components_of_FTIR_Spectrometers

108. https://eee.uci.edu/programs/hongchem/RDGspec20.pdf

109. http://assets.newport.com/webDocuments-EN/images/12298.pdf

110. Y. Li, Y.L. Zou, Mater. Sci.-Pol. 28, 2010, 741

111. R. Viswanatha, T.G. Venkatesh, C.C. Vidyasagar, Y. Arthoba Nayaka, Arch. Appl. Sci. Res. 4, 2012, 480

112. S. Dhara, P.K. Giri, Appl. Nanosci. 1, 2011, 165

113. S. Zandi, P. Kamelin, H. Salamati, H. Ahmadvand, M. Hakimi, Physica B 406, 2011, 3215

114. G. B. Zhang, C. S. Shi, Z. F. Han, J. Y. Shi, Z. X. Fu, M. Kirm, G. Zimmerer, Chin. Phys. Lett. 18, 2001, 441

115. S. Modak, S. Acharya, A. Bandyopadhyay, S. Karan, S.K. Roy, P.K. Chakrabarti, J. Magn. Magn. Mater. 322, 2010, 283

116. R. Chen, Y.Q. Shen, F. Xiao, B. Liu, G.G. Gurzadyan, Z.L. Dong, X.W. Sun, H.D. Sun, J. Phys. Chem. C 114, 2010, 18081

117. A.R. Rao, V. Dutta, Nanotechnology 19, 2008, 445712

118. C.G. Kuo, C.F. Yang, L.R. Hwang, J.S. Huang, Int. J. Photoenergy, 2013, 650973

119. A. Ramar, T. Soundappan, S.M. Chen, M. Rajkumar, S. Ramia Int. J. Electrochem. Sci. 7, 2012, 11734

120. B. R. Rehani, P.B. Joshi, K. N. Lad, A. Pratap, Indian Journal of Pure & Applied Physics 44, 2006, 157

121. Y. Liu, L. Luo, G. Chen, M. Xie, Z. Yu, Iranian Polymer Journal 19 (3), 2010, 207

122. J. S. Ghomi, M. A. Ghasemzadeh, S. Zahedi J. Mex. Chem. Soc. 57(1), 2013, 1

123. C-N Liu, B. Ozkaya, S. Steves, P. Awakowicz and G. Grundmeier J. Phys. D: Appl. Phys. 46, 2013, 084015

124. S. K. Mishra, R. K. Srivastava, S. G. Prakash, R. S. Yadav, and A. C. Panday Opto−Electronics Review 18(4), 2010, 467

125. A.K. Srivastava, Praveen, M. Arora, S.K. Gupta, B.R. Chakraborty, S. Chandra, S. Toyoda, H. Bahadur, J. Mater. Sci. Technol. 26(11), 2010, 986

126. L. Grinis, S. Dor, A. Ofir, A. Zaban, J. Photochem. Photobiol. A Chem. 198, 2008, 52

127. P. Debye, Annalen der Physik. 351, 1915, 809

128. J. Liu, J. Li, A. Sedhain, J. Lin, H. Jiang, J. Phys. Chem. C 112, 2008, 17127

129. S. Chaveanghong, S.M. Smith, J. Sudchanham, T. Amornsakchai, J. Microsc. Soc. Thail. 4, 2011, 36

130. X. Song, L. Gao, Langmuir 23, 2007, 11850

131. X. Chen, Y. Hu, Y. Wang, J. Nanosci. Nanotechnol. 10, 2010, 1865

132. M. Pal, U. Pal, J.M.G.Y. Jime´nez, F.P. Rodrı´guez, Nanoscale Res. Lett. 7, 2012, 1

133. K.V. Baiju, A. Zachariah, S. Shukla, S. Biju, M.L.P. Reddy, K.G.K. Warrier, Catal. Lett. 130, 2009, 130

134. P. Ghosh, A. Patra, Langmuir 22, 2006, 6321

135. M.H. Kim, Y.U. Kwon, J. Phys. Chem. C 113, 2009, 17176

136. T. Ivanova, A. Harizanova, M. Surtchev, Materials Letters 55, 2002, 327

137. D. Beydoun R. Amal, Materials Science and Engineering B 94, 2002, 71

138. M. T. Pham, H. Reuther, W. Matz, R. Mueller, G. Steiner, S. Oswald, I. Zyganov, Journal of Materials Science: Materials In Medicine 11, 2000, 383

139. J. Jun, C. Jin, H. Kim, J. Kang, C. Lee, Appl Phys A 96, 2009, 813

140. S. Wu, H. Han, Q. Tai, J. Zhang, S. Xu, C. Zhou, Y. Yang, H. Hu, B. Chen, B. Sebo, X. Zhao, Nanotechnology 19, 2008, 215704

141. J. Y. Kim, S. Lee, J. H. Noh, H. S. Jung, K. S. Hong, J. Electroceram. 23, 2009, 422

142. S. S. Kanmani, K. Ramachandran, S. Umapathy, International Journal of Photoenergy 2012, 267824